The Survey of Water and Ammonia in the Galactic Center (SWAG): Molecular Cloud Evolution in the Central Molecular Zone

Nico Krieger[1] , Jürgen Ott[2] , Henrik Beuther[1] , Fabian Walter[1,2] , J. M. Diederik Kruijssen[1,3], David S. Meier[4] , Elisabeth A. C. Mills[5] , Yanett Contreras[6] , Phil Edwards[6], Adam Ginsburg[2,7] , Christian Henkel[8,9] , Jonathan Henshaw[1], James Jackson[10] , Jens Kauffmann[8], Steven Longmore[11] , Sergio Martín[12,13], Mark R. Morris[14] , Thushara Pillai[8], Matthew Rickert[15], Erik Rosolowsky[16] , Hiroko Shinnaga[17] , Andrew Walsh[18], Farhad Yusef-Zadeh[15], and Qizhou Zhang[19]

[1] Max-Planck-Institut für Astronomie, Königstuhl 17, D-69120 Heidelberg, Germany; krieger@mpia.de
[2] National Radio Astronomy Observatory, P.O. Box O, 1003 Lopezville Road, Socorro, NM 87801, USA
[3] Astronomisches Rechen-Institut, Zentrum für Astronomie der Universität Heidelberg, Mönchhofstraße 12-14, D-69120 Heidelberg, Germany
[4] New Mexico Institute of Mining and Technology, 801 Leroy Place, Socorro, NM 87801, USA
[5] San Jose State University, 1 Washington Square, San Jose, CA 95192, USA
[6] Leiden Observatory, Leiden University, P.O. Box 9513, NL-2300 RA Leiden, The Netherlands
[7] European Southern Observatory, Karl-Schwarzschild-Straße 2, D-85748 Garching bei München, Germany
[8] Max-Planck-Institut für Radioastronomie, Auf dem Hügel 69, D-53121 Bonn, Germany
[9] Astronomy Department, King Abdulaziz University, P.O. Box 80203, Jeddah 21589, Saudi Arabia
[10] School of Mathematical and Physical Sciences, University of Newcastle, University Drive, Callaghan NSW 2308, Australia
[11] Astrophysics Research Institute, Liverpool John Moores University, 146 Brownlow Hill, Liverpool L3 5RF, UK
[12] European Southern Observatory, Alonso de Córdova 3107, Vitacura Casilla 763 0355, Santiago, Chile
[13] Joint ALMA Observatory, Alonso de Córdova 3107, Vitacura Casilla 763 0355, Santiago, Chile
[14] Department of Physics and Astronomy, UCLA, 430 Portola Plaza, Los Angeles, CA 90095-1547, USA
[15] Department of Physics and Astronomy and CIERA, Northwestern University, Evanston, IL 60208, USA
[16] Department of Physics, CCIS 4-181, University of Alberta, Edmonton, Alberta, T6G 2E1, Canada
[17] Department of Physics and Astronomy, Kagoshima University, 1-21-35, Korimoto, Kagoshima, 890-0065, Japan
[18] International Centre for Radio Astronomy Research, Curtin University, Bentley, 6102, Australia
[19] Harvard-Smithsonian Center for Astrophysics, 60 Garden Street, Cambridge, MA 02138, USA

Abstract

The Survey of Water and Ammonia in the Galactic Center (SWAG) covers the Central Molecular Zone (CMZ) of the Milky Way at frequencies between 21.2 and 25.4 GHz obtained at the Australia Telescope Compact Array at $\sim$0.9 pc spatial and $\sim$2.0 km s^{-1} spectral resolution. In this paper, we present data on the inner $\sim$250 pc (1°.4) between Sgr C and Sgr B2. We focus on the hyperfine structure of the metastable ammonia inversion lines $(J, K) = (1, 1)$–$(6, 6)$ to derive column density, kinematics, opacity, and kinetic gas temperature. In the CMZ molecular clouds, we find typical line widths of 8–16 km s^{-1} and extended regions of optically thick ($\tau > 1$) emission. Two components in kinetic temperature are detected at 25–50 K and 60–100 K, both being significantly hotter than the dust temperatures throughout the CMZ. We discuss the physical state of the CMZ gas as traced by ammonia in the context of the orbital model by Kruijssen et al. that interprets the observed distribution as a stream of molecular clouds following an open eccentric orbit. This allows us to statistically investigate the time dependencies of gas temperature, column density, and line width. We find heating rates between $\sim$50 and $\sim$100 K Myr^{-1} along the stream orbit. No strong signs of time dependence are found for column density or line width. These quantities are likely dominated by cloud-to-cloud variations. Our results qualitatively match the predictions of the current model of tidal triggering of cloud collapse, orbital kinematics, and the observation of an evolutionary sequence of increasing star formation activity with orbital phase.

Key words: Galaxy: center – evolution – ISM: clouds – ISM: kinematics and dynamics – stars: formation

1. Introduction

The Galactic Center (GC) and the Central Molecular Zone (CMZ) in particular represent an environment with conditions that are not to be found anywhere else on large scales in the Milky Way. The CMZ received its name from the presence of a large reservoir of dense ($\gtrsim 10^4$ cm^{-2}) and molecular gas of a few times $10^7 M_\odot$ (Oka et al. 1998; Morris & Serabyn 1996; Ferrière et al. 2007) and covers the central $\sim$500 pc of the GC region. The large amount of molecular gas is found to be accompanied by a relatively high star formation rate (SFR) of $\sim$0.1 $M_\odot$ yr^{-1} (Longmore et al. 2013a; Barnes et al. 2017). Star formation (SF) laws that build on the assumption of a constant gas-depletion time of 1 Gyr can fit the observed SFR (Bigiel et al. 2010; Leroy et al. 2008, 2015). However, these relations are derived from gas at much lower densities than observed in the CMZ. Density-dependent SF laws, on the other hand, strongly overpredict the SFR (Longmore et al. 2013a) at $\sim$0.4 $M_\odot$ yr^{-1} (Kennicutt 1998; Krumholz & McKee 2005; Krumholz et al. 2012) to $\sim$0.8 $M_\odot$ yr^{-1} Lada et al. (2010, 2012). Thus, the star formation efficiency (SFE) in the CMZ is significantly lower than expected for the observed gas densities. The complex interplay of energetic processes in the GC allows for different potential answers to this problem of low SFE, but none of these processes alone can explain the discrepancy (Kruijssen et al. 2014). A general picture of episodic starbursts in gas rings in galactic centers introduced by Krumholz & Kruijssen (2015) and Krumholz et al. (2017) might solve the SFE problem in the particular case of the CMZ and set the framework for another intriguing feature of the GC: a ring-like structure of dust and molecular gas. This structure
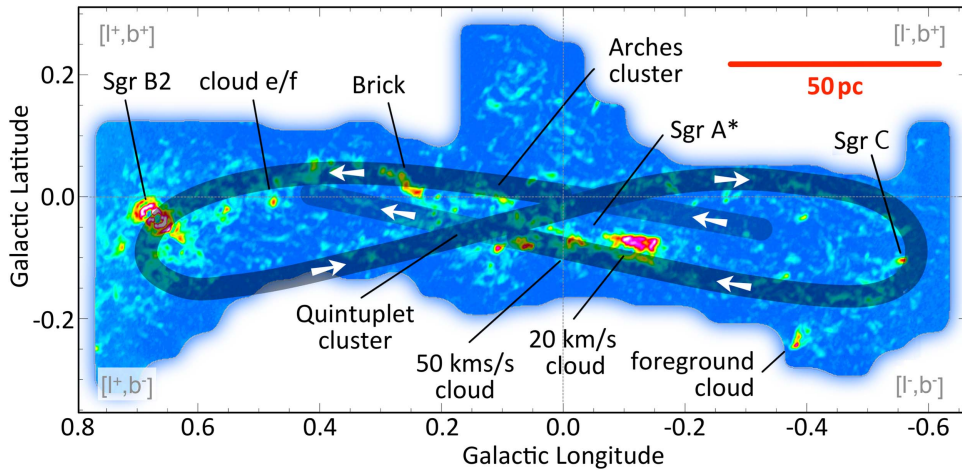
Figure 1. Overview of the GC. The gas (background, SWAG NH_3 (3, 3) peak intensity) resembles the shape of an infinity symbol, ∞, and is parametrized as a sequence of stream segments by K15. The direction of motion is along the dust ridge ($[l^+, b^+]$ denoting positive longitude and latitude) to Sgr B2, $[l^+, b^-]$, $[l^-, b^+]$ to Sgr C and $[l^-, b^-]$. Gas in the dust ridge $[l^+, b^+]$ and $[l^-, b^-]$ is mostly on the near side (in front of the GC), whereas $[l^+, b^-]$ and $[l^-, b^+]$ gas is mostly on the far side (Bally et al. 2010; Molinari et al. 2011). The most important sources are labeled.

(see Figure 1 for an overview) is projected onto an infinity (∞) shape that follows several arcs, the most prominent being the so-called "dust ridge" stretching from the massive molecular cloud G0.253+0.016 ("the Brick") to the star-forming region Sgr B2 (Lis et al. 1999). It might be continued via an $[l^+, b^-]$ arc and another loop at negative longitude ($[l^-, b^+]$, $[l^-, b^-]$) passing through the star-forming region Sgr C. The syntax $[l^{+/-}, b^{+/-}]$ denotes the four quadrants in Galactic coordinates at positive/negative Galactic longitude (l) and latitude (b). Clouds at $[l^-, b^-]$ and $[l^+, b^+]$ are thought to be located in front of Sgr A*, i.e., the near side of the GC that is visible in silhouette against the background, whereas most of the $[l^-, b^+]$ and $[l^+, b^-]$ gas is more likely to be on the far side, i.e., behind Sgr A* (Bally et al. 2010; Molinari et al. 2011).

Various models of the gas and dust distribution in the GC exist: a simple bar model (Morris & Serabyn 1996); variations of a spiral arm model in which the apparent ring is formed by the inner part of two spiral arms (Sofue 1995; Sawada et al. 2004; Rodríguez-Fernández & Combes 2008; Rodríguez-Fernández 2011; Ridley et al. 2017); a closed, twisted elliptical ring detected in dust emission (Molinari et al. 2011), and a sequence of open-ended gas streams (Kruijssen et al. 2015, hereafter K15). K15 highlight the impossibility of closed orbits in extended gravitational potentials and provide a better fit to single-dish ammonia emission in position–position–velocity (PPV) space, as was confirmed by Henshaw et al. (2016b) for three molecular species in single-dish observations. Thus, we focus on this model and call it the "stream model" in contrast to the "ring model" and the "spiral arm" model. According to the stream model, the stream of GC molecular clouds oscillates radially and vertically, and can be traced for $\sim$1.5 revolutions around the GC. The radial oscillation periodically brings dense molecular gas closer ($r \sim 60$ pc at pericenter) to the gravitational center (traced by Sgr A*) and deeper into the potential, whereas the apocenter lies at $r \sim 120$ pc. As the CMZ clouds slowly evolve toward low virial ratios as the turbulent energy dissipates (Krumholz & Kruijssen 2015; Walker et al. 2015; Henshaw et al. 2016a), it is statistically more likely that cloud collapse occurs at the pericenter where the compressive tidal forces are strongest along the orbit and thus a cloud receives the final nudge for the transition to self-gravitation. Subsequent

SF stages will then occur downstream from the pericenter passages and could potentially be observed as an SF sequence if the orbit is sufficiently sampled with molecular clouds that start to collapse at a similar point of their orbits. This model of triggered star formation was first proposed by Longmore et al. (2013b) based on the observation of different evolutionary SF stages along the dust ridge. The two young stellar clusters in the GC, Arches and Quintuplet, may also support this model as their orbits and ages are consistent with formation at a common point after collapse of their respective parent clouds at a pericenter passage (Figure 1 of Stolte et al. 2014; Kruijssen et al. 2015). In addition to stars and star formation tracers, cloud properties are also expected to show evolutionary behavior along the gas streams; this has not been thoroughly tested yet. Weak hints toward rising gas temperatures in the dust ridge are suggested by Ginsburg et al. (2016), while a recent paper by Kauffmann et al. (2017b) based on N_2H^+ data from the Galactic Center Molecular Cloud Survey can neither confirm nor exclude the possibility of triggered evolution when examining mass-size relation and SF suppression. Both analyses were based on a low number of measurements ($\sim$35 measurements in dust ridge clouds in Ginsburg et al. 2016 and six clouds in Kauffmann et al. 2017b) and lack the statistical power to detect potential evolution in the presence of scatter.

In this paper, we aim to test the prediction of the stream model by searching for coherent temporal evolution of molecular gas properties on a broad statistical basis using the Survey of Water and Ammonia in the Galactic Center (SWAG). SWAG targets 42 molecular and atomic species at $\sim$21–25 GHz, of which at least 20 are detected, and thus it offers an ideal database for such an analysis. SWAG maps the CMZ in the region of $\sim -1°$ to $\sim +2°$ in Galactic longitude at latitudes $|b| < 0°4$ using the Australia Telescope Compact Array (ATCA) and achieves a spectral resolution of 0.4 km s^{-1} at $\sim 20''$ spatial resolution. One of the survey's signature targets is the ammonia molecule, the properties of which are well suited to exploring the thermal and kinematic structure of the interstellar medium (ISM; Ho & Townes 1983). In an ammonia (NH_3) molecule, the nitrogen atom can tunnel through the plane of hydrogen atoms (inversion) at a rotational-state-dependent frequency that can be related to temperature. These inversion frequencies are closely spaced

$(\Delta\nu_{(1,1)\ldots(6,6)} \sim 1.4\,\mathrm{GHz})$ while covering a large energy range (excitation energy $22 < T_l[\mathrm{K}] \lesssim 400$) that traces moderately dense gas of 10^4–$10^6\,\mathrm{cm}^{-3}$ due to the critical density being $n_{\mathrm{crit}} \sim 10^3\,\mathrm{cm}^{-3}$ (e.g., Shirley 2015). Detections of ammonia span a large range of sources from circumstellar envelopes (e.g., Betz et al. 1979) to galactic dark clouds (e.g., Ho et al. 1978) and nearby galaxies such as NGC 253 (e.g., Ott et al. 2005; Lebrón et al. 2011; Mangum et al. 2013; Gorski et al. 2017) to heavily star-forming galaxies like ultraluminous infrared galaxies (ULIRGS; e.g., Arp 220, Ott et al. 2011; Zschaechner et al. 2016) and even at high redshift ($z = 0.9$) as absorption against continuum emission (Henkel et al. 2008). In the GC, SWAG offers high-resolution ($\sim$0.9 pc) interferometric ammonia maps that show the intermediate-density gas structure most relevant to the stream model because large-scale diffuse emission $\gtrsim 1\farcm4$ ($\gtrsim 3.3$ pc at 8.3 kpc)[20] is filtered out by the ATCA interferometer in this setup. Spectral fitting of the ammonia hyperfine structure allows us to construct maps of line-of-sight velocity, line width, opacity, and kinetic gas temperature that can be tested for evolutionary behavior under the assumption of a kinematic model. Applying this method to SWAG data and the stream model allows us to check gas properties for absolute time dependencies that can be expected if a sequential star formation sequence is present in one or more of the stream segments.

As the structures in the GC are complex, simple names can be misleading. Throughout this paper, we refer to the "ring" as the general ∞-like structure of CMZ gas without being interested in the detailed structure or kinematics. "Stream," however, refers to the K15 model that introduced a stream as a set of four segments of an orbit wrapping around the GC whose subdivision does not have physical meaning but simplifies descriptions.

In this paper, we summarize the observational setup and data reduction of the SWAG survey in Section 2 on the basis of observations of one-third of the total area, covering the region between Sgr B2 and Sgr C. Section 3 shows and discusses the primary data products (channel and moment maps, spectra, position–velocity diagrams), and Section 4 describes the fitting of the ammonia hyperfine structure inversion lines. In Section 5 we use the derived thermal and kinetic properties of GC molecular clouds to discuss their properties in the context of the orbital model of K15 by reconstructing potential time dependencies of these properties. The resulting relations are discussed in the context of the star formation sequence as proposed by Longmore et al. (2013b). A summary in Section 6 concludes this work. Appendices show further SWAG data products (Appendix A), details on imaging (Appendix B), the ammonia thermometer (Appendix C), and hyperfine structure line fitting (Appendix D), as well as further fit-derived data products (Appendices E and F) and further time evolution plots (Appendix G).

2. Observations and Data Reduction

SWAG is a large survey aiming to map the entire CMZ of the Milky Way from $\sim$−1° to $\sim$+2° in Galactic longitude at latitudes $|b| < 0\fdg4$. The boundaries correspond to an integrated surface brightness level of $0.1\,\mathrm{K\,km\,s^{-1}}$ of $\mathrm{NH_3}$ (3, 3) from

Mopra single-dish observations (beam size $\sim 2\farcm4$ Ott et al. 2014). The achieved spatial resolution is $\sim 22\farcs8$ ($20\farcs6$–$25\farcs0$ in the range of 25.4–21.2 GHz), which at the Galactic Center distance corresponds to $\sim$0.9 pc. The velocity resolution is $\sim 0.4\,\mathrm{km\,s^{-1}}$ (0.37–$0.45\,\mathrm{km\,s^{-1}}$ for 25.4–21.2 GHz). The observations were performed in a mosaic of $\sim$6500 pointings with the ATCA interferometer during $\sim$525 hr spread over three years (2014–2016). At a wavelength of around 1.3 cm, 42 spectral lines were targeted in the range of 21.2–25.4 GHz; among these are six metastable and three non-metastable ammonia inversion lines, water maser and atomic radio recombination lines, and complex organic molecules. At least 20 of the targeted lines are unambiguously detected.

2.1. Observations

The observations for SWAG were carried out with the ATCA[21] interferometer. Achieving the maximum sensitivity to extended emission requires the most compact array configuration, H75, with baselines of 31–89 m between five dishes. A sixth antenna that is not considered in this work provides baselines of $\sim$4.4 km to the inner antennas. The primary beam FWHM of the 22 m dishes at $\nu = 23$ GHz is $\sim 2\farcm4$. Every position in the targeted area is covered by the primary beam of at least three pointings. In the radio K-band regime, the H75 array configuration is not sensitive to emission extending over more than $\sim 1\farcm4$ (3.3 pc) because of interferometric spatial filtering.

Between 40 and 220 pointings are combined into strips of $\sim 4\farcm5$ width, as shown in Figure 2, which are observed between subsequent observations of the phase calibrator. Long strips are split into Galactic northern and southern parts to ensure frequent phase calibrations. In order to maximize the u, v coverage, pointings are not observed one after the other, but in rows of even and odd numbers, as explained in Ott et al. (2014). The rows are aligned parallel to Galactic longitude ("l-scan" in Ott et al. 2014), while the first element of each row determines its parity (odd, even). Rows of odd parity are observed consecutively, followed by the left-out rows of even parity at somewhat later local sidereal times (LST) and therefore other projected baselines, which increases the u, v coverage. The resulting typical u, v coverage of a single pointing is shown in Figure 3.

The Compact Array Broadband Backend (CABB, Wilson et al. 2011) provides two IF bands, each of 2 GHz bandwidth. In the CFB 64M-32k mode adopted for these observations, each 2 GHz band was divided into 32×64 MHz "continuum" channels with 16 "zoombands" of 2048×32 kHz channels selected in each IF band for spectral line observations. The integration time of each pointing was set to $8 \times 30\,\mathrm{s} = 4$ minutes as a trade-off between low noise and total project time, but it varied due to reobservations and flagging. The eight individual integrations were scheduled for best u, v coverage to be observed over the whole available range of LST from about 15:00 to 22:00 hr as much as possible. Owing to pointing overlap, the actual sensitivity is higher by a factor of $\sqrt{3}$ ($\sqrt{2}$ for edge pointings) than can be expected from the integration time of a single pointing. The expected noise calculated from the radiometer equation $\sigma \propto \frac{T_{\mathrm{sys}}}{\sqrt{\Delta\nu\tau}}$ as a function of system temperature T_{sys}, bandwidth $\Delta\nu$, and integration time τ is
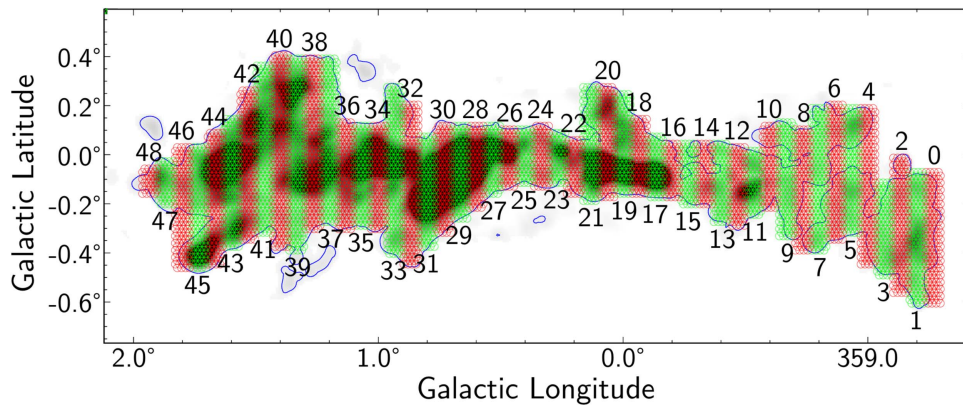

Figure 2. SWAG observing layout. The spatial coverage of SWAG is derived from the 0.1 K km s^{-1} contour (blue) of the Mopra single-dish CMZ survey by Ott et al. (2014; background gray-scale image). Between 40 to 220 pointings are included in an observation strip (numbered from west to east and alternately colored). This work includes data of the inner CMZ covered by strips 10 to 30.
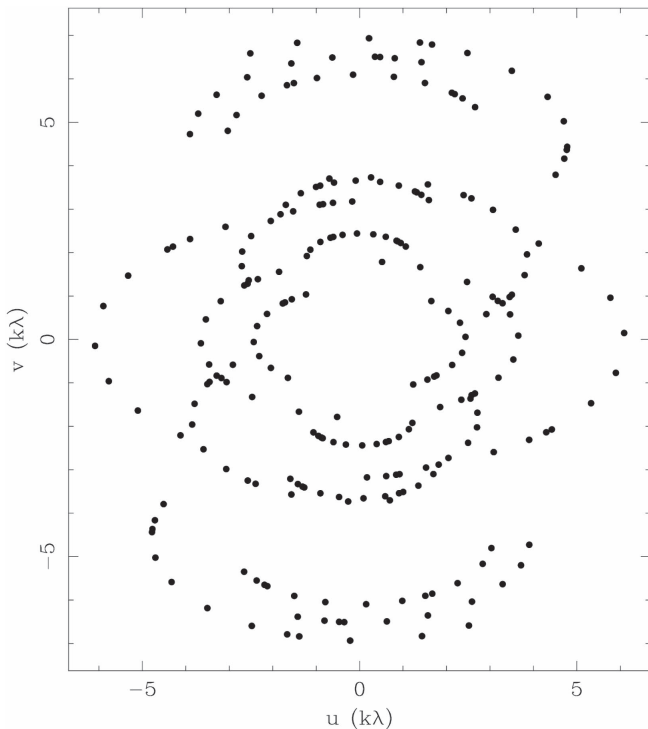

Figure 3. Typical u, v coverage of a single pointing of SWAG using the inner array of five antennas (excluding the far out antenna ca06). Note that overlapping pointings increase the u, v coverage by a factor of $\sqrt{3}$ ($\sqrt{2}$ for edge pointings), which is not included in this plot. The u, v coverage was optimized by the scanning technique ("l-scan") shown in Figure 1 of Ott et al. (2014).

$\sigma = 28$ mK for a typical $T_{sys} = 80$ K in one channel of $\Delta\nu = 32$ kHz (~ 0.4 km s^{-1} at 23 GHz) and $t = 240$ s. This value corresponds to $\sigma \sim 6.0$ mJy beam^{-1} for NH$_3$ (3, 3) ($\nu = 23.87$ GHz, beam $26''03 \times 17''71$), which is about half of the measured noise of ~ 13.1 mJy beam^{-1} (Section 2.3.1) because the deconvolution is imprefect owing to the sparsely sampled u, v plane.

Observations were scheduled in three-week blocks in the southern hemisphere winter months of July/August in each year from 2014 to 2016. The total project time including calibration data sums up to ~ 720 hr (~ 204 hr for the data presented in this paper), including additional time needed to reobserve some regions whose observations were affected by

bad weather, resulting in increased noise. The total on-source time was ~ 525 hr (~ 150 hr shown in this paper).

Bandpasses and delay calibrations for each antenna are derived from daily 10-minute integrations on PKS 1253-055 (3C 279). Its flux of ~ 16–20 Jy at frequencies around 23 GHz is bright enough to derive accurate bandpass solutions. The gain/phase (complex gain) calibrator PKS 1710-269 was observed for 2 minutes every 20–30 minutes, depending on the field, after each l-scan and in between l-scans if necessary. Daily flux calibrations of 5-minute integration time are performed on the radio galaxy PKS 1934638, which is the standard primary flux density calibrator for the ATCA below 50 GHz.

2.2. Calibration

All steps from data import to imaging are performed with the ATCA specific version of the package MIRIAD[22] (Sault et al. 1995). The necessary steps were developed into a data reduction pipeline that provides the base for reducing the entire survey.

2.2.1. Flagging

Raw data are imported via `atlod` with options `birdie`, `nocacal`, `noif,` and `opcorr` to automatically flag resonant instrument modes (birdies), initial array calibration data (cacal), set correct intermediate-frequency mapping behavior, and to apply atmospheric opacity corrections. Some of the array setup data were not detected by the automatic routine and had to be flagged manually with `uvflag`.

Resonant modes in ATCA's backend system cause additional birdies in channels $n \times 1024 + 1 (n = 1, 2, \ldots)$ that are not identified during data import. The missing channels are interpolated later when averaging and Doppler-correcting the visibilities to a common resolution of 2 km s^{-1}. To remove additional correlator artifacts and extreme RFI, calibrator data were clipped at 200 Jy and CMZ observations at 10 Jy. Additional flagging of bad data was made by eye in the interactive task `blflag`. Polarization measurements were not required for the presented analysis, and all crosshands/cross-polarizations (XY and YX for ATCA's linear feeds) were flagged. Antenna ca06 offers high spatial resolution at baselines of >4300 m, but was also flagged due to lack of

---

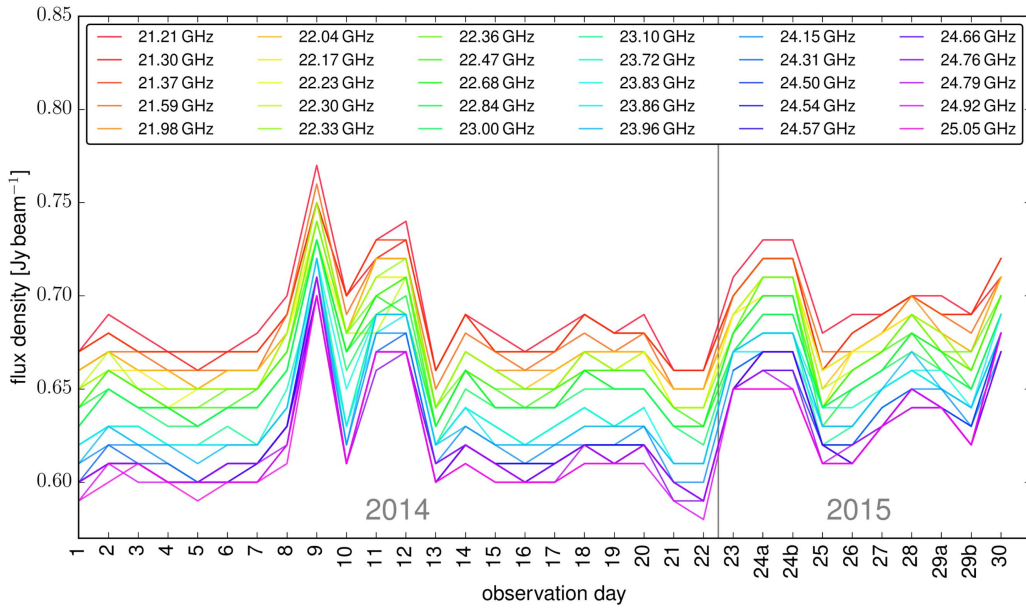[22] http://www.atnf.csiro.au/computing/software/miriad

Figure 4. Flux density of the phase calibrator PKS 1710-269 per observation day after all calibration steps for the 30 frequency bands of CABB. On observation days 24 and 29, correlator crashes required new calibrations, which are labeled a and b and correspond to flux densities before and after the crash, respectively. Flux densities are constant across observation days within ~15%. The increasing values toward lower frequency is an intrinsic property of the source: a quasar with spectral index ~−0.5. The precision of the MIRIAD task imstat is two decimal places, which leads to quantized data.

intermediate u, v points, which drastically down-weights these long baselines. Except for the instrumental birdies we described, little radio frequency interference (RFI) is present at frequencies of ~23 GHz.

2.2.2. Complex Gain Calibration

Bandpass amplitudes and phases are calculated on the designated bandpass calibrator PKS 1253-055. The resulting correction is then applied to the gain/phase calibrator PKS 1710-269 and flux density calibrator PKS 1934-638, and complex antenna gains are derived with mfcal.

Calibration solutions were inspected visually to identify remaining problems that were subsequently flagged. Recalibrations were performed until well-behaved solutions were found.

2.2.3. Flux Density Calibration

The calibration quality is assessed with Figure 4. The phase calibrator PKS 1710-269 was imaged including all calibration corrections for all observation days and all zoombands and the peak flux density listed. Measured flux densities per zoomband are constant within ~15%, which is typical for radio observations at this frequency. The origin of this variability cannot be identified without absolute measurements and can be due to changing atmospheric conditions or intrinsic luminosity variation in the QSO PKS 1710-269. Thus, 15% is an upper limit on the flux density variation across observation days, which is similar to the absolute flux uncertainty.

Spectral lines observed in the same zoomband, however, share a common flux density uncertainty, and thus flux ratios and derived quantities are more accurate. This provides a robust basis for the derivation of the kinetic gas temperature, which is primarily determined from ammonia line ratios.

2.2.4. Continuum Subtraction

Over the relatively small spectral range of a zoomband of ~64 MHz, a linear approximation captures the spectral index of any continuum emission well enough. Line-free channels could not be identified in visibility spectra because the brightness of most of the spectral lines is too low; instead, they are calculated from the line's rest frequency and a window of ±400 channels (corresponding to ~178–150 km s^{-1} at 21.0–25.0 GHz), which is large enough to exclude the typical velocity range of molecular gas in the CMZ of ±150 km s^{-1}. Any possible emission outside these line-free windows is weak and does not affect the continuum fit. Fit and subtraction were made using the uvlin task, forcing a first-order polynomial.

Rest frequencies are set according to Table 1, which lists values from splatalogue.[23]

Merging five channels to obtain a spectral resolution of 2 km s^{-1} increases the signal-to-noise ratio (S/N) by a factor of $\sqrt{5} \sim 2.2$, while the spectral resolution is still adequate for the expected typical line widths of 5–25 km s^{-1} in ammonia emission.

2.3. Imaging

2.3.1. Deconvolution

Fourier transformation from the visibility to the image domain is performed with the task invert, which includes primary beam correction and combines the visibilities of single pointings into a mosaic. The Briggs weighting parameter is set to +2, which is close to natural weighting. The cell size (pixel size) is set to 5″ in R.A. and decl., which oversamples the minor axis of the synthesized beam (24″8 × 16″9, 89°3 at 25.1 GHz) by a factor >3. At lower frequency, the beam size grows up to 26″2 × 17″8 at 23.7 GHz, which results in a

---

[23] http://www.splatalogue.net

Table 1
For Each Ammonia Transition (1), We Detail the (2) Rest Frequency, (3) Excitation Energy of the Upper Transition State, (4) Natural Weighted Beam Sizes ($b_{\mathrm{maj}} \times b_{\mathrm{min}}$), (5) Beam Position Angle, rms Noise for a Channel Width of 2 km s^{-1} in the Two Regions of (6) Normal (σ_{normal}) and (7) Elevated Noise (σ_{high})

Transition	Frequency (GHz)	E_u/k_{B} (K)	Beam Size ($''$)	PA ($°$)	σ_{normal} (mJy beam^{-1})	σ_{high} (mJy beam^{-1})
(1)	(2)	(3)	(4)	(5)	(6)	(7)
NH$_3$ (1, 1)	23.69451	24.4	26.2 × 17.8	89°3	13.4	19.4
NH$_3$ (2, 2)	23.72263	65.6	26.2 × 17.8	89°3	13.1	19.3
NH$_3$ (3, 3)	23.87013	124.7	26.0 × 17.7	89°3	13.1	18.6
NH$_3$ (4, 4)	24.13942	201.7	25.7 × 17.5	89°3	12.9	16.1
NH$_3$ (5, 5)	24.53299	296.5	25.3 × 17.2	89°3	12.0	16.2
NH$_3$ (6, 6)	25.05603	409.2	24.8 × 16.9	89°3	13.2	16.2
mean value					13.0	17.6

Note. σ_{normal} is relevant for most of the maps beside the two outermost strips (see Figure 2) on each side that are described by σ_{high}. Given values are an average over 20 (σ_{normal}) and 12 (σ_{high}) measurements in two channels at ±150 km s^{-1} relative to the rest frequency.

variation of linear size of ~5% between NH$_3$ (1, 1) and (6, 6). These beam size are ~1.7 and ~1.2 times the naively expected size of ~$15'' \times 15''$ due to weighting. Table 1 lists the obtained beam sizes for NH$_3$ (1, 1) to (6, 6).

Each pointing is imaged over 512 pixel (FOV 42′7) and then integrated linearly into the mosaic with another weighting function that smooths noise across regions of differing pointing coverage (MIRIAD default method, Sault et al. 1996).

The extended emission of most spectral lines is generally better deconvolved by an algorithm that also uses extended sources for modeling. The only possibility of extended modeling that MIRIAD offers is the maximum entropy method (MEM). Our tests with the mosaic versions of MEM (mosmem) and clean (mossdi) on SWAG data confirmed that more extended emission was reconstructed by MEM over regular clean.

A first run with up to 10 iterations deconvolves the dirty image well enough to construct a mask that prevents treating regions without significant emission. Image restoration is done with restor. A mask is calculated to contain all pixels with S/N above ~5, which corresponds to 65.0 mJy beam^{-1} in the semi-cleaned image.

Deconvolution is then repeated with 50 iterations in mosmem only inside the pixels that were set as relevant by the mask. The restored images still contain sidelobe structures, especially around strong sources and in strong lines. The difficulty of obtaining better images with mosmem is described in more detail in Appendix B.

The root mean square (rms) noise is not constant within and across the data cubes, but increases slightly with decreasing frequency because of the proximity to an atmospheric water line that increases the telescope's system temperature. At a level of ~13.0 mJy beam^{-1}, the difference between the channels at -150 km s^{-1} and $+150$ km s^{-1} relative to rest frequency is 0.1–0.6 mJy beam^{-1} for the ammonia lines listed in Table 1. Thus, a common value is calculated as the mean of minimum and maximum noise measurements. The spatial variation of noise across pointings is negligible except for the two outermost strips of the data considered in this work (10/11 and 30/31, see Figure 2), which show increased noise levels in

the 2014/2015 data that are due to bad weather. Hence, two values σ_{normal} and σ_{high} are needed to describe the noise properties in the inner map and the l^+/l^- edges, respectively. Table 1 lists these noise levels for the six metastable ammonia lines. Any further mention of noise refers to σ_{normal} as only two major molecular clouds (Sgr B2 and Sgr C) are located in the region of elevated noise, and they are strong sources with high S/N.

2.3.2. Masking of the Convolved Data Cubes

The outer edges of all data cubes exhibit a $\sqrt{3}$ higher noise than the rest of the maps because of non-overlapping pointings. These edges are blanked from the edge inward by ~$50''$ and ~$100''$ (~one-third and two-thirds of the primary beam, respectively) as the smaller radius of $50''$ proved to be enough to exclude any visible higher noise edges in ammonia distribution maps, whereas spectral fitting is affected by increased noise to ~$90''$ from the edge.

2.3.3. Moment Maps

Data cubes were collapsed along the spectral axes with the task moment in MIRIAD to obtain moment maps. Map edges are blanked with the $50''$ edge mask and noise is excluded at levels of 3σ and 5σ for intensity maps (peak intensity; moment 0, integrated intensity) and velocity maps (moment 1, intensity-weighted mean velocity; moment 2, velocity dispersion), respectively.

2.3.4. Position–Velocity Diagrams

Position–velocity cuts through the restored datacube edge masked at $100''$ were calculated with the task impv in the CASA software package[24] (McMullin et al. 2007) along Galactic longitude, averaging over all emission in Galactic latitude.

3. Results

Figures in this section show NH$_3$ (3, 3) as representative of all six observed metastable ammonia inversion lines as it is typically the brightest ammonia line observed with SWAG. The corresponding figures for NH$_3$ (1, 1), (2, 2), (4, 4), (5, 5), and (6, 6) can be found in Appendix A.

3.1. Data Cubes

Channel maps of 2 km s^{-1} width in steps of 15 channels (30 km s^{-1}) are shown in Figure 5. All velocities are specified in the LSRK frame using the radio approximation. Emission can be detected in the range of ~-180 km s^{-1} to ~150 km s^{-1} with emission related to the ring-like feature between ~-150 km s^{-1} and ~120 km s^{-1}. Extended gas clumps at $l \sim 0°$, $b \sim 0°15$ are offset in velocity from the surrounding gas and are detected among the highest velocity gas in the field of view. Typical flux density values for molecular clouds in the NH$_3$ (3, 3) line are on the order of a few hundred mJy beam^{-1} with peaks of 4.23 Jy beam^{-1} (19.6 K) in the 20 km s^{-1} cloud and 5.28 Jy beam^{-1} (24.8 K) in Sgr B2. The spatial distribution is very similar among the ammonia lines, despite the varying flux density levels (Sections 5 and A.1).

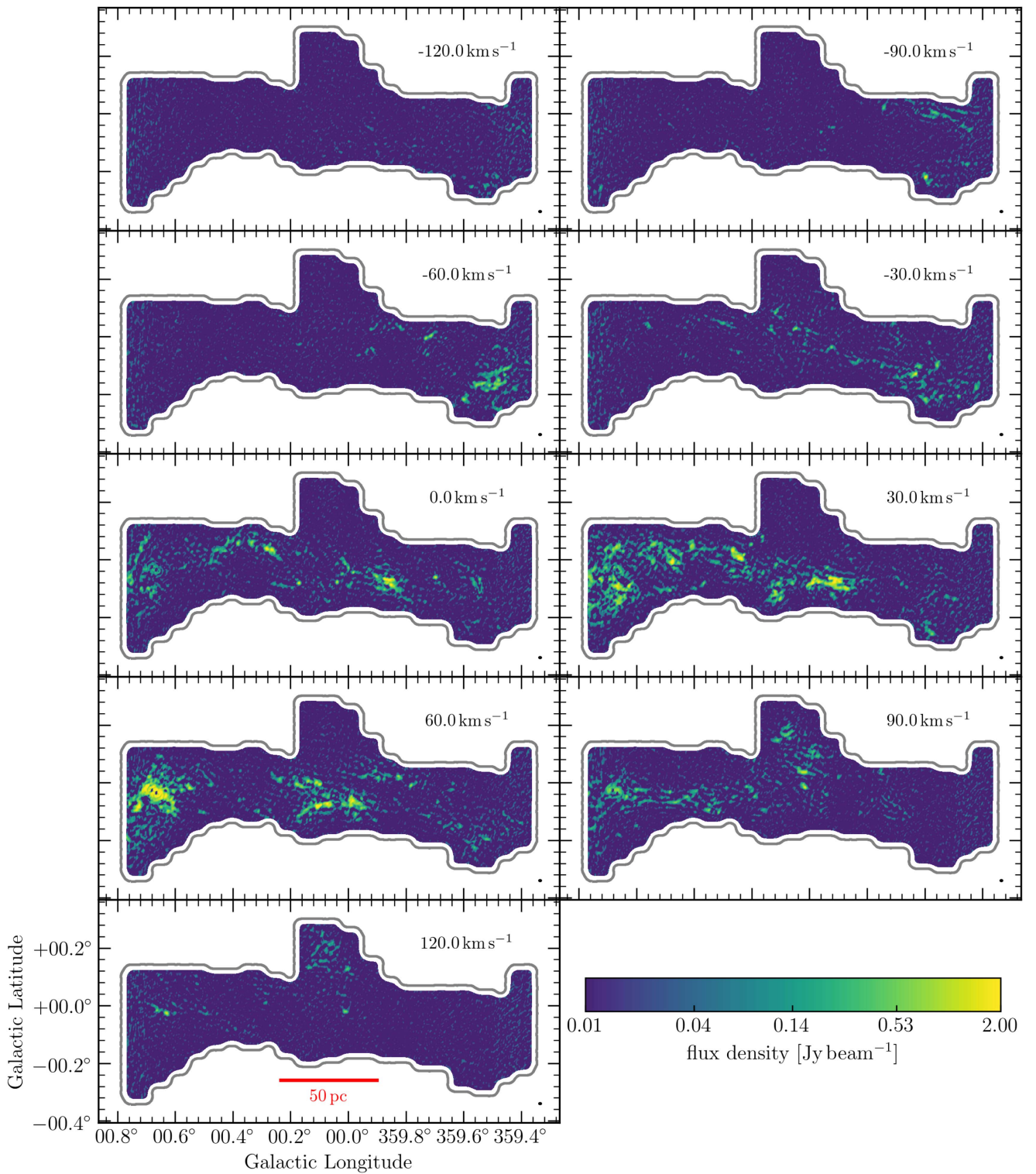
[24] Common Astronomy Software Applications, https://casa.nrao.edu/.

Figure 5. Channel maps of NH_3 (3, 3). Every fifteenth channel of 2 km s^{-1} (separated by 30 km s^{-1}) in the range of -120 km s^{-1} to $+120$ km s^{-1} is shown. Velocity and beam ($26\rlap{.}''03 \times 17\rlap{.}''71$, $89\rlap{.}°3$) are indicated in the top and bottom right corners, respectively. The conversion factor from flux density to brightness temperature for this beam size at 23.87 GHz is T [K]$/S$ [Jy beam^{-1}] = 4.65.

3.2. Sample Spectra

Depending on the structure of the source and the spectral line, hyperfine satellite components and multiple components along the line of sight are detected. A bright single-component example spectrum of NH_3 (3, 3) is shown in Figure 6 toward the Brick

(G0.253+0.016). Absorption against continuum supposedly from free–free emission is detected toward the 50 km s^{-1} cloud, the Brick, clouds c and f, and some smaller clouds in the l^+, b^- and l^-, b^+ portions of the "ring" (cf. Figure 1).

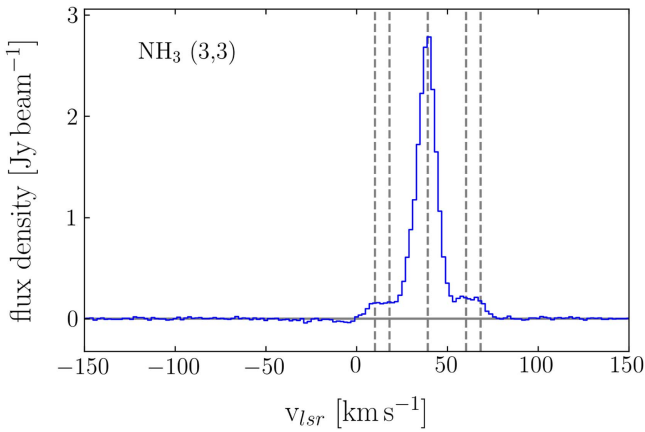Further spectra at the same position in the Brick for NH_3 (1, 1) to (6, 6) are shown in Appendix A.2.

Figure 6. Sample spectrum toward the Brick ($l = 0°.2328$, $b = 0°.0107$) extracted from the NH$_3$ (3, 3) cube. rms noise is 13.1 mJy beam^{-1} (0.061 K). The positions of the hyperfine satellites according to Table 3 are indicated by dashed vertical lines. Note the broad line width that blends the outer hyperfine components (which have separations of ±21.1 km s^{-1} and ±29.1 km s^{-1} from the main line) into a pedestal.

3.3. Image Moments

Image moment maps are shown in Figure 7 for orders 0 (integrated intensity), 1 (velocity centroid), and 2 (velocity dispersion); the top panel shows the peak intensity.

Peak intensity (Figure 7(a)) and integrated intensity (Figure 7(b)) show an almost identical distribution of emission, with Sgr C being a notable exception of strong peak but low integrated intensity, indicating narrow line widths. Sgr B2, the arching structure of the dust ridge ($0°.2 < l < 0°.6$) and the sequence of massive clouds at $-0°.2 < l < 0°.15$ with a bifurcation[25] at $l \sim 0°.1$ are most prominent in both intensity maps. The line-of-sight velocity (Figure 7(c)) shows a complex pattern at $0°.0 < l < 0°.2$ of multiple partially overlapping emission components along the line of sight. At negative longitudes, the coherent structure of negative velocities is intermingled with clouds at positive velocities. In total, the molecular arcs trace an apparently ring-like structure. As the interferometer filters out diffuse emission, the molecular clouds in this ring-like structure must be rather clumpy, which has been reported previously (Bally et al. 2010; Molinari et al. 2011; Ott et al. 2014; Ginsburg et al. 2016).

Using the definition $l^{+/-}$ and $b^{+/-}$ denoting positive/negative values of Galactic longitude and latitude, the general sense of rotation in the CMZ is consistent with the scenario $[l^-, 0] \rightarrow ([l^-, b^-] \rightarrow [0, 0] \rightarrow [l^+, b^+] \rightarrow [l^+, 0] \rightarrow [l^+, b^-] \rightarrow [0, 0] \rightarrow [l^-, b^+]$ found in previous studies (e.g., Molinari et al. 2011; Kruijssen et al. 2015; Ginsburg et al. 2016). This, however, does not necessarily mean that arcs are physically connected, e.g., note the 50 km s^{-1} jump between $[l^-, b^-]$ and $[l^+, b^+]$, but indicates that the bulk of the gas is following the same sense of rotation. Typical velocity dispersions in the moment-2 map are found to be 5–25 km s^{-1}, but velocity dispersions for individual clouds are expected to be lower because of multiple components along the line of sight, and for the lower excitation states, blending of hyperfine components.

Moment maps of NH$_3$ (1, 1) to (6,6) are shown in Appendix A.3.

3.4. Structure in Position–Velocity Space

A position–velocity diagram along Galactic longitude integrated over Galactic latitude traces the ring-like structure in the CMZ (Figure 8), which can be seen as roughly parallel structures traversing the diagram diagonally. A detailed analysis of the spatial and kinematic structure is given in Section 4.2.2 based on fit-derived kinematics.

4. Analysis: Pixel-by-pixel Hyperfine Structure Fitting

Several basic cloud properties can be derived from the metastable ammonia inversion lines (Ho & Townes 1983). The tunneling frequency of the nitrogen atom through the plane of three hydrogen atoms (inversion) depends on the rotational state (J, K) of the molecule. The population of these states is temperature dependent according to a Boltzmann law. For each rotational state J (angular momentum), there exists another ladder of states with quantum number K (angular momentum projected onto the symmetry axis). Each state decays quickly down the K-ladder to the lowest energy state ($J, K = J$), e.g., NH$_3$ (1, 1). These states are metastable as they can only deexcite through forbidden transitions if the density is too low for collisional deexcitation and thus live long enough to be commonly observable in the ISM. The inversion lines are further split into hyperfine structure lines by the interaction of the electric quadrupole moment of the nitrogen atom with the electric field of the molecule's electrons, which allows the derivation of gas opacity from the ratio of hyperfine components. Fits of the entire line structure of at least two metastable ammonia lines thus yield opacity-corrected column density, line-of-sight velocity, line width, and rotational temperature. The rotational temperature is a lower limit and can be used to estimate the kinetic gas temperature up to approximately the line excitation energy via model-derived conversion functions.

Details on the ammonia thermometer, the derivation of opacity-corrected column density, rotational temperature, and its conversion into kinetic gas temperature are described in Appendix C.

4.1. Hyperfine Structure Fitting in CLASS

In order to derive gas temperatures without having to assume optically thin emission, we need to know line temperatures, line widths, and opacities. We derive these quantities by fitting the ammonia hyperfine structure with the CLASS[26] package in GILDAS.[27] The 100″ edge-masked data cubes were masked at 3σ per channel and 5 Jy beam^{-1} km s^{-1} in integrated flux density to ensure sufficient S/N for successful fits. Fitting is made with the CLASS functions `method nh3(j,j)` and `minimize` for $J = 1, 2, 3$. The higher transitions $J = 4, 5, 6$ are not implemented but can be fitted with the `method hfs` using the relative positions and strengths of the ammonia hyperfine structure components of Townes & Schawlow (1975; listed in Table 3). The fitting algorithm is constrained to line opacities in the range $0.1 \leqslant \tau \leqslant 30$, which introduces a factor of

$$\lim_{\tau \to 0} \frac{0.1}{\tau} \frac{1 - e^{-\tau}}{1 - e^{-0.1}} = 1.051 \qquad (1)$$
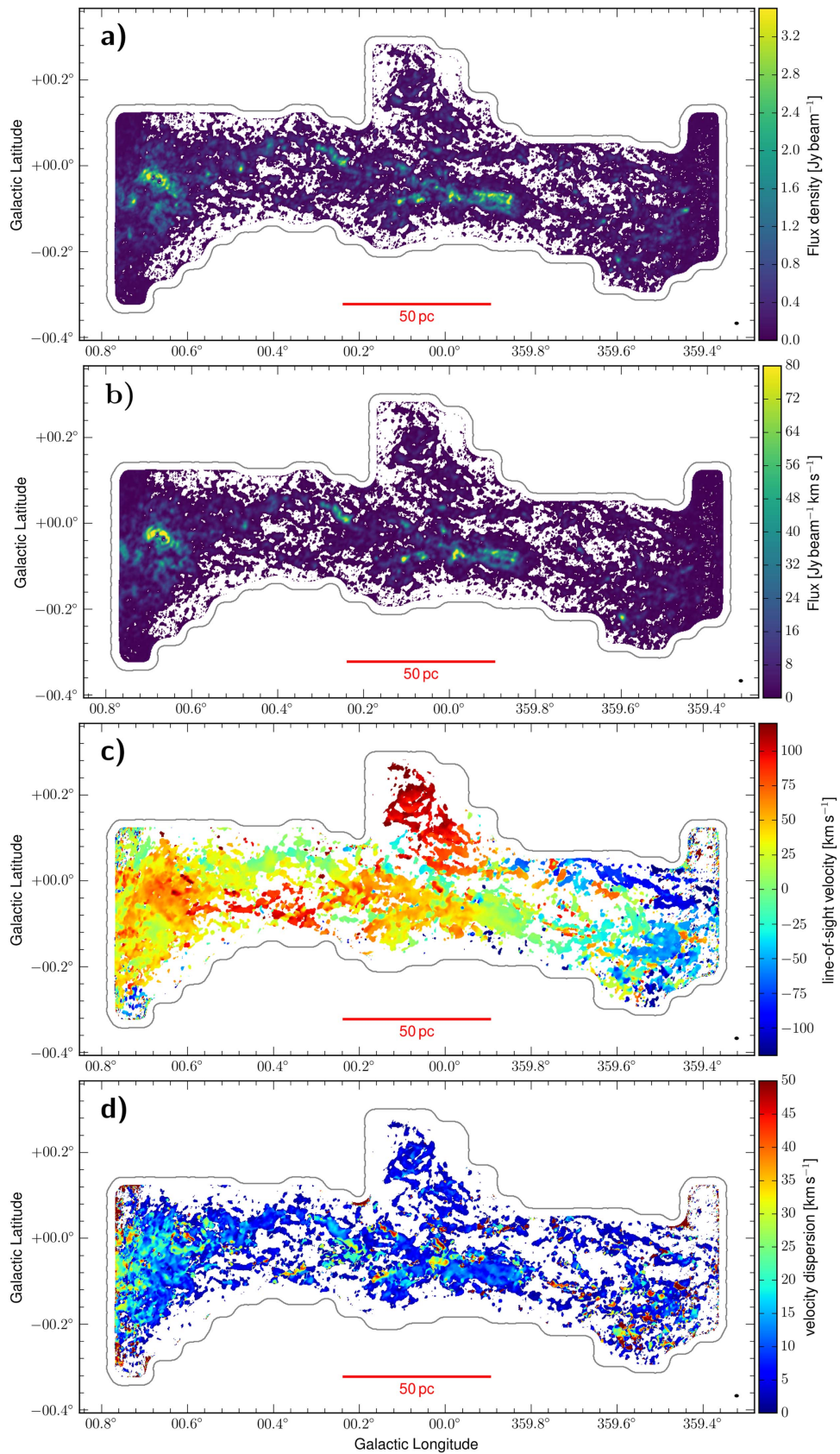

Figure 7. NH_3 (3, 3) moment maps: (a) peak intensity, (b) integrated intensity (moment 0), (c) intensity-weighted mean velocity (moment 1), and (d) intensity-weighted velocity dispersion (moment 2). The intensity maps (a) and (b) are masked at 3σ, and velocity maps (c) and (d) are masked at 5σ with an rms noise of $\sigma = 13.1$ mJy. The beam of $26\rlap{.}''0 \times 17\rlap{.}''7$ (1.05 pc $\times$ 0.71 pc) is indicated in the lower right-hand corner of each panel.
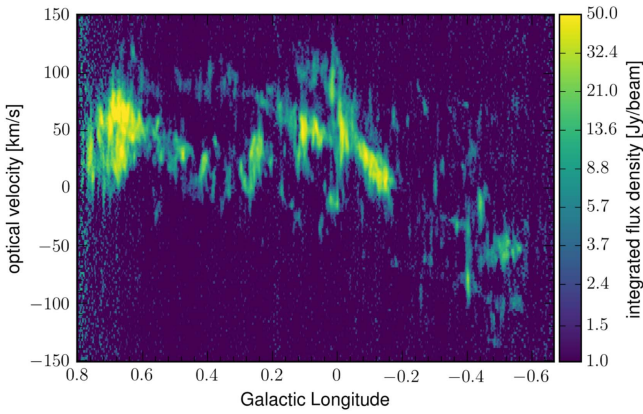
Figure 8. Position–velocity diagram along Galactic longitude, integrated over Galactic latitude.
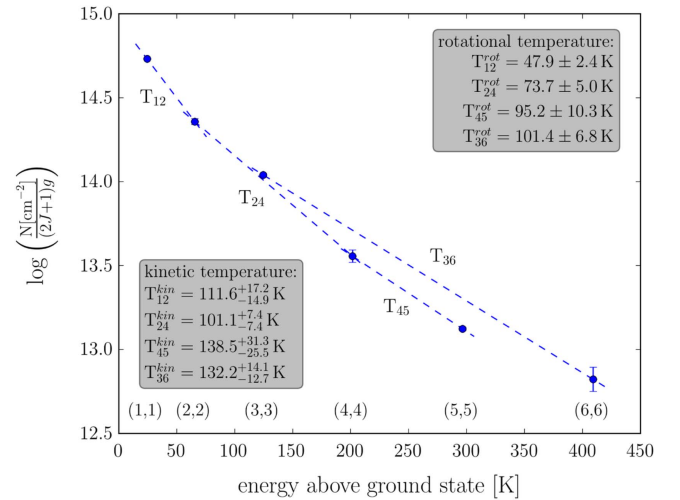

Figure 9. Typical Boltzmann plot (excitation state-scaled column density as a function of excitation temperature or energy above ground state) of ammonia emission in the Brick. Four temperature estimates (proportional to the inverse slope) are sketched and listed in the two boxes. Typical errors are 5%–10% in rotational and 10%–25% in kinetic temperature with increasing uncertainty for higher kinetic temperatures owing to the flattening of the $T_{\rm kin}-T_{\rm rot}$ conversion (Table 4; Morris et al. 1973; Ott et al. 2011; Gorski et al. 2017).

relative to the line temperature of optically thin emission ($\tau \to 0$). This deviation by up to 5.1% is small compared to the general flux density uncertainties of $\sim$15% (Figure 4) and can be neglected. The fit is further constrained to the strongest emission component along the line of sight. Occasionally, unsuccessful fits occur through blending of closely spaced emission components. These are discarded based on reduced χ^2 (CLASS parameter `lineRMS` > 0.1), physically implausible values (Δv(FWHM) $> 50.0\,{\rm km\,s^{-1}}$), and the very large error of the fitted parameter ($\Delta(v_{\rm los}) > 10.0\,{\rm km\,s^{-1}}$, $\Delta(\Delta v) > 10.0\,{\rm km\,s^{-1}}$). Examples and statistics of the hyperfine structure fitting can be found in Appendix D.

4.1.1. Sample Boltzmann Plot

A Boltzmann plot (Appendix C.1, cf. Goldsmith & Langer 1999), typical for the ammonia emission in the GC, is shown in Figure 9. The observed shapes do not follow a single linear relation, but become more shallow around NH$_3$ (3, 3) to NH$_3$ (4, 4), which can be due to the nonlinear $T_{\rm kin}-T_{\rm rot}$ conversion or be indicative of a multiple temperature medium, as is already known in the literature (e.g., Hüttemeister et al. 1993; Mills & Morris 2013). Errors in derived column density are typically small ($\Delta N_{\rm u}/N_{\rm u}$ on the order of a few percent) but larger (a few tens of percent) at the edges of clouds because of the lower S/N, which allows the derivation of accurate temperatures of typically 5%–10% relative error ($T_{\rm rot}$) and 10%–25% after conversion into kinetic temperature. Additionally, the $\sim$15% flux density error (Figure 4) contributes to the column density errors.

4.2. Results of the Hyperfine Structure Fitting

As in Section 3, only NH$_3$ (3, 3) is shown to illustrate features common in all observed ammonia lines. As a representative temperature measure, we choose to show T_{24} calculated from NH$_3$ (2, 2) and NH$_3$ (4, 4). The strongest line, NH$_3$ (3, 3), yields the temperature T_{36}, which suffers larger relative errors than T_{24} because of the low intensity of the NH$_3$ (6, 6) emission. We also calculate T_{12} and T_{45}. Other combinations, like T_{23}, cannot be calculated because NH$_3$ (2, 2) is a para state (one hydrogen nuclear spin antiparallel), while NH$_3$ (3, 3) is an ortho state (all hydrogen nuclear spins parallel). Generally, NH$_3$ (i, i) with $i = 3n$ (n integer) are ortho,

the others are para states. As the relative abundance of ortho versus para ammonia is not known, temperatures can only be estimated from two para states or two ortho states. For T_{12}, the $T_{\rm rot} - T_{\rm kin}$ conversion (Table 4 and Figure 5 in Ott et al. 2011; see also Morris et al. 1973) flattens, which prevents a reliable derivation of temperatures above $\sim$50–60 K. T_{24}, T_{45}, and T_{36} do not suffer such problems (Gorski et al. 2017) and yield very similar results. The corresponding maps for T_{12}, T_{45}, and T_{36} can be found in Appendix E.

4.2.1. Column Density

The NH$_3$ (3, 3) column density N_l (Figure 33) traces much of the ring-like gas stream by construction of the mask applied before hyperfine structure fitting. A peak of $N_{33} = 7.7 \times 10^{15}$ cm^{-2} is reached in Sgr B2. Massive clouds like the Brick, G+0.10–0.08, and the 20 km s^{-1} cloud are also found to have high column densities ($N_{33} \gtrsim 1.5 \times 10^{15}$ cm^{-2}), while NH$_3$ (3, 3) is not largely excited and detected at column densities $\lesssim 1.5 \times 10^{15}$ cm^{-2}. The NH$_3$ (1, 1) column density reaches a maximum of 1.2×10^{16} cm^{-2} in Sgr B2, where NH$_3$ (6, 6) is still detected at up to 2.6×10^{15} cm^{-2}.

The total ammonia column density as derived from Equation (22) (Figure 10) shows a similar picture as the NH$_3$ (3, 3) column density. The highest column densities are reached in Sgr B2 (6.8×10^{16} cm^{-2}), the Brick (3.9×10^{16} cm^{-2}), and the 20 km s^{-1} cloud (3.0×10^{16} cm^{-2}), whereas most smaller clouds along the "ring" have $N_{\rm tot} \lesssim 1.0 \times 10^{16}$ cm^{-2}. The clouds at $l \sim 0°.1$, $b \sim 0°.2$ show the lowest detected column densities ($1.0 \times 10^{15} \lesssim N_{\rm tot}$ cm$^{-2} \lesssim 2.5 \times 10^{15}$) of clouds that do not fall below the fitting thresholds. Other clouds of this size typically exhibit column densities that are higher by a factor of 2–3. A small cloud of high column density is located at $l = -0°.40$, $b = -0°.22$ with $N_{\rm tot}$ up to 2.6×10^{16} cm^{-2} ($N_{33} = 6.4 \times 10^{15}$ cm^{-2}) and surrounded by gas of $N_{\rm tot} \sim 10^{16}$ cm^{-2}. This cloud is assumed to lie in the foreground (Longmore et al. 2013b) and is discussed to be influenced by an

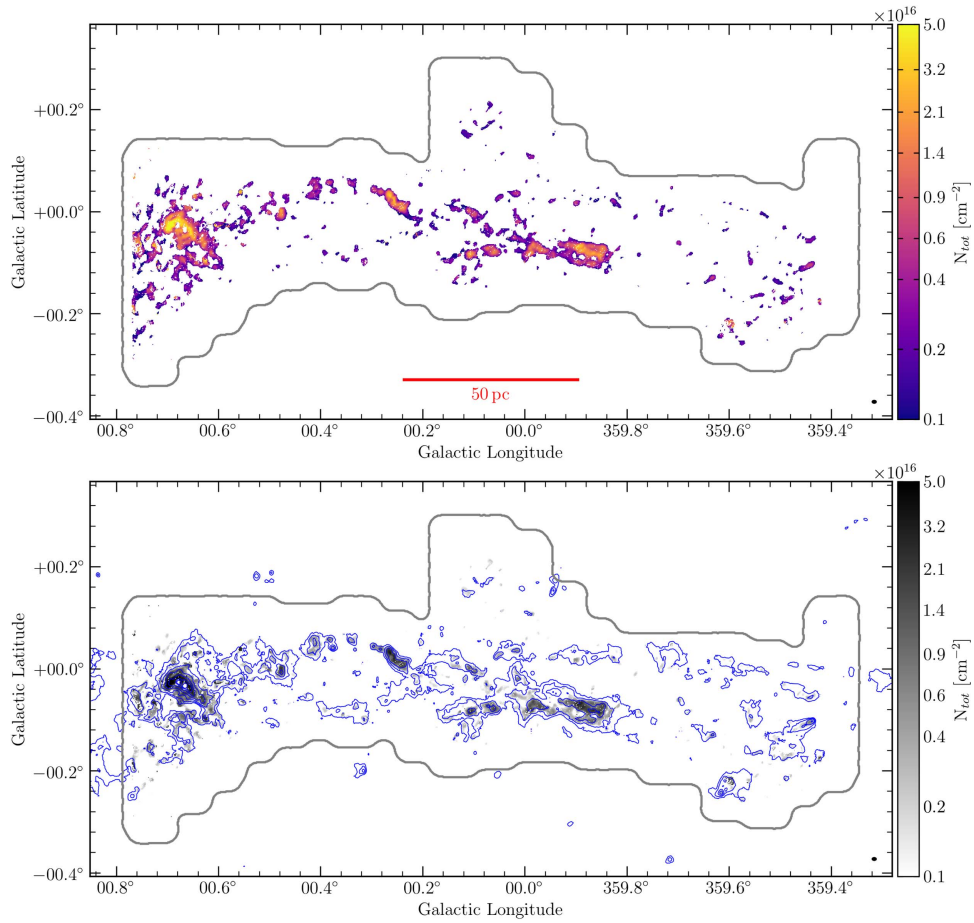**Figure 10.** Top: total ammonia column density according to Equation (22). The dynamical range is $\sim 5 \times 10^{15}$ cm^{-2} to $\sim 6.8 \times 10^{16}$ cm^{-2}. In warm clouds like Sgr B2, this figure represents a lower limit as the unobserved states $J > 6$ can be populated in non-negligible fractions (Mills & Morris 2013). Bottom: the same map of the total column density overlaid with 870 μm dust emission from ATLASGAL (Schuller et al. 2009) at contours of powers of two (1, 2, ..., 64) Jy beam^{-1}. The ammonia distribution closely follows dust emission in regions of high ammonia column density ($\gtrsim 1 \times 10^{16}$ cm^{-2}).
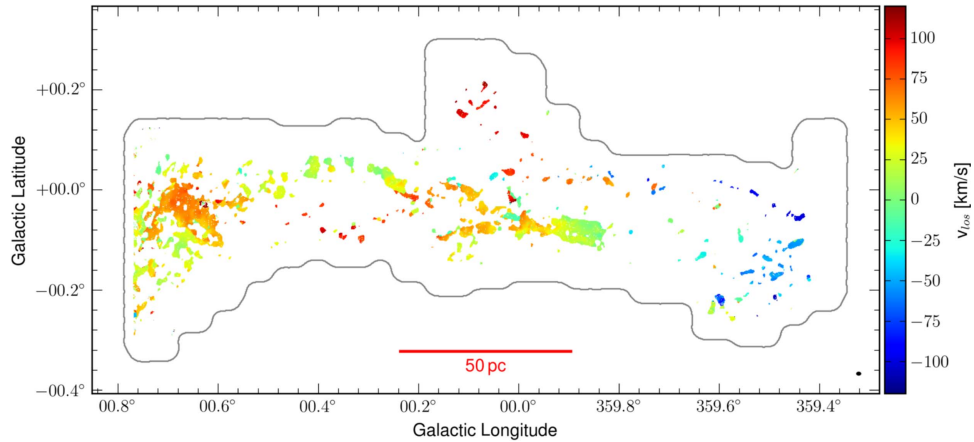

Figure 11. NH$_3$ (3, 3) line-of-sight velocity derived from fitting the hyperfine structure.

intermediate mass black hole (Oka et al. 2016) because of its unusually high CO velocity dispersion.

The ammonia distribution as traced by the NH$_3$ column density map closely follows 870 μm dust emission obtained by ATLASGAL (Schuller et al. 2009), as can be seen in Figure 10 (bottom). The correlation is most pronounced for gas at higher column density than $\sim 1 \times 10^{16}$ cm^{-2}. Lower column density gas is mostly found in regions of weak dust emission, but the presence of dust does not imply the detection of ammonia at $N_{\rm tot} \gtrsim 2 \times 10^{15}$ cm^{-2}. Almost all (dense) ammonia gas is accompanied by dust emission. Notable exceptions from the overall good correlation are found in Sgr B2 and Sgr A*. Sgr B2 (N) and Sgr B2 (M) are detected in absorption in ammonia, whereas the dust emission peaks at these locations.
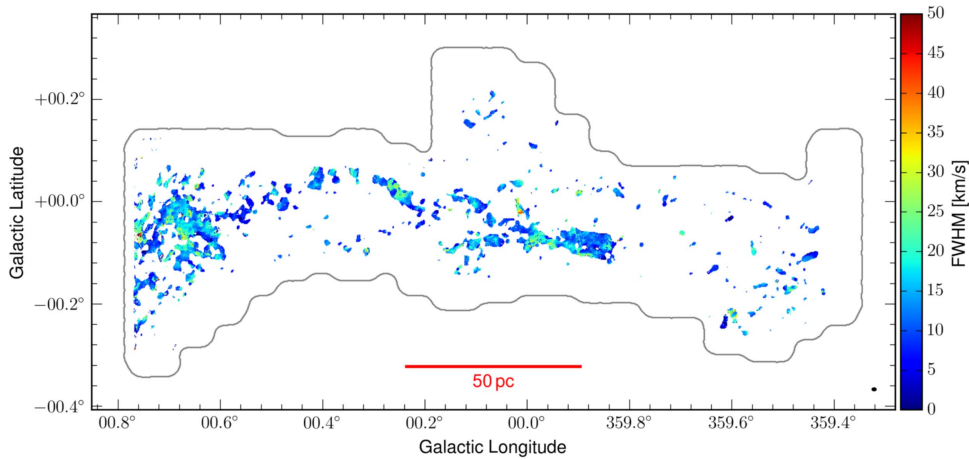
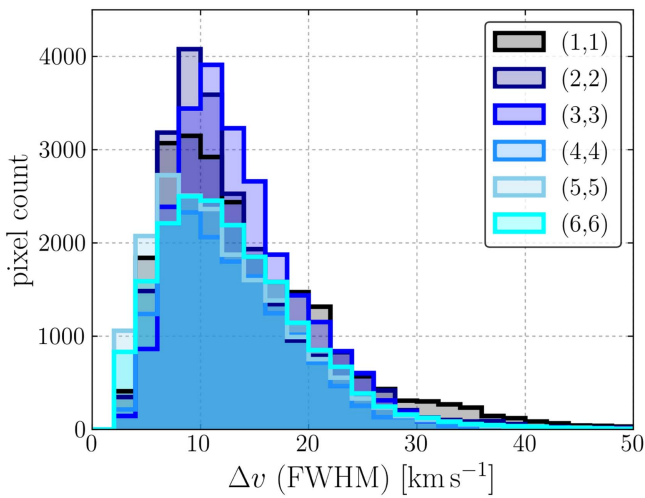**Figure 12.** NH$_3$ (3, 3) line width (FWHM) derived from fitting the hyperfine structure.

Figure 13. Distribution of FWHM of metastable ammonia hyperfine lines in the GC. The bin size of 2 km s^{-1} corresponds to the spectral resolution of the data cubes.

All of Sgr B2 that is detected in emission, however, does correlate very well with the 870 μm contours. At Sgr A*, the 870 μm emission locally peaks, but the ammonia column density is $\ll 1 \times 10^{15}$ cm^{-2} as this region falls below the selection thresholds for hyperfine structure fitting. The emission from Sgr A* at submm is contributed by optically thick synchrotron emission rather than thermal dust emission, and no correlation is observed.

4.2.2. Kinematics

The fit-derived line-of-sight velocity of NH$_3$ (3, 3), shown in Figure 11, generally agrees well with the moment-1 map (Figure 7(c)). Owing to the constraints for successful fitting (Section 4.1), the mapped area is considerably smaller. Significant differences between the two maps are not detected, which confirms that "successful" fits are indeed correct and potential "bad" fits were excluded.

The line widths of the fitted map (Figure 12) and the moment-2 map (Figure 7(d)) qualitatively agree about regions of higher or lower line width, but show very different quantitative results. After correcting for the conversion between FWHM (fitted map) and velocity dispersion σ

(moment map), a typical factor of ∼1.5–2 (coresponding to differences of <10 km s^{-1}) remains, but extended regions all across the CMZ display factors of 3–5 (differences of 20 km s^{-1} up to >50 km s^{-1}). The larger line widths are derived from the moment map in all cases, meaning the image moment analysis overestimates the line width with respect to line fitting. This is partly due to unaccounted blending of hyperfine structure and mostly caused by multiple line-of-sight components in the moment map. Henshaw et al. (2016b) find similar differences between these two line width estimates in the CMZ based on HNCO data. Depending on the number of detected emission components along the line of sight, their median difference varies between 3.4 km s^{-1} (single component) and 18.8 km s^{-1} when four components are present. The maps derived from hyperfine structure fitting are thus considered to be more reliable than the simple moment analysis when investigating the kinematics, although fitting discards all but the strongest component along the line of sight, introducing a bias toward strong sources.

The distribution of fitted line widths for all ammonia transitions is shown in Figure 13 and shows a typical line width of 8–16 km s^{-1} consistently for all six observed ammonia lines. The peak of the distribution is located at 8–10 km s^{-1}, and only NH$_3$ (3, 3) has its peak at a slightly higher velocity of 10–12 km s^{-1}.

4.2.3. Opacity

The opacity map of NH$_3$ (3, 3) (Figure 14) shows that a significant number of fitted pixels of the six ammonia species exhibit opacities $\tau \gtrsim 1$, where the often used assumption of optically thin emission does not hold anymore. This is the case not only in the very high column density clouds (like Sgr B2 and the Brick), but also in other dust ridge clouds and the inner regions of smaller clouds at negative longitudes and the far side of the "ring" (l^+, b^-). A weak correlation between high column density (Figure 33) and high opacity (Figure 14) is found in the Brick, G+0.10 + 0.00, the 20 and 50 km s^{-1} clouds, and the foreground cloud G-0.40-0.20. Other clouds are optically thin at low column density or do show high opacity despite having low column density ($N_{u,33} < 2.5 \times 10^{15}$ cm^{-2}, e.g., G0.50 +0.05 or G-0.60-0.09), which is indicative of a smaller filling fraction of clumpy gas. High opacities, especially in very small regions, must be taken with care as the edge of a region corresponds to a low S/N ($\gtrsim 3\sigma$, see Section 4.1 for details),
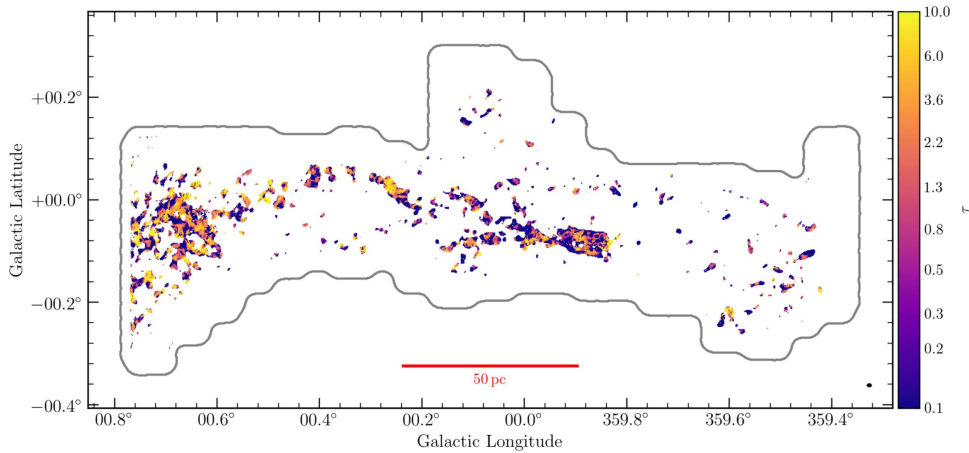
Figure 14. NH_3 (3, 3) opacity derived from fitting the hyperfine structure. Large areas in CMZ clouds are not optically thick ($\tau \lesssim 1$) and either optically thin ($\tau \sim 0$) or marginally thick ($\tau < 1$). Several extreme exceptions of $\tau \gtrsim 10$ exist in the Brick, an extension to the 20 km s^{-1} cloud, and the surrounding of Sgr B2.

and thus random noise peaks may be mistaken as hyperfine structure satellite components by the fitting routine. Because of the low flux of these pixels, the derived column density is only marginally affected, but opacity, which depends on the flux ratio of hyperfine structure components, can be artificially elevated. This opacity distribution is consistent with Hüttemeister et al. (1993), who observed NH_3 (1, 1), (2, 2), (4, 4), and (5, 5) in selected clouds in the GC. In the (1, 1) line, they find "strong" sources at $\tau_{11} \sim 4$ and an average $\bar{\tau}_{11} = 2.3$ for "weak" sources, which matches our observations of $\bar{\tau}_{11} = 2.0$ (median 1.2) and $\tau_{11} \gg 1$ in clouds when considering that SWAG also observed the less dense ISM in between clouds. We can also confirm the trend to lower opacity in Hüttemeister et al. (1993) for higher-J lines as the median opacity decreases to the lower fitting limit ($\tau = 0.1$) for NH_3 (4, 4) and higher.

4.2.4. Temperature

The ammonia gas temperature as traced by kinetic temperature T_{24}, which is derived from NH_3 (2, 2) and NH_3 (4, 4), is shown in Figure 15. The typical temperature range observed in the GC is 50–120 K, only Sgr B2 is considerably hotter with $\sim$200 K.

A histogram of temperature measures T_{12}, T_{24}, T_{45}, and T_{36} is shown in Figure 16 to illustrate the temperature distribution of the CMZ. T_{12} cannot reliably trace temperatures $\gtrsim$50–60 K (see excitation energies listed in Table 1), and thus its distribution peaks at $\sim$35 K, tracing cooler molecular gas. The other three temperature measures of higher lines are reliable to at least $\sim$200 K before the rotational-kinetic conversion starts to introduce large uncertainties, and they are therefore easier to interpret. Their distributions are similar in peak temperature and spread, with T_{24} yielding higher values by $\sim$15 K. Regarding the spatial distribution, most of the gas is found at intermediate temperatures at 60–100 K and in a few hot regions $T > 150$ K.

The detection of two temperature components in the molecular gas is consistent with Hüttemeister et al. (1993), who found gas at rotational temperatures $T_{\rm rot} \sim 25$ K and $T_{\rm rot} \sim 200$ K. Our cold ($T_{\rm kin} = 25$–50 K) component is thus compatible with Hüttemeister et al. (1993) considering the rotational-kinetic temperature conversion. However, the temperature of the warm components differ significantly by a factor of $\sim$2–2.5 in rotational temperature. Ao et al. (2013) and

Ginsburg et al. (2016) derived kinetic temperatures of dense molecular gas over large areas of the CMZ based on APEX observations of H_2CO (formaldehyde). They find the gas to be warm at 50 K to $>$100 K (Ao et al. 2013) and $\sim$60 K to $>$100 K (Ginsburg et al. 2016), which is consistent with our detection of a warm gas component. Regarding the spatial distribution, the temperatures known in the literature match our results: Sgr B2 is hot at $\sim$200 K (this work), $>$150 K (Ginsburg et al. 2016); the 20 km s^{-1} and 50 km s^{-1} cloud and the Brick show temperatures of 80–100 K (this work, Güsten et al. 1981; Mauersberger et al. 1986; Ao et al. 2013; Ginsburg et al. 2016).

We estimate the fraction of cold ($\sim$35 K) and warm ($\sim$80 K) gas of the total detected ammonia column density by fitting the Boltzmann plot (Figure 9) with two components. This allows the calculation of the column density of cold and warm ammonia independently and hence the relative abundances. Over the whole CMZ, we find the mean column density fractions to be $\sim$55% and $\sim$45% for the cold and warm component, respectively. In the 20 and 50 km s^{-1} clouds, the cold component dominates at 50%–70% (mean: $\sim$68%) the relative contribution to the observed ammonia column density. In Sgr B2, a larger fraction of the column density is in the warm component, which results in both components being almost equally strong ($\sim$50% cold and warm). Mean values of $\sim$60% of the cold gas fraction are found in the dust ridge and $\sim$53% in clouds at negative longitudes (excluding the 20 km s^{-1} and 50 km s^{-1} clouds). The "Three Little Pigs" (G+0.05–0.07 "sticks," G+0.10–0.08 "stones," and G+0.15–0.09 "straw") are a group of clouds of similar global properties but very different substructure. They are also striking in the cold gas fraction $f_{\rm cold}$ as G+0.10–0.08 ("sticks") shows the highest $f_{\rm cold}$ over an extended region at $\sim$81%, whereas its neighbor G+0.05–0.07 ("stones"; $f_{\rm cold} \sim 65$%) seems inconspicuous and much closer to the CMZ mean. G+0.15–0.09, "straw," does not show up as its ammonia emission was to low to be hyperfine structure fitted. These results show that the typical gas temperature is not the same over the whole CMZ, but is either $\sim$35 K or $\sim$80 K depending on the considered region.

The relation between Hi-GAL dust temperature (Molinari et al. 2011) and ammonia gas temperature is shown in Figure 17 for T_{24}. Further tracers are shown in Appendix F. T_{24} is offset well above the one-to-one relation by a factor of $\sim$3 to $>$5. A linear best fit, calculated in bins of 1 K for
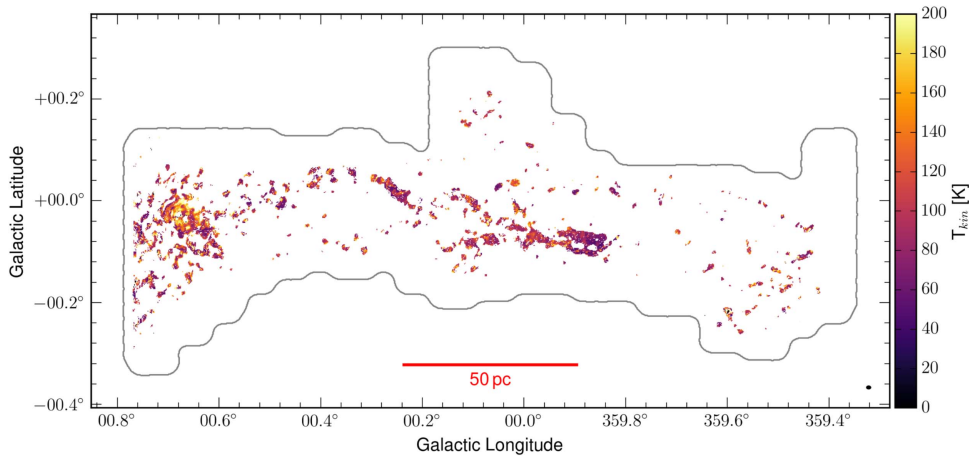
Figure 15. Kinetic ammonia gas temperature map (T_{24}) derived from NH$_3$ (2, 2) and NH$_3$ (4, 4) hyperfine structure fits.
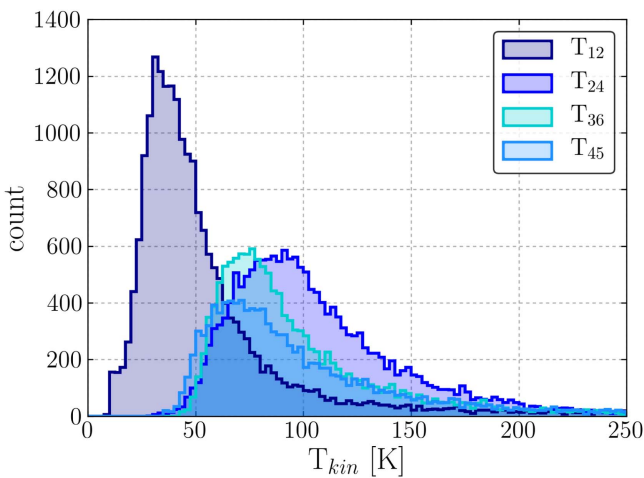

Figure 16. Distribution of temperatures in the GC as derived for four kinetic ammonia gas temperatures. The conversion of rotational to kinetic temperature is taken from Ott et al. (2011), as described in Section C. T_{ij} denotes the temperature measure derived from the lines NH$_3$ (i, i) and NH$_3$ (j, j). T_{12} is sensitive to cold gas, whereas higher lines need warmer conditions to be excited and are thus succeptible only to increasingly warm gas. T_{24}, T_{45}, and T_{36} trace similarly warm gas of >50 K.
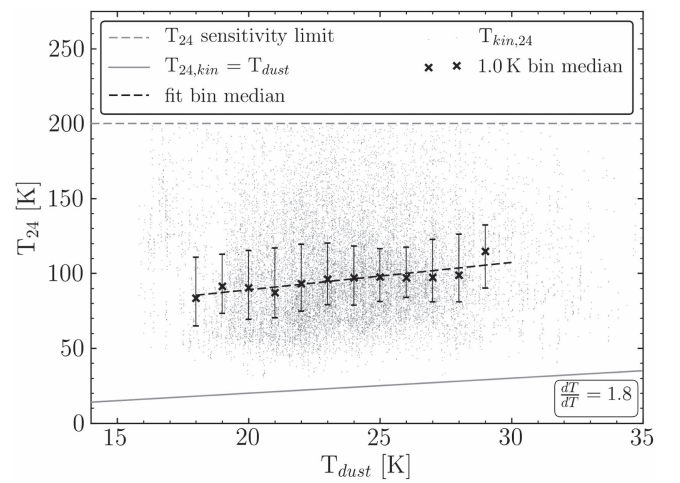

Figure 17. Correlation of Hi-Gal dust temperature (Molinari et al. 2011) and kinetic ammonia gas temperature T_{24}. Black crosses denote median T_{24} temperature in bins of 1.0 K dust temperature, which are linearly fitted (black dashed line). The errors are the range that includes 50% of measurements in the respective bin. Median temperatures are correlated despite the offset relative to $T_{24} = T_{dust}$.

18 K $\leqslant T_{dust} \leqslant$ 30 K, yields a gradient of $dT_{24}/dT_{dust} = 1.8$, and fitting without binning results in no correlation (gradient ~0.0) because of cutoff effects of the limited temperature reliability range. This result implies that in the CMZ, the same heating mechanism is likely to be responsible for both dust and gas heating although their temperatures are not coupled to the same value. This hint toward a common heating source contradicts the prediction by Clark et al. (2013), who explain the temperature structure of the Brick (G0.253+0.016) by independent heating of gas and dust by cosmic rays and an interstellar radiation field, respectively. The observed correlation is compatible with heating by turbulence on large scales and compression on cloud scales (cf. Section 5), as was also suggested by Ginsburg et al. (2016). The fact that dust acts as a coolant in the CMZ has been known in the literature for a long time (e.g., Güsten et al. 1981; Molinari et al. 2011; Ginsburg et al. 2016) and can be confirmed by our new data. Similar results are obtained for warm molecular gas traced by T_{45} and T_{36} ($dT_{45}/dT_{dust} = 2.4$, $dT_{36}/dT_{dust} = 1.4$). The cold molecular gas component (T_{12}) only weakly correlates with dust temperatures

($dT_{12}/dT_{dust} = 0.5$), which implies a temperature component that is not reflected by dust measurements.

4.2.5. Estimation of the Beam Filling Factor

A simple estimation of the beam filling factor η_f can be made based on the comparison of T_{kin} and brightness temperature T_b. For $\eta_f = 1$, both temperatures must be equal, but if the beam is partly covered by emission of temperature T_{kin} and partly by weak (i.e., cold) background, the observed T_b is lower. A first-order estimate is given by $\eta_f = T_b/T_{kin}$ under the assumptions of η_f being identical for the two lines NH$_3$ (i, i) and NH$_3$ (j, j) that define temperature T_{ij}. This furthermore assumes high optical depth and the line excitation temperatures being approximately given by T_{kin}. Typical values of dense clouds (the 20 km s^{-1} cloud, the Brick, cloud d, Sgr B2) are in the range 0.10–0.15, Sgr C and less dense clouds are covered at $\eta_f = 0.05$–0.10 (e.g., the "Three Little Pigs" G0.05–0.07, G0.10–0.08, and G0.15–0.09). G-0.40–0.25 sticks out from all other clouds at negative longitudes with $\eta_f \sim 0.10$, which is the third highest η_f observed after Sgr B2 and the 20 km s^{-1}
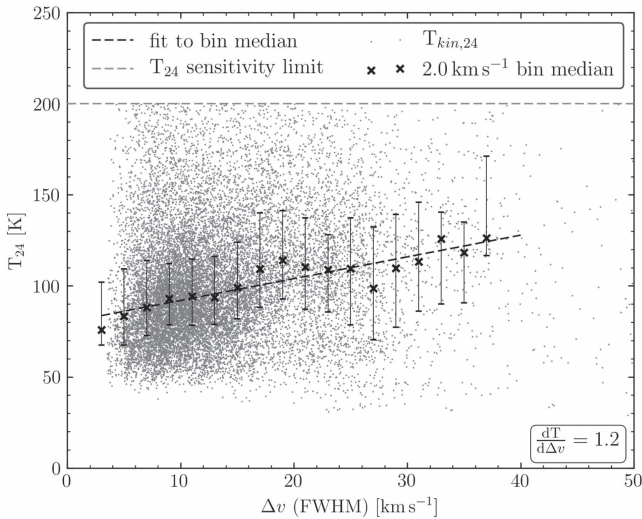
Figure 18. Kinetic ammonia temperature T_{24} as a function of line width of NH_3 (2, 2). Median temperatures in bins of 2.0 km s^{-1} width are marked by black crosses and fitted linearly. The errors are the range that includes 50% of measurements in the respective bin. A cutoff at 200 K is applied, above which the conversion of rotational into kinetic temperature becomes increasingly unreliable (Table 4, Morris et al. 1973; Ott et al. 2011; Gorski et al. 2017).
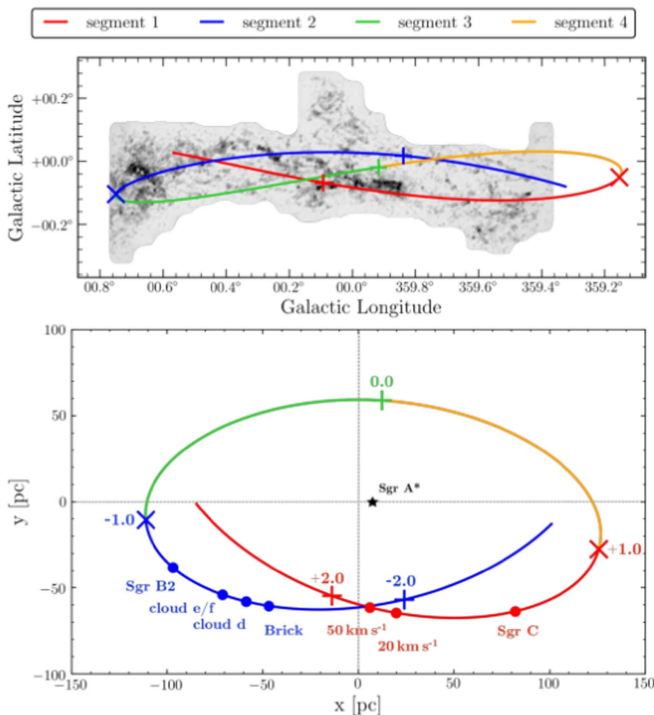

Figure 19. Overview of the stream orbit according to K15. Pericenters are marked by plus symbols, crosses denote apocenters. The bottom of the gravitational potential at Sgr A* is marked by a star. Top: projected view of the stream orbit in Galactic coordinates. Background image: SWAG NH_3 (3, 3) integrated intensity. Bottom: top-down view in physical coordinates. The observer is situated in negative y-direction. Major molecular clouds are labeled. Time since far-side pericenter passage is given for peri- and apocenters in Myr.

cloud. All other clouds show beam filling factors below 0.05. The average size of cloud substructure (clump size) for $\eta_f = 0.10$ (0.05 0.15) is then 0.27 pc (0.19 pc, 0.33 pc). This is consistent with recent interferometer measurements with the SMA and ALMA (Kauffmann et al. 2013, 2017a; Rathborne et al. 2014b; Lu et al. 2017).

4.2.6. Correlation of Fitted Parameters

Figure 18 shows the relation between line width and temperature for T_{24} and the corresponding line NH_3 (2, 2). As before, temperatures scatter between 50 K and the sensitivity cutoff at 200 K for line widths of $\sim$5 km s^{-1} to 30–40 km s^{-1} with no obvious correlation. Temperature medians in bins of 2 km s^{-1} width, however, follow a linear relation at $dT/d(\Delta v) = 1.2$. The increase in line width due to thermal broadening scales sub-linearly as $\Delta v \propto \sqrt{T}$ and is about one order of magnitude ($\Delta v_{\text{thermal}} \sim 2$ km s^{-1}) weaker than the observed linear relation. Assuming that the line width is not contaminated by blending of clouds along the line of sight, this implies that on a statistical basis, the more turbulent gas is warmer but large variations between clouds do exist, as has also previously been detected by Immer et al. (2016) and Ginsburg et al. (2016).

5. Discussion

We now compare the observations to models proposed in the literature with a focus on the stream model by K15, as introduced in Section 1. In practice, this means that positions on the sky are mapped to times and examined for consistent sequential behavior. Figure 19 offers an overview of the orbit's 3D structure, of the relation to major molecular clouds, and of evolutionary timescales.

5.1. Orbital Fitting and Statistical Analysis

The mapping of cloud positions to times in the K15 model is made in PPV space. Within $\pm$20 km s^{-1} in line-of-sight velocity and 0°.15 projected distance, a cloud is matched to the nearest point along the orbit for which time and other orbital parameters are known. The line-of-sight velocity of clouds is given by the mean velocity derived from the NH_3 hyperfine structure fits (Section 4.2.2). Clouds farther from the stream than 0°.15 in the Galactic longitude/latitude plane are considered to not belong to the stream as this is approximately the maximum spatial separation found by K15 (see their Figure 4). Out of the 24383 fitted pixels, we match 19453 pixels to the stream (79.8%), while 4930 pixels (20.2%) contain emission from clouds that are not related to the gas stream.[28]

We examine the kinetic ammonia temperatures T_{24}, T_{45}, and T_{36}, as well as column density and line width of the six metastable inversion lines covered by SWAG along the stream. Medians are calculated in bins of 0.01 Myr if the bin contains more than 10 members, and therefore the sample size is large enough for the median to be considered robust against outliers. Errors to the medians are given by the range that includes the central 50% of all measurements in the respective bin. The resulting time dependencies of physical parameters are assessed by fitting linear functions to the medians if a trend is apparent.

5.2. Time Dependencies

The time dependencies of kinetic temperature T_{24}, column density, and line width of NH_3 (3, 3) are shown in the following sections to represent results that appear in all of the ammonia temperature measures (T_{24}, T_{45}, T_{36}) or ammonia inversion lines ($J = 1, ..., 6$) if not explicitly noted otherwise. Plots of the other

---

[28] This gas is mostly located on the polar spur at $l \sim 0$ and in the surrounding of Sgr B2 and thus too far ($>$0°.15) from the stream.
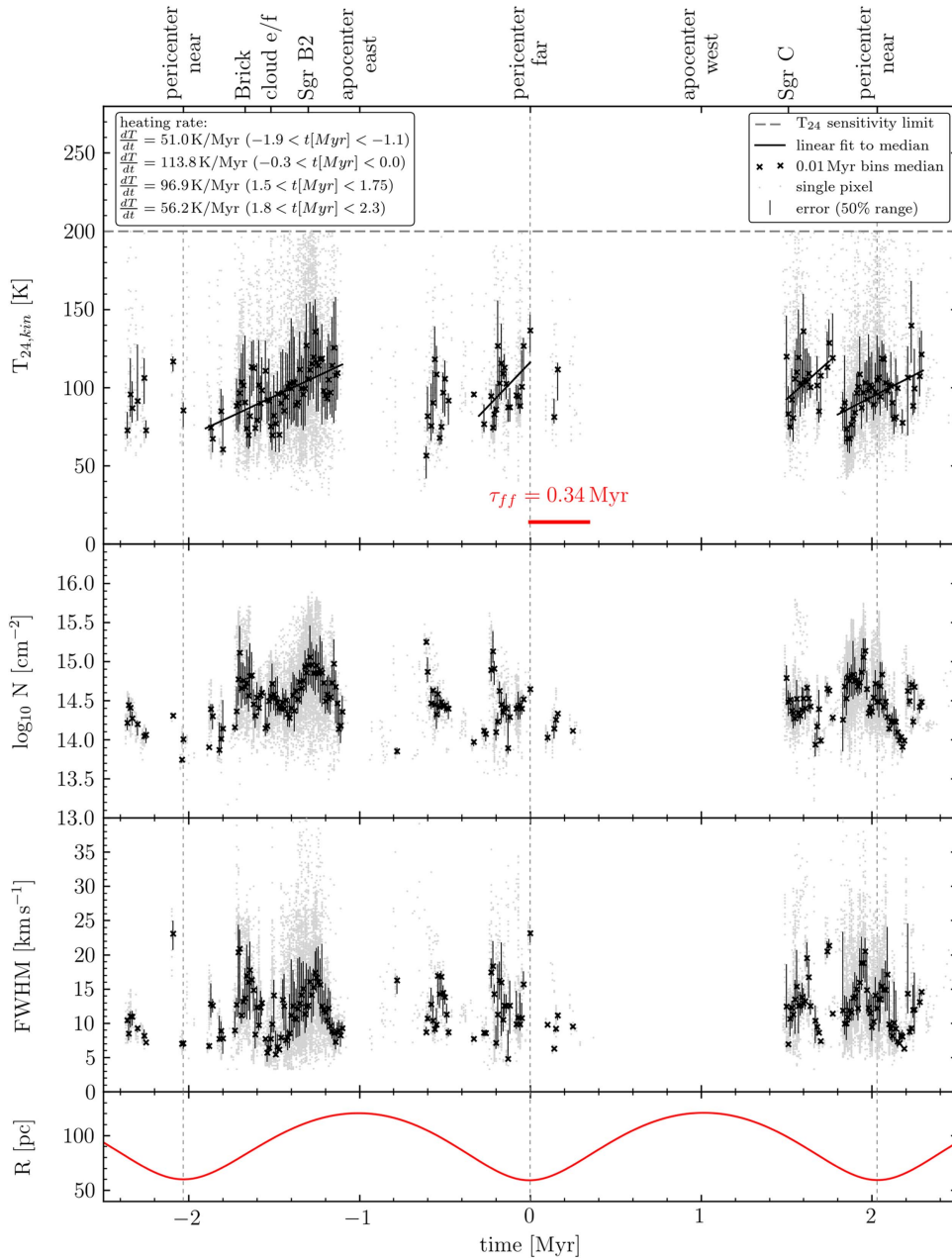
Figure 20. Kinetic ammonia temperature T_{24} (top), NH$_3$ (3, 3) column density (middle top), and NH$_3$ (3, 3) line width (middle bottom) as a function of time since far-side pericenter passage (bottom x-axis; top x-axis shows important dynamical points in the K15 model and massive molecular clouds). The bottom panel shows the radial distance from the center of the Galactic potential. Measurements for individual pixels (light gray points) are overlaid with black crosses denoting medians in bins of 0.01 Myr and error intervals that include 50% of the data in each bin. Linear fits to the median temperature and corresponding heating rates are shown for four regions of consistent time evolution.

temperature measures and ammonia lines can be found in Appendix G. The origin of the timescale in plots versus time is chosen to match K15 and as such identifies 0.0 Myr (± 2.03 Myr) with far (near) side pericenter passages, respectively (as labeled in Figure 19).

Although ammonia hyperfine structure fits were derived at the projections of all four stream segments, several time ranges are not well sampled. Especially, $0.3 \lesssim t\,[\mathrm{Myr}] \lesssim 1.5$ is not covered. This time range corresponds to stream segment 4, where little gas is found because of the large-scale $1^+/1^-$ asymmetry of the CMZ. The time ranges most interesting to this study, the dust ridge and around the pericenter passages at 0 Myr and +2 Myr, are well sampled.

The potential evolution can be fit in up to four regions of significant data density: in the dust ridge, $-1.90 < t\,[\mathrm{Myr}] < -1.1$, at the far-side pericenter passage, $-0.30 < t\,[\mathrm{Myr}] < 0.05$, at the near-side pericenter passage, at $1.75 < t\,[\mathrm{Myr}] < 2.25$, and in clouds near Sgr C, $1.50 < t\,[\mathrm{Myr}] < 1.75$.

5.2.1. Gas Temperature

The top panel of Figure 20 shows the kinetic ammonia temperature T_{24} as a function of time. Median kinetic temperatures of $\sim$55 K to $\sim$135 K are detected with typical error margins of $[-11\,\mathrm{K}, +15\,\mathrm{K}]$. Four sequences of consistently increasing temperature are found in the time intervals $[-1.9\,\mathrm{Myr},$

16

Table 2
Ammonia Kinetic Temperature Gradients (Heating Rates) of the Four Recovered Temporal Sequences (Figure 20)
and of the Orbital Phase without and with Adjusting the Zero-point (Figure 21)

Time Range	$\frac{T_{24}}{dt}$ [K Myr^{-1}]	$\frac{T_{45}}{dt}$ [K Myr^{-1}]	$\frac{T_{36}}{dt}$ [K Myr^{-1}]	Mean [K Myr^{-1}]
$-1.90 < t$ [Myr] < -1.10 (dust ridge)	51.0	47.1	57.9	52.0
$-0.30 < t$ [Myr] < 0.00 (pericenter far)	113.8	77.3	67.7	86.3
$1.50 < t$ [Myr] < 1.75 (Sgr C)	96.9	122.8	84.8	101.5
$1.80 < t$ [Myr] < 2.30 (pericenter near)	56.0	57.2	41.6	51.6
combined (phase)	14.6	14.6	17.7	15.6
combined (phase, adjusted)	47.7	58.4	46.3	50.8

Note. Errors are ∼100% for individual heating rates and ∼58% for the mean.

−1.1 Myr], [−0.3 Myr, 0.05 Myr], [1.5 Myr, 1.8 Myr], and [1.8 Myr, 2.3 Myr]. Positive linear temperature gradients of 51 and 56 K Myr^{-1} are derived in the dust ridge and around the near-side pericenter, whereas steeper gradients of 114 K Myr^{-1} at pericenter far and 97 K Myr^{-1} at pericenter near are fitted. Owing to the short sampled time range and the few temperature measurements, the sequence at pericenter far must be taken with caution. The error intervals are large because of the chosen conservative error estimation (Section 5.2), which causes the heating rate errors derived from χ^2-fitting to also show a substantial error of typically ∼100%, which is likely over-estimated given the consistent trend. The mean heating rate of the three individual measurements (T_{24}, T_{45}, T_{36}) thus has a relative error of approximately 58%.

In the dust ridge (Brick to Sgr B2, $−1.9 < t$ [Myr] $< −1.1$), the covered time range (0.8 Myr) and statistics (∼9200 measurements) yield reliable heating rates of 47.1 K Myr^{-1} to 57.9 K Myr^{-1} (mean of 52.0 K Myr^{-1}) in the three partly independent temperature measures T_{24}, T_{45}, and T_{36} (Table. 2). The absolute increase is from 75 K to 110 K (T_{24}), 60 K to 105 K (T_{45}), and 60 K to 100 K (T_{36}) or ∼40 K on average.

The short sequence at the far-side pericenter passage ($−0.30 < t$ [Myr] < 0.00) is affected by low number statistics and has heating rate errors larger than 100%. Any conclusion for this time range should thus be treated merely as a qualitative but not as a quantitative result.

Between the western apocenter of the orbit and the pericenter on the near side, two independent sequences of increasing temperature are found, separated by a discontinuity at 1.8 Myr, where the median temperature sharply drops from ∼120 K to ∼85 K. This is again seen at a very similar level in T_{24}, T_{45} and T_{36}. Heating rates differ between the sequence at Sgr C and pericenter, the former being consistently higher at ∼102 K Myr^{-1} than the latter (∼52 K Myr^{-1}, mean heating rates).

An overview of derived heating rates in the four sequences is given in Table 2.

5.2.2. Column Density

The median column densities show no evidence of time dependence (Figure 20, middle top, Appendix G) in the dust ridge. No consistent trend is apparent as column densities increase strongly in the Brick and Sgr B2 above a flat or, at most, very weakly rising base level. These clouds are already known to be denser than other dust ridge clouds and thus are expected to be more massive outliers to any potential underlying relation (Lis & Carlstrom 1994; Lis et al. 1994; Molinari et al. 2011; Longmore et al. 2012; Pillai et al. 2015). Given that the column densities in between the Brick and Sgr B2 show no rise and also drop to the same level after Sgr B2, we conclude that there is no evolutionary column density sequence in the dust ridge.

The clouds around near-side pericenter passage show weak evidence for decreasing column densities where the median column density drops for $J = 1, 2, 3$ but can be considered constant within the scatter for $J = 4, 5$, and 6. This relation is likely also influenced by two individual objects, the 20 km s^{-1} and 50 km s^{-1} clouds, although density bumps are not as prominent as in Sgr B2.

At far-side pericenter, medians scatter by up to ∼1 dex and no conclusion can be drawn. The column densities in the Sgr C region are constant for all six ammonia tracers, with very low scatter compared to the rest of the covered time ranges.

Qualitatively and quantitatively very similar results are derived for opacity due to the correlation of opacity and column density, and this is hence not discussed further.

5.2.3. Line Width

The evolution of the median line width (FWHM) is similar to that of the column density, but shows an even less consistent behavior, as can be seen in Figure 20 (middle bottom) for NH$_3$ (3, 3) ($J = 1, ..., 6$ in Appendix G). In the dust ridge, line widths vary by a factor of ∼2.5 with peaks in the Brick and Sgr B2. There is no sign that these could be just outliers to an underlying trend as line widths are at similar levels of 6–10 km s^{-1} before the Brick, in between Brick and Sgr B2, and after Sgr B2. Any potential time dependency of the line width thus cannot be stronger than a few km s^{-1} Myr^{-1} to be hidden within the observed scatter. Results are very similar for the other ammonia lines ($J = 1, 2, 4, 5, 6$) at slightly varying absolute level, as could already be seen in the line width histogram (Figure 13).

In the other time ranges that show temperature evolution, no sign of consistent line width trend can be found. As for column density, the 20 and 50 km s^{-1} clouds are weak outliers toward higher values.

The increase in line width at the position of large and massive clouds can be caused by scaling relations ("Larson
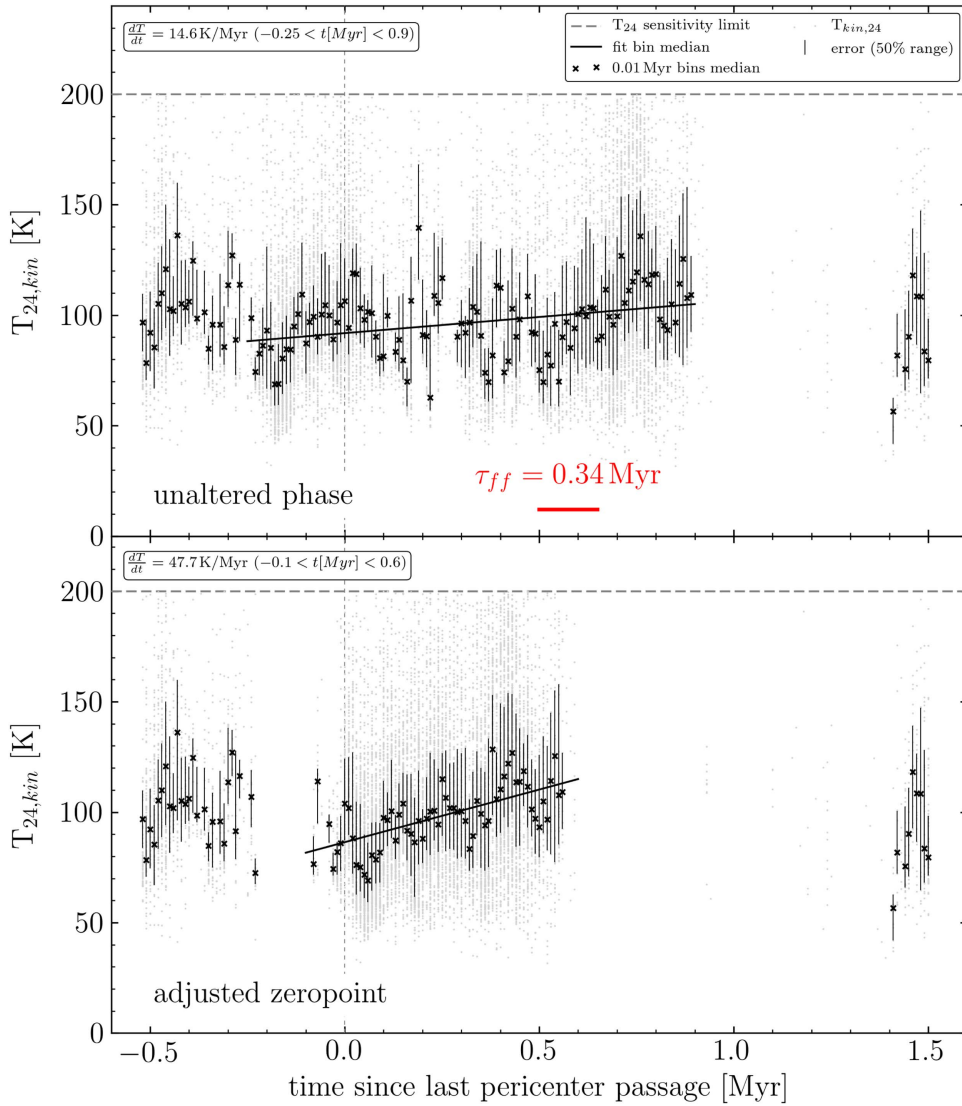
Figure 21. Kinetic ammonia temperature T_{24} as a function of time since the last occurrence of pericenter passage (orbital phase). Symbols and error bars are the same as in Figure 20. The top panel shows the unaltered data as in Figure 20 (top panel), whereas in the bottom panel, the zero-point of the sequences in the dust ridge, pericenter near, and pericenter far are adjusted to maximize the heating rate. Within a range of reasonable offsets in zero-point of ±0.3 Myr, the best fit is achieved for -0.3 Myr (dust ridge), $+0.2$ Myr (pericenter near), and $+0.2$ Myr (pericenter far). The fitted time ranges of -0.25 Myr to $+0.9$ Myr and -0.1 Myr to 0.6 Myr result from the sum of the fits in the time domain.

laws," Larson 1981), be an effect of hyperfine structure fitting, or an effect of projection. CMZ clouds are known to follow a steep scaling relation of line width σ with cloud radius R: $\sigma \propto R^{0.6-0.7}$ (Shetty et al. 2012; Kruijssen & Longmore 2013; Kauffmann et al. 2017b), and thus line widths are expected to increase by a factor of ~1.5 between the small clouds b/c and larger clouds like the Brick and cloud e/f (Immer et al. 2012). The observed variation in line width of a factor ~2.5 is thus only partly due to variations in cloud size and other sources of scatter must be present, such as unresolved blending of multiple emission components along the line of sight, as shown in Figure 36(d)). Spectra with two close components with separations of a few to a few tens of $\mathrm{km\,s^{-1}}$ are more likely to be present in larger clouds and thus cause the same signature as the scaling relation does, increasing the overall scatter. Projection effects may also increase the apparent line width through pile-up along the line of sight at the tangent points of the orbit. This can play a role in Sgr B2, but is not expected to affect the other clouds (cf. Figure 19).

5.3. Discussion in the Context of the Stream Model and Tidal Triggering

As shown above, sequences of increasing temperature are found, but no such sign is recovered for line width and column density. At near-side pericenter passage, an anticorrelation of increasing temperature and potentially decreasing column density is found, whereas the positive-temperature gradients in the dust ridge at far-side pericenter and around Sgr C do not have a detectable counterpart in column density or line width. Based on the concept of tidally triggered SF (Longmore et al. 2013b), we discuss the evolution at and after pericenter passage separately in Sections 5.3.1 and 5.3.2. By the time-tagging method used in this work, the interpretation is furthermore linked to the stream model of K15, but general conclusions can be transferred to other orbital models. If a model includes radial oscillation, it can trigger cloud collapse and may give rise to a sequence of star formation. If the clouds were on circular orbits, our time-tagging method would still result in accurate
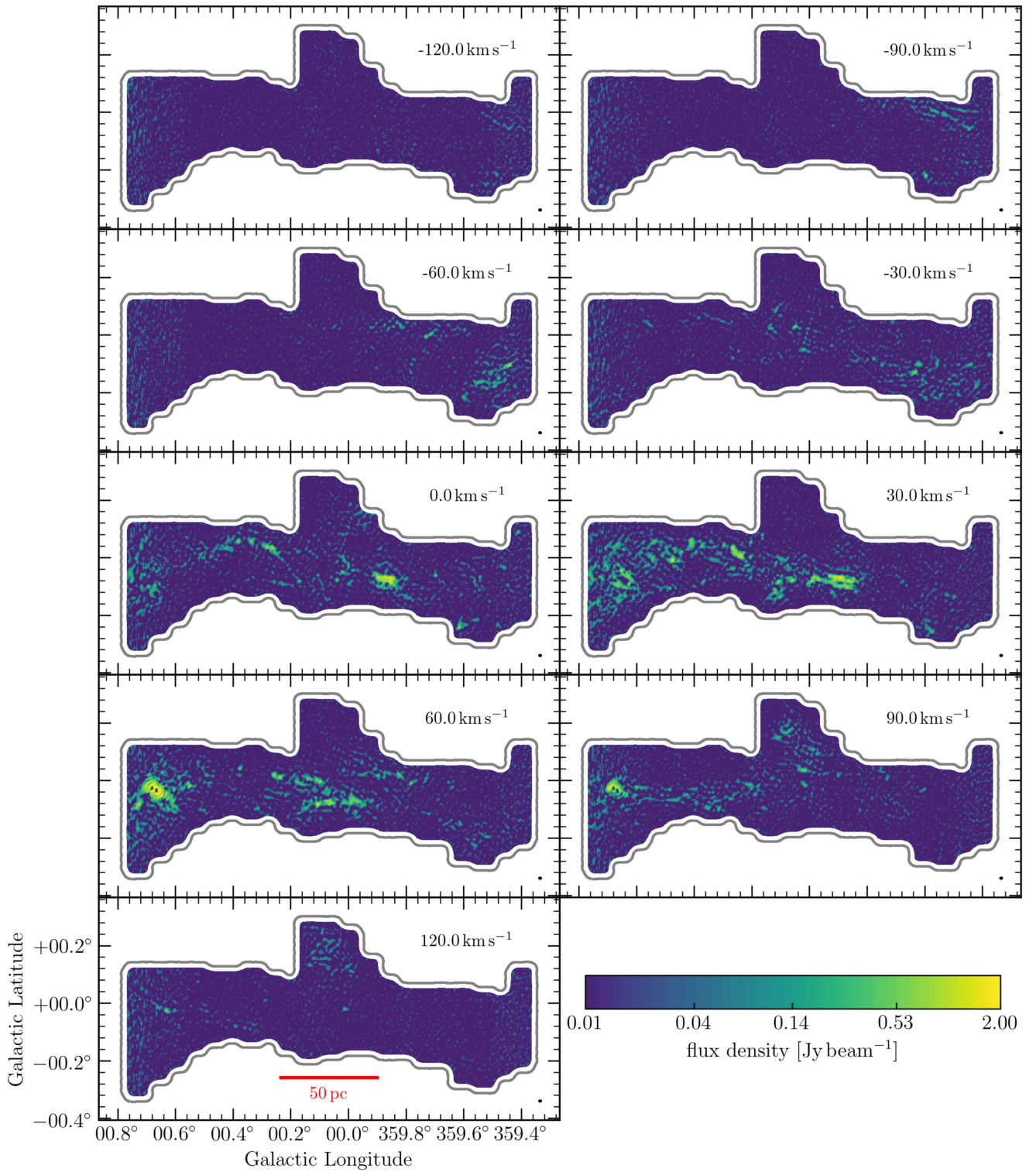
Figure 22. Channel maps of NH$_3$ (1, 1). Every fifteenth channel of 2 km s^{-1} (separated by 30 km s^{-1}) in the range of -120 km s^{-1} to $+120$ km s^{-1} is shown. Velocity and beam area ($26''22 \times 17''84$, $89°3$) are indicated in the top and bottom left corners, respectively. The conversion factor from flux density in Jy beam^{-1} to brightness temperature in K for this beam size at 23.69 GHz is T [K]$/S$ [Jy beam^{-1}] = 4.65.

measurements, which means that the basic conclusions are not sensitive to the orbital model that is used.

5.3.1. Sequences at Pericenter Passage

Qualitatively, increasing temperatures during pericenter passage can occur by converting the gravitational energy

released by cloud compression or collapse into heat through a turbulence cascade if cooling is not efficient enough to keep the cloud at a constant temperature (e.g., Ginsburg et al. 2016). The effect on the line width of such a process is not immediately clear and likely needs detailed simulations. In general, turbulence should increase the observed line width, which would result in a rising sequence of line width following the
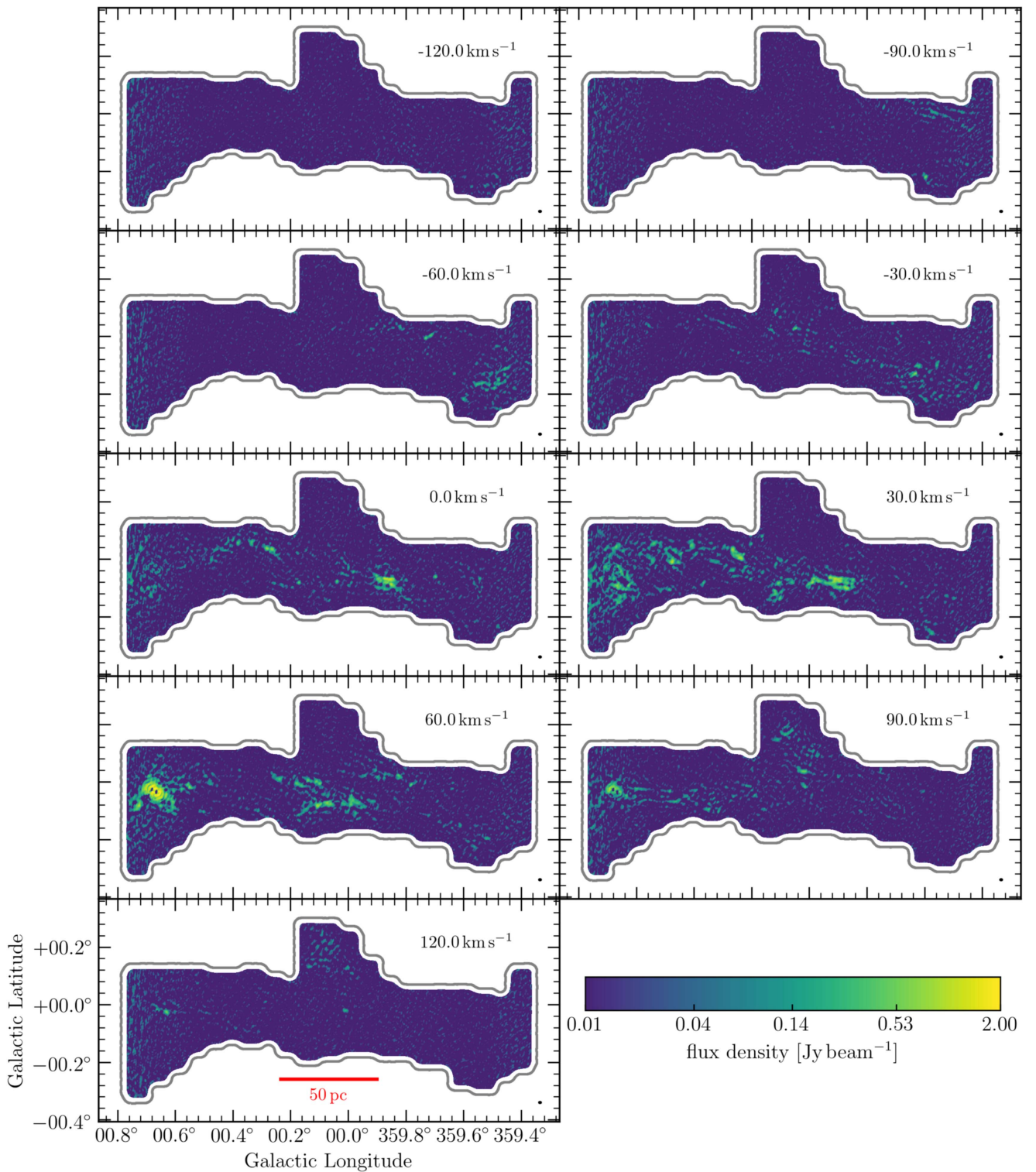
19

Figure 23. Channel maps of NH$_3$ (2, 2). Every fifteenth channel of 2 km s^{-1} (separated by 30 km s^{-1}) in the range of -120 km s^{-1} to $+120$ km s^{-1} is shown. Velocity and beam (26$''$19 $\times$ 17$''$82, 89$°$3) are indicated in the top and bottom left corners, respectively. The conversion factor from flux density in Jy beam^{-1} to brightness temperature in K for this beam size at 23.72 GHz is T [K]$/S$ [Jy beam^{-1}] $= 4.65$.

rise in temperature. However, as the energy makes its way through the cascade to smaller scales R, the dissipation rate $\epsilon \propto \sigma/R$ also increases, allowing for little or even no change in the effective line width σ. If the turbulent line width does increase, it will still be difficult to detect because of variations among clouds (Section 5.2.3).

Radiative cooling generally is an efficient process (e.g., Juvela et al. 2001), and it is not obvious why it could be so inefficient for temperatures to rise by >50 K Myr^{-1}. As shown by Figure 14, a significant fraction of clouds in the CMZ are optically thick for line emission at $\sim$25 GHz, which can trap cooling photons inside clouds and diminish cooling

20

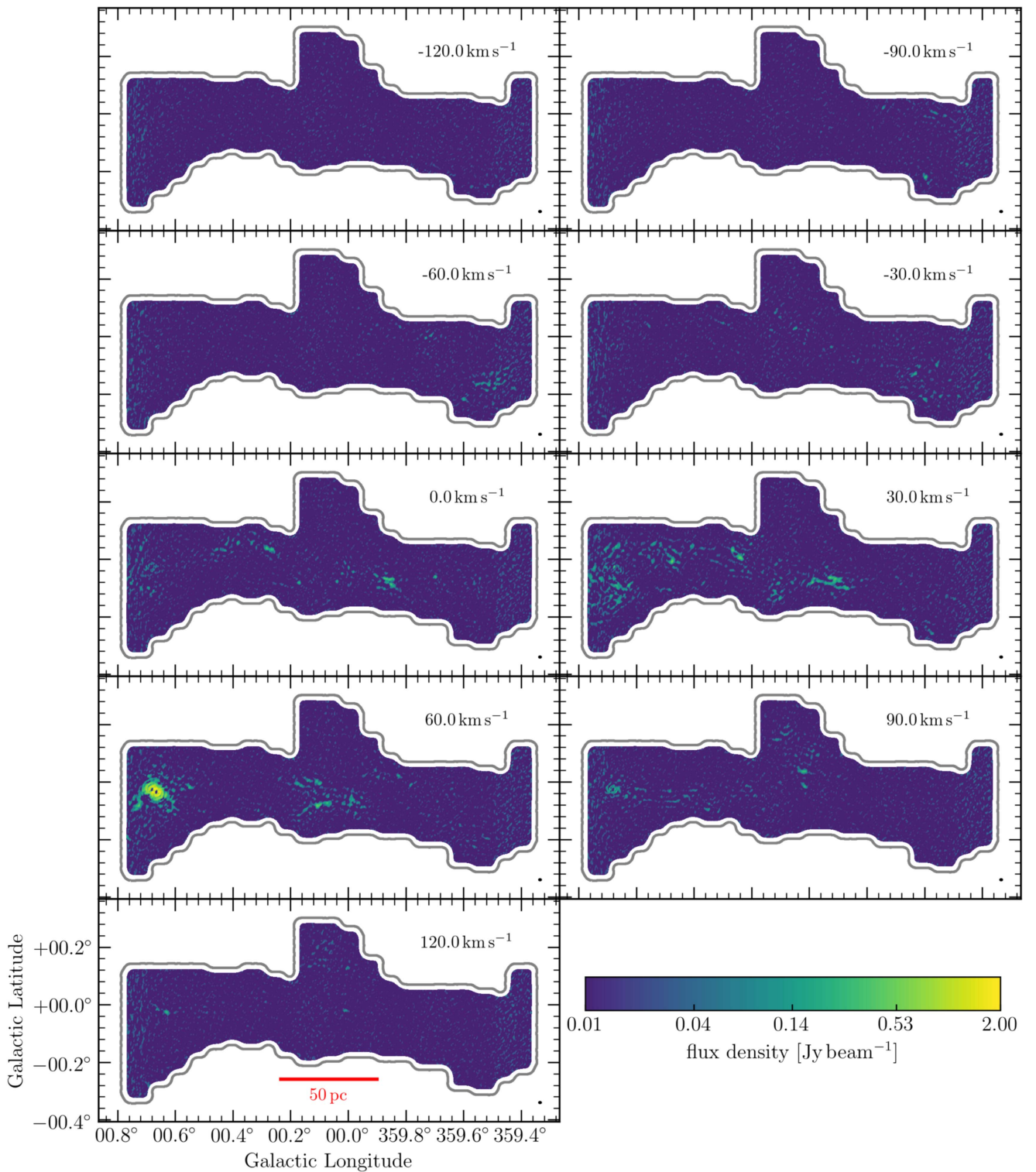**Figure 24.** Channel maps of NH$_3$ (4, 4). Every fifteenth channel of 2 km s^{-1} (separated by 30 km s^{-1}) in the range of -120 km s^{-1} to $+120$ km s^{-1} is shown. Velocity and beam ($25\rlap{.}''74 \times 17\rlap{.}''51$, $89\rlap{.}°3$) are indicated in the top and bottom left corners, respectively. The conversion factor from flux density in Jy beam^{-1} to brightness temperature in K for this beam size at 24.14 GHz is T [K]$/S$ [Jy beam^{-1}] $= 4.65$.

efficiency. Ammonia is not a dominant cooling line, but other lines that are more important for cooling (CO, C$^+$, and, at least in the Brick, neutral oxygen; Clark et al. 2013) can be expected to be even more optically thick than NH$_3$, and the same argument applies. If true, the hint toward decreasing column density might also be an effect of opacity because in

optically thick media, the observed emission originates from an optical depth of $\tau \sim 1$, which is the envelope rather than the core of the cloud. The outer layers of a cloud moving through the pericenter along the stream orbit are sheared and can even become unbound, while the inner cloud is pushed into self-gravity and collapses, as shown observationally by
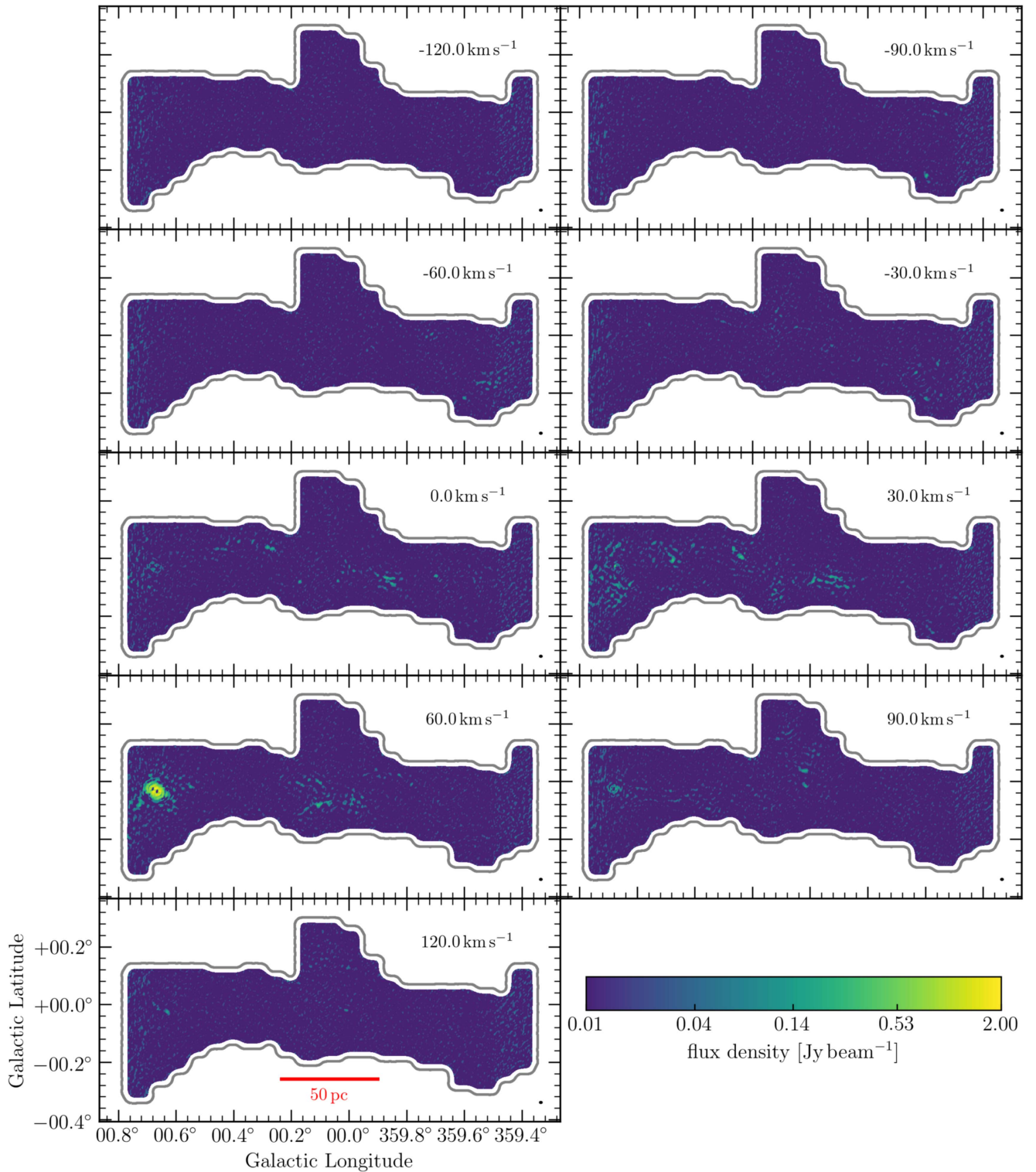
Figure 25. Channel maps of NH_3 (5, 5). Every fifteenth channel of 2 km s^{-1} (separated by 30 km s^{-1}) in the range of -120 km s^{-1} to $+120$ km s^{-1} is shown. Velocity and beam ($25\overset{''}{.}32 \times 17\overset{''}{.}23$, $89\overset{\circ}{.}3$) are indicated in the top and bottom left corners, respectively. The conversion factor from flux density in Jy beam^{-1} to brightness temperature in K for this beam size at 24.53 GHz is T [K]$/S$ [Jy beam^{-1}] = 4.65.

Rathborne et al. (2014a), Federrath et al. (2016), and modeled by Kruijssen (2017) and Kruijssen et al. (2017, in preparation). Hence, a trend of decreasing column density can be observed.

The observed mean heating rates at pericenter passage of ~ 52 and ~ 86.3 K Myr^{-1} are high, but cannot be easily compared to theoretic predictions because the complex interplay of dynamic and hydrodynamic processes requires simulations that include radiative transfer. Without these simulations, it is also not known at which time before pericenter passage tidal effects start to become non-negligible and affect temperature. The same applies to the time after pericenter passage, when compression and shear
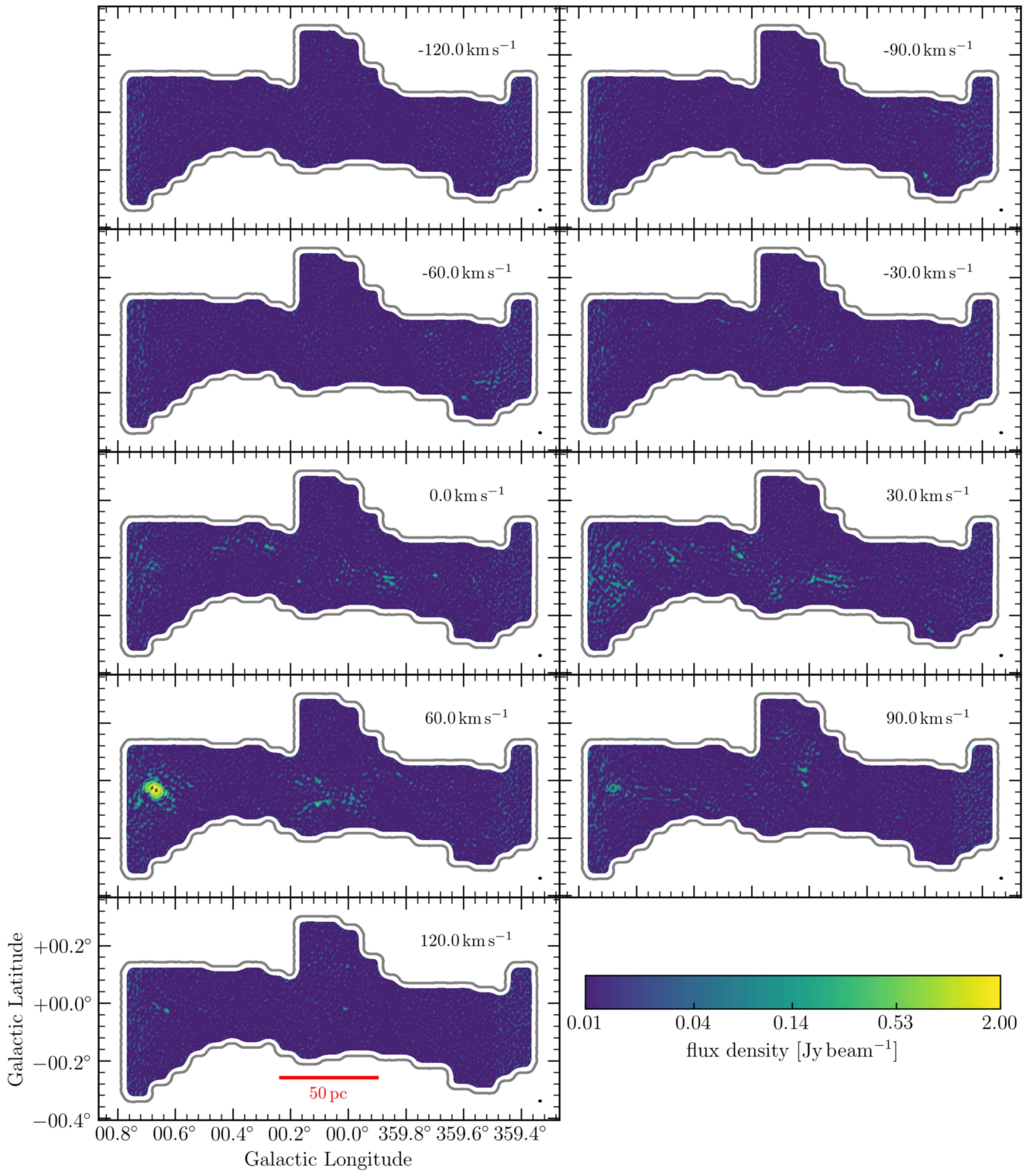
Figure 26. Channel maps of NH$_3$ (6, 6). Every fifteenth channel of 2 km s^{-1} (separated by 30 km s^{-1}) in the range of -120 km s^{-1} to $+120$ km s^{-1} is shown. Velocity and beam ($24\rlap{.}''80 \times 16\rlap{.}''87$, $89\rlap{.}°3$) are indicated in the top and bottom left corners, respectively. The conversion factor from flux density in Jy beam^{-1} to brightness temperature in K for this beam size at 25.06 GHz is T [K] $/S$ [Jy beam^{-1}] $= 4.65$.

are reduced, which could in principle also lead to cooling, but this is not observed. Detailed simulations can be expected in the near future as the general feasibility was already demonstrated (Clark et al. 2013; Kruijssen 2017). Without simulations, we can estimate the time range of strong tidal influence on the clouds from Figure 20. The indication of increasing temperature in

Figure 20 suggests that a temperature change is detectable *at least* 0.25 Myr before reaching pericenter. A change in temperature might occur earlier than 0.25 Myr before pericenter passage, but unfortunately, our data do not cover that time range, therefore we cannot check if temperatures are flat before heating sets in. At 0 Myr and 2 Myr, the deepest point in the potential is
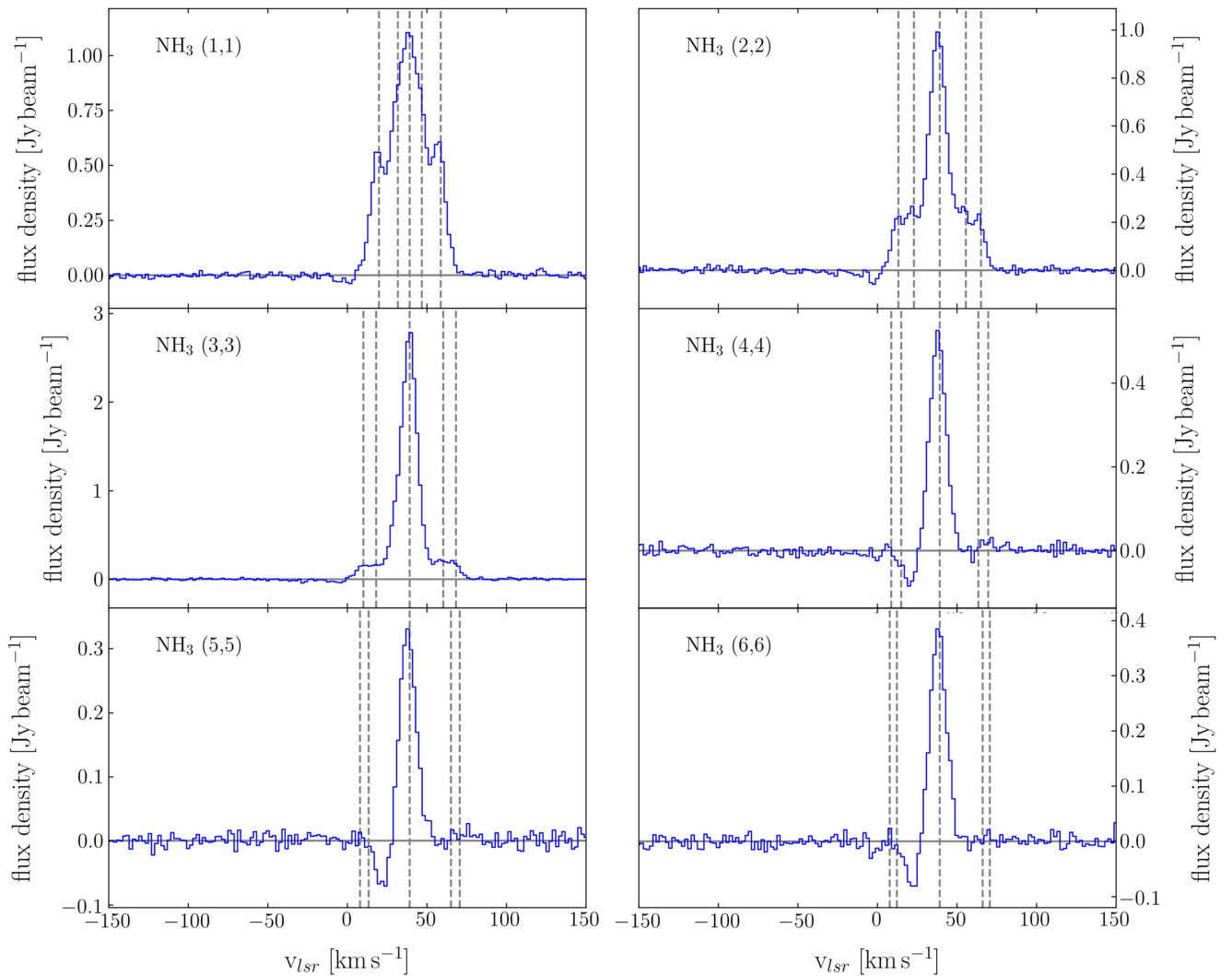
Figure 27. Example spectra with independent scaling of the *y*-axis toward the Brick extracted from the NH_3 (1, 1) to (6,6) data cubes. The rms noise is 0.062 K, 0.061 K, 0.061 K, 0.060 K, 0.056 K, and 0.061 K, respectively. The positions of the hyperfine satellites according to Table 3 are indicated by dashed vertical lines. Note the complex structure of broad line widths blending hyperfine components and an absorption component at $\sim$20 km $^{-1}$ in the higher lines.

reached at $R_{peri} \sim 59$ pc, while 0.25 Myr corresponds to $R \sim 1.22~R_{peri} = 72$ pc. Apocenter is reached at $R \sim 120$ pc, so tidal effects becoming relevant at $\sim$75–80 pc from the center of the potential is plausible. In the spherically symmetric enclosed mass distribution in the GC (Launhardt et al. 2002), the gravitational potential at $\lesssim 0.25$ Myr before reaching pericenter[29] is symmetric to the respective range after pericenter, i.e., tidal effects are expected to play a role until at least 0.25 Myr after pericenter passage. After pericenter passage, some processes reverse, i.e., tidal pressure is released, which can allow cooling, but cloud collapse is ongoing and early star formation may set in. This complex interplay of physical processes makes it very difficult to define an end point of the strong tidal influence from the observational data. Generally, observations show that the temperatures are consistent with turbulent energy dissipation (Ginsburg et al. 2016), as would be expected from triggered cloud collapse.

5.3.2. Sequences after Pericenter Passage

This observed sequence in the dust ridge starts about one free-fall time $\tau_{ff} = 0.34$ Myr after pericenter passage, whereas the other sequences start before. This means that if cloud collapse was triggered, a cloud core collapses, whereas previously sheared but still bound gas is reaccreted. As the collapse of outer cloud layers proceeds, the release of gravitational energy declines, which implies flattening temperature gradients. However, no obvious decrease in heating rate is found in the dust ridge, meaning that cloud collapse is still ongoing at a similar intensity as at pericenter passage, or alternatively, that a second heating source starts to contribute. In the framework of triggered SF, star formation could be a second source of heating. As an estimate, star formation can set in as early as one free-fall time after the cloud itself started to collapse, which is 0.34 Myr for a typical CMZ cloud, and this coincides with the time since the Brick passed pericenter (K15). Accordingly, early signs of embedded star formation have been found in one region of the Brick (Longmore et al. 2012; Johnston et al. 2014; Rathborne et al. 2014a), i.e., heating by star formation is just about to set in.
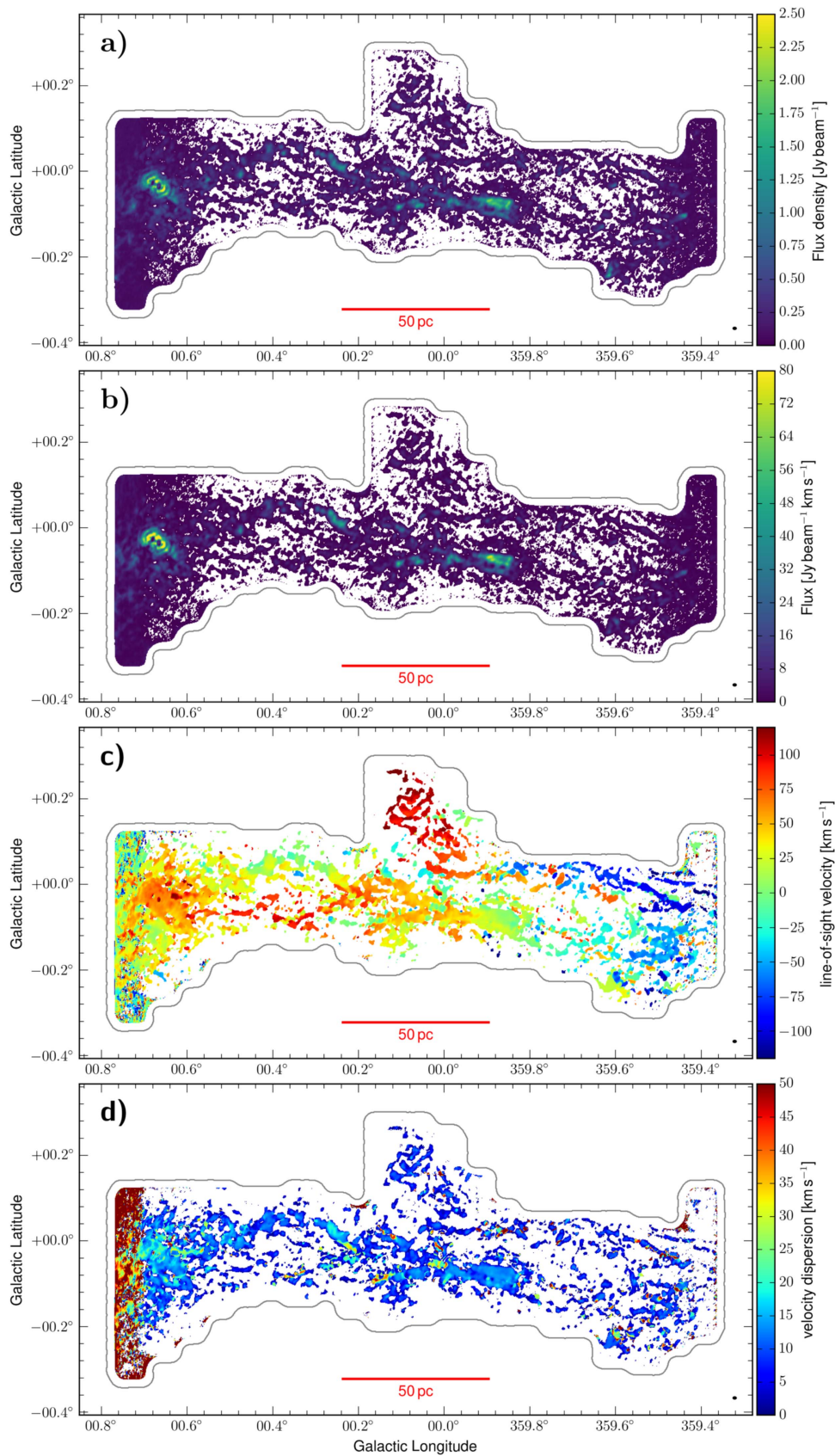
---

[29] Or $\sim$50 pc before reaching pericenter at $\sim$200 km s^{-1} orbital velocity, which is appropriate near pericenter; see Kruijssen et al. (2015).

Figure 28. NH$_3$ (1, 1) moment maps: (a) peak intensity, (b) integrated intensity (moment 0), (c) intensity-weighted mean velocity (moment 1), and (d) intensity-weighted velocity dispersion (moment 2). The intensity maps (a) and (b) are masked at 3σ, velocity maps (c) and (d) are masked at 5σ with an rms noise of $\sigma = 13.4$ mJy. The beam of $26\overset{''}{.}2 \times 17\overset{''}{.}8$ (1.06 pc $\times$ 0.72 pc) is indicated in the lower right corner of each panel.
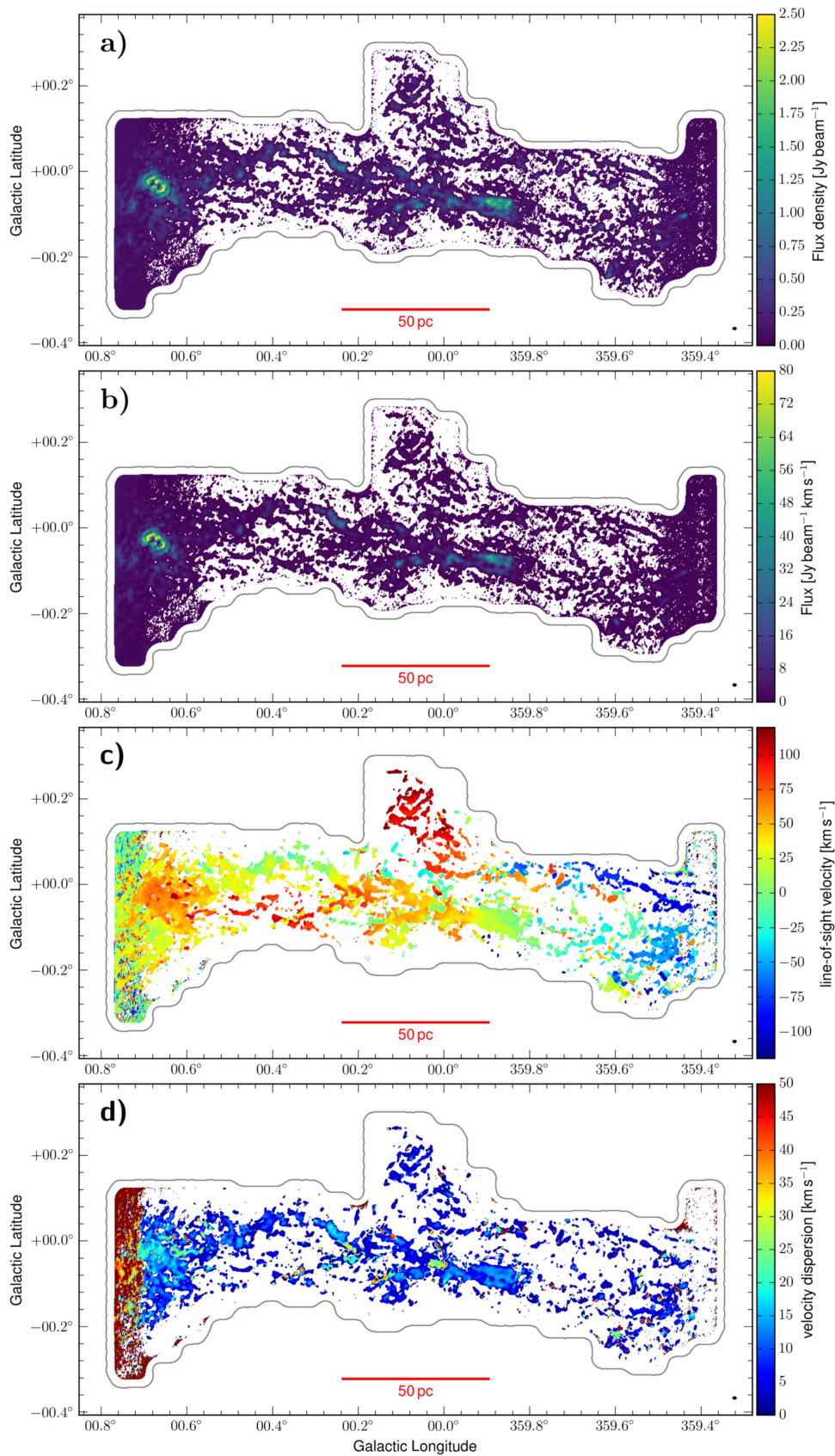
Figure 29. NH$_3$ (2, 2) moment maps: (a) peak intensity, (b) integrated intensity (moment 0), (c) intensity-weighted mean velocity (moment 1), and (d) intensity-weighted velocity dispersion (moment 2). The intensity maps (a) and (b) are masked at 3σ, velocity maps (c) and (d) are masked at 5σ with an rms noise of $\sigma = 13.1$ mJy. The beam of 26.2 $\times$ 17$\overset{''}{.}$8 (1.05 pc $\times$ 0.72 pc) is indicated in the lower right corner of each panel.
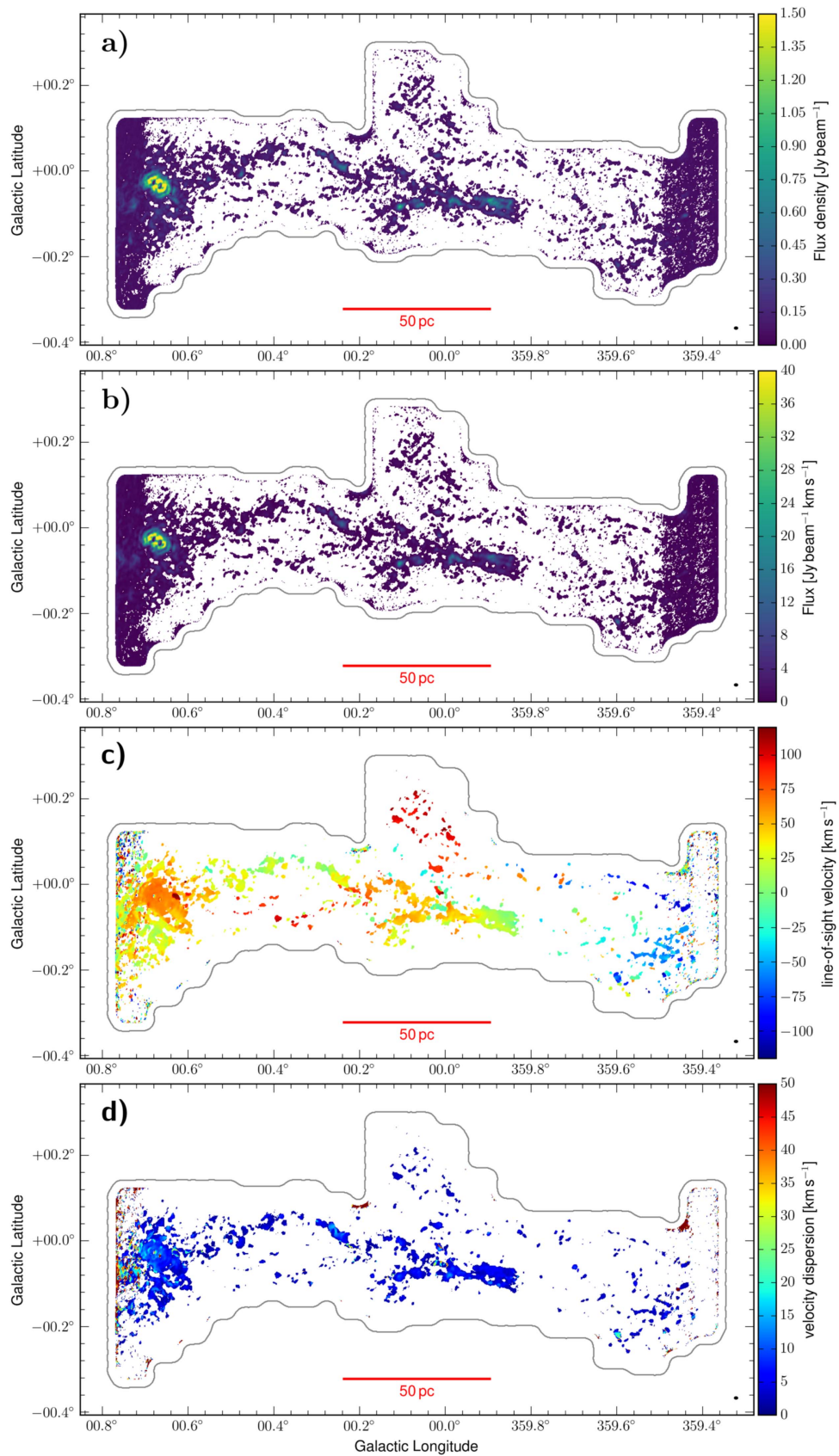
Figure 30. NH$_3$ (4, 4) moment maps: (a) peak intensity, (b) integrated intensity (moment 0), (c) intensity-weighted mean velocity (moment 1), and (d) intensity-weighted velocity dispersion (moment 2). The intensity maps (a) and (b) are masked at 3σ, velocity maps (c) and (d) are masked at 5σ with an rms noise of $\sigma = 12.9$ mJy. The beam of $25\farcs7 \times 17\farcs5$ (1.04 pc $\times$ 0.70 pc) is indicated in the lower right corner of each panel.
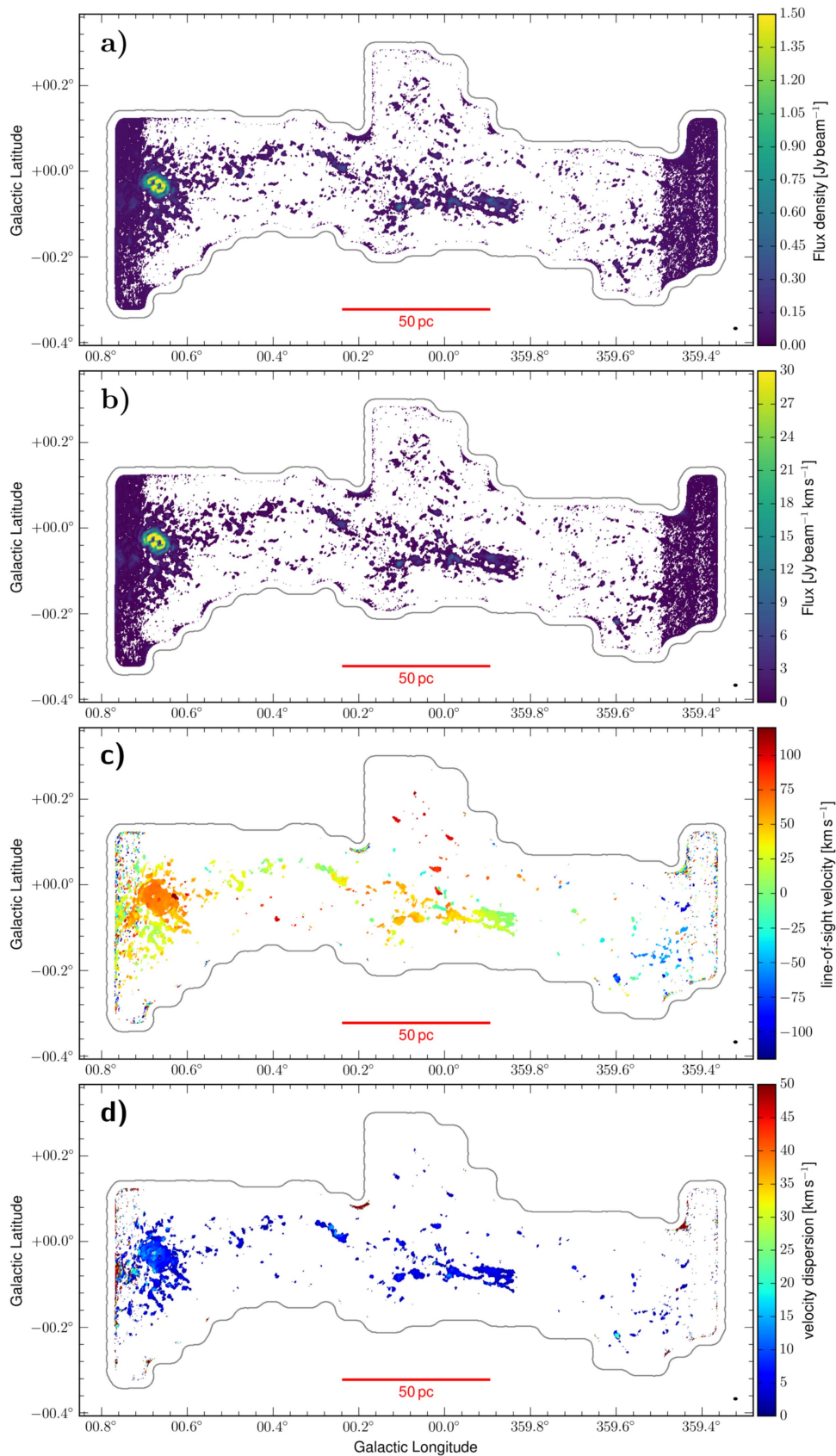
Figure 31. NH$_3$ (5, 5) moment maps: (a) peak intensity, (b) integrated intensity (moment 0), (c) intensity-weighted mean velocity (moment 1), and (d) intensity-weighted velocity dispersion (moment 2). The intensity maps (a) and (b) are masked at 3σ, velocity maps (c) and (d) are masked at 5σ with an rms noise of $\sigma = 12.0$ mJy. The beam of $25\rlap{.}{''}3 \times 17\rlap{.}{''}2$ (1.02 pc × 0.69 pc) is indicated in the lower right corner of each panel.
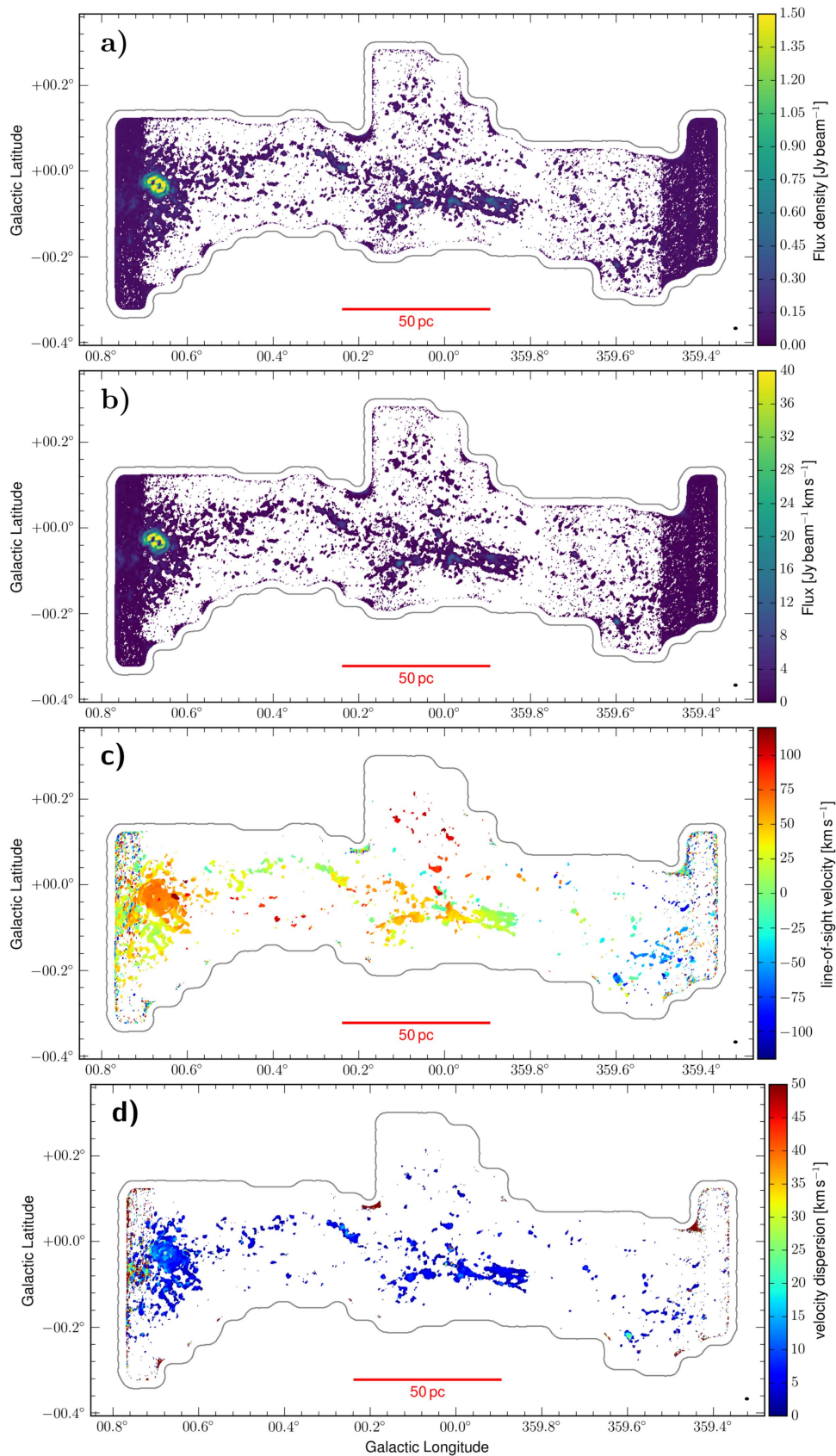
Figure 32. NH$_3$ (6, 6) moment maps: (a) peak intensity, (b) integrated intensity (moment 0), (c) intensity-weighted mean velocity (moment 1), and (d) intensity-weighted velocity dispersion (moment 2). The intensity maps (a) and (b) are masked at 3σ, velocity maps (c) and (d) are masked at 5σ with an rms noise of $\sigma = 13.2$ mJy. The beam of $24\rlap{.}''8 \times 16\rlap{.}''9$ (1.00 pc $\times$ 0.68 pc) is indicated in the lower right corner of each panel.

These effects increase the temperature if the gas cannot cool efficiently enough, which apparently is the case as gas temperatures are known to be significantly offset from dust temperatures (Figure 17 and e.g., Güsten et al. 1981; Molinari et al. 2011; Ginsburg et al. 2016). Therefore, the increase in temperature cannot simply be attributed to a single of these processes, but to a combination at varying relative strengths, which is not known at the moment for GC conditions and cannot be inferred from our observations. In order to disentangle the contribution of star formation from the kinematic and gravitational effects, a complex hydrodynamic gas simulation including star formation feedback is needed.

Collapsing clouds are expected to show a signature of increasing column density that is not observed, which might be a consequence of shearing outer cloud layers during pericenter passage. It might also be an observational effect of too low resolution to trace the collapse. Collapse occurs quickest on the highest density, lowest virial ratio scales. It is known in the literature that the column density profiles of the Brick and bricklet clouds are centrally concentrated and that the volume density of the Brick increases toward the center (Walker et al. 2015; Rathborne et al. 2016). The collapse will therefore occur quickest at the center, on scales smaller than the SWAG beam, which will wash out potential small-scale effects. In higher resolution observations, Walker et al. (2015) found evidence for increasing gas and (proto-) stellar density along the stream orbit from the Brick to Sgr B2.

As discussed in Section 5.2.1, the sequence of increasing temperature around Sgr C is likely not connected to the sequence at near-side pericenter because of the sharp discontinuity and differing heating rate. The observation of 24 μm emission in this region and the higher temperature compared to the pericenter sequence suggest that these clouds already underwent tidal triggering of collapse at far-side pericenter (see also Kruijssen et al. (2015) regarding the position of Sgr C). This places Sgr C as a successor to the dust ridge sequence in terms of evolution, but not in time. Finding no column density trend in Sgr C matches the picture, as this cloud is supposedly collapsed already and is actively forming stars (Kendrew et al. 2013; Lu et al. 2017), which powers the rise in temperature.

5.3.3. Connection of Sequences at and after Pericenter Passage

According to the K15 model, the empirically found sequences are directly associated in the sense that the phase dominated by star formation (dust ridge and Sgr C) follows the phase dominated by tidal compression (near and far pericenter passage). The orbital phase, however, cannot be the only parameter controlling the physical state of gas along the stream, as discussed in Section 5.2.1. It seems likely that the clouds at and after pericenter passage are similar but not identical in properties, i.e., all clouds may follow the same evolution, but the gas in the dust ridge was initially cooler or could cool more efficiently when cloud collapse was triggered. The offset in temperature that is required to match the sequences is small ($\sim$15–20 K) compared to the observed heating rates ($\sim$52 K Myr^{-1}). As we do not know the initial cloud properties, this remains speculation, and we can only state that the observed sequences can be the result of tidally triggered collapse assuming a scatter of initial cloud temperature of $\sim$20 K. On this note, it should be kept in mind that individual cloud properties as well as collapse triggering are statistically distributed and are not identical for subsequent occurrences.

Table 3
Ammonia Hyperfine Components as Calculated from Tabulated Data in Townes & Schawlow (1975) and splatalogue.net

| Line | Component | |
	−2	−1	0	1	2	
NH$_3$ (1, 1)	−19.48	−7.46	0	7.59	19.61	[km s^{-1}]
	0.111	0.139	0.500	0.139	0.111	
NH$_3$ (2, 2)	−25.91	−16.30	0	16.43	26.03	[km s^{-1}]
	0.052	0.054	0.789	0.054	0.052	
NH$_3$ (3, 3)	−29.14	−21.10	0	21.10	29.14	[km s^{-1}]
	0.027	0.029	0.888	0.029	0.027	
NH$_3$ (4, 4)	−30.43	−24.22	0	24.22	30.43	[km s^{-1}]
	0.016	0.016	0.935	0.016	0.016	
NH$_3$ (5, 5)	−31.41	−25.91	0	25.91	31.41	[km s^{-1}]
	0.011	0.011	0.956	0.011	0.011	
NH$_3$ (6, 6)	−31.47	−26.92	0	26.92	31.47	[km s^{-1}]
	0.008	0.008	0.969	0.008	0.008	

Note. For each ammonia species, the top row lists spectral offset in km s^{-1}, the bottom row shows the fractional line strength.

Estimates for the variation of physical parameters from cloud to cloud can be drawn from the analysis of velocity corrugations in the $[l^-, b^-]$ segment of the stream, which is expected to be a precursor to the dust ridge (Henshaw et al. 2016a). For this analysis, Kruijssen (2017) report standard deviations of initial cloud parameters of 0.19 dex (mass), 0.09 dex (radius), 0.16 dex (density), and 0.08 dex (free-fall timescale) among the potential precursors to the dust ridge only. The standard deviations would naturally be larger when the progenitors to the other temperature sequences identified in this paper were also included. If the variations of initial cloud temperature are at a similar level as these properties, the expected temperature scatter is $\gtrsim$20 K, larger than the observed offsets of 15–20 K. These numbers show that the observed temperature sequences at and after pericenter passage may be causally related as the temperature deviation is within the expected scatter.

5.3.4. Orbital Phase and Variation of the Trigger Point

The periodic occurrence of pericenter passages every $\sim$2.0 Myr suggests that temperatures can also be plotted against orbital phase, which is shown in Figure 21 (top panel). Although four temperature sequences could be defined as a function of absolute time, no global sequence is found. Only the time range 0.5 to 0.9 Myr shows a consistent trend of rising temperatures as the data in this region originate almost exclusively from the dust ridge. The other sequences are lost because differing temperature levels are superposed, which also smears the discontinuity at $t_{peri} = 1.75$ Myr that occurs at a phase of $t_{last} = -0.25$ Myr. However, fitting a linear relation in the time range -0.25 to 0.90 Myr (sum of the four ranges identified in Section 5.2) still results in a positive heating rate of 14.6 K Myr^{-1}. Almost identical results are obtained for T_{45} and T_{36} with relative errors of $\sim$100%, as listed in Table 2. These results are in line with Kauffmann et al. (2017b), who find a trend in density gradients of six CMZ clouds, but no clear trend in star formation activity per unit dense gas as a function of orbital phase.
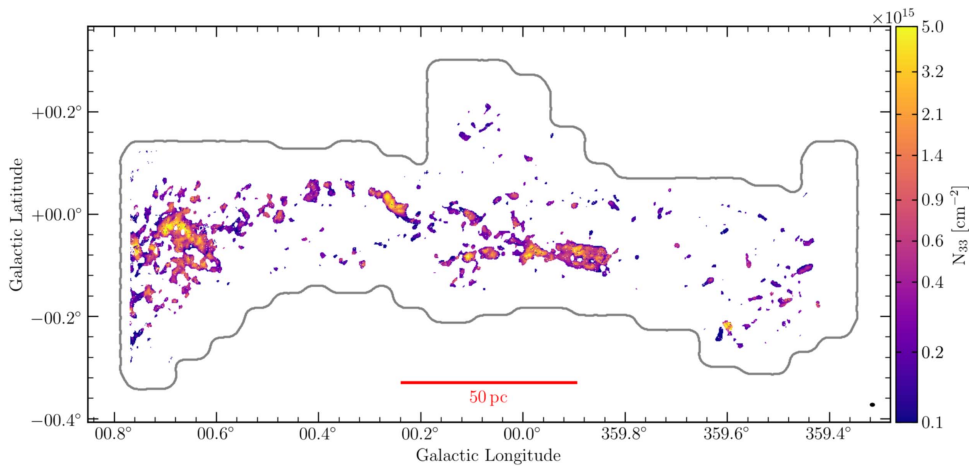
Figure 33. NH$_3$ (3, 3) column density N_l under consideration of non-zero opacity as derived by Equation (18) from fitting the hyperfine structure.

The signature of rising temperature could be expected to become stronger by transforming into orbital phase if the four sequences are samples of a single consistent evolution. However, it is highly unlikely that all clouds are triggered to collapse exactly at pericenter, this is expected to occur rather within some time range around pericenter. By allowing the zero-point t_{start} of each sequence to vary by up to ± 0.3 Myr, the sequential behavior can be recovered (Figure 21 bottom panel). The heating rate is maximized at a value of ~ 48 K Myr^{-1} for zero-points of $t_{start} = -0.3$ Myr (dust ridge), $t_{start} = +0.2$ Myr (pericenter near) and $t_{start} = +0.2$ Myr (pericenter far). At 0.3 Myr before or after pericenter, the radial distance from the bottom of the GC potential is $R = 77$ pc ($R = 60$ pc at pericenter), and thus the clouds are still deep in the potential where tidal forces can be expected to be sufficiently strong to trigger cloud collapse. The fact that heating rates similar to the individual values can be recovered by only adjusting the exact trigger point without taking potential variations of initial cloud conditions or variations of the gravitational potential into account suggests that t_{start} is one of the major sources of scatter of a downstream SF sequence. The stacked and t_{start}-adjusted mean heating rates are lower than the per-segment heating rates, implying that another factor still erases part of the trend. This is the vertical (temperature) offset, which is due to slightly different initial conditions, as has been discussed in Section 5.3.3. This observation confirms the warning by Kruijssen (2017) that simple stacking of pericenter passages is not advisable because of scatter. However, problems can be diminished if it is possible to estimate the scatter in t_{start}. Additional scatter can result from the local environment (e.g., radiation field), which does not have to be identical for two clouds of the same evolutionary stage at different positions. For instance, pericenters on the near and far side are identified with each other in terms of evolutionary stage despite the spatial separation of ~ 120 pc. Hence, influences of the environment can be very different at a given time since the *last* pericenter passage.

5.4. Sequential Evolution in other CMZ Models

Although this analysis is based on the kinematic stream model of K15, similar results would be obtained assuming a different orbital model.[30] However, the interpretation of the

sequences we found in Section 5.3 relies on a varying tidal field strength along the orbit. In the context of a dense gas torus (Molinari et al. 2011) instead of streams, the basic requirement for a tidal triggering of cloud collapse is still present (as argued by Longmore et al. 2013b): gas passes close to the bottom of the GC gravitational potential. It is irrelevant if this is due to a displaced orbit (ring model), elliptical orbits (x_1/x_2 orbits in the bar model), or a radially oscillating stream. Differing dynamics (e.g., orbital speed) imply that the time axis of Figure 20 is stretched or squished, but the progression fundamentally stays the same. The major difference in the context of this work is the question whether another trigger point on the far side of the orbit is present, which does not strongly affect this analysis as most of the gas is detected in the dust ridge or near-side pericenter. Thus, a definite distinction between models is not possible, but the hints of a third trigger point at far-side pericenter passage favors the K15 model. As not all the models agree on the clouds' positions along the line of sight, any connection between the sequences we found relies on the adopted model. Some versions of the two spiral arms model place the 20 and 50 km s^{-1} clouds or Sgr C and the dust ridge on different arms (Sofue 1995; Sawada et al. 2004), thus no connection is given, whereas in a recent spiral arm model (Ridley et al. 2017) and the elliptical ring model, the dust ridge immediately follows the 20 and 50 km s^{-1} clouds. The K15 model is different from all other published orbital models of the CMZ in that it predicts two different pericenters on the near side. This is consistent with our observations, but the absence of dense gas on segment 2 before the dust ridge does not allow a definite distinction between models.

5.5. Relation to Other Recent GC SF Research

Finding a gas temperature sequence in the CMZ stream segments confirms implications that followed from the star formation triggering model by Longmore et al. (2013b), but does not directly confirm that the clouds themselves evolve as expected. Heating or cooling of molecular clouds does not necessarily have to be associated with star formation or collapse in the theoretically expected way, but can be related to other mechanisms such as cosmic ray heating as well (e.g., Yusef-Zadeh et al. 2007; Ao et al. 2013; Clark et al. 2013). A sequence of rising temperature could be observed as a function of distance to the potential heating sources Sgr A* and Sgr B2. For these two sources and the distribution of measurements, the

---

[30] Of course, this also assumes that a consensus about the 3D position of CMZ clouds is reached. Results differ greatly when a cloud is placed on the far side of the GC instead of in front.

Table 4
Conversion Equations for the Rotational to Kinetic Temperature Conversion as
Obtained by Ott et al. (2011) and Partially Published in
Ott et al. (2011) and Gorski et al. (2017)

	T_{kin}–T_{rot} conversion		Temperature Range		
$T_{kin,12}$	=	$6.05 \cdot \exp(0.06088\, T_{rot,12})$			
$T_{kin,24}$	=	$1.467\, T_{rot,24} - 6.984$	$0\,K \lesssim$	T_{kin}	$\lesssim 100\,K$
	=	$27.085 \cdot \exp(0.019\, T_{rot,24})$	$100\,K \lesssim$	T_{kin}	$\lesssim 500\,K$
$T_{kin,36}$	=	$T_{rot,36}$	$0\,K \lesssim$	T_{kin}	$\lesssim 50\,K$
	=	$28.87511 \cdot \exp(0.015\, T_{rot,36})$		T_{kin}	$> 50\,K$
$T_{kin,45}$	=	$1.143\, T_{rot,45} - 1.611$	$0\,K \lesssim$	T_{kin}	$\lesssim 50\,K$
	=	$21.024 \cdot \exp(0.0198\, T_{rot,45})$	$50\,K \lesssim$	T_{kin}	$\lesssim 500\,K$

Table 5
Fit Success Rates for the Six Ammonia Inversion Lines Observed with SWAG

	(1, 1)	(2, 2)	(3, 3)	(4, 4)	(5, 5)	(6, 6)
Selected pixels	24383	24383	24383	24383	24383	24383
Fitted pixels	23790	23025	23646	19269	19261	19245
Failed to fit	593	1358	917	5114	5122	5138
% fitted	97.6	94.4	96.2	79.0	79.0	78.9
Good fits	23437	22822	23403	19137	18795	18971
Bad fits	353	203	63	132	466	274
% good	98.5	99.1	99.7	99.3	97.6	98.6

Note. 24,383 pixels were selected by a two-step S/N criterion to be fitable in at least one of the lines NH$_3$ (1, 1) to NH$_3$ (6, 6). The actual number of attempted fits per ammonia species ("fitted pixels," second row) is lower because of non-identical distributions and decreasing S/N for higher states. The difference is given in rows 3 and 4 ("failed to fit" and success percentage) and lists the amount of pixels that could not be fitted because they were excluded by masking. Out of the attempted fits, the vast majority of >98.5% did converge and yielded physical plausible results ("good fits"); "bad" fits are defined by large uncertainty and physically implausible values (see Section 4.1 for details).

fitted time since pericenter passage can be related to physical distance. The observed temperature sequence in the dust ridge rises toward Sgr B2, which is qualitatively consistent with it being the locally dominating heating source. The other sequences, however, do not match this picture because the molecular clouds on the far side show an inverse trend and gas at negative longitudes requires a second heating source to the east that does not influence the close-by western end of the dust ridge. Similar arguments apply to Sgr A*. Clouds are observed to heat up beyond pericenter (closest distance to Sgr A*), and the 20 and 50 km s^{-1} clouds are colder than Sgr C, which is $\sim$1.5 times farther from Sgr A*. However, these arguments also rely on the 3D distribution of gas in the GC, which is still debated (e.g., McGary et al. 2001; Clavel et al. 2013; Kruijssen et al. 2015; Takekawa et al. 2015; Churazov et al. 2017).

It is therefore essential to gain more insight into cloud evolution in the stream and the GC in general in order to link it to observations of star formation tracers (in the dust ridge) and stars (Arches and Quintuplet clusters). Barnes et al. (2017) extend the SF sequence downstream from Sgr B2 by finding evidence of a gradual increase in stellar feedback activity as measured from the size of the hot gas bubbles driven by young massive stars. The Arches and Quintuplet clusters are found to be consistent in kinematics and age to have formed by tidally triggered cloud collapse and thus seem to fit in the GC star formation model (K15). If this can be confirmed by future observations, the time range covered by the model would greatly

increase from pre-collapse clouds ($t_{peri} \sim -1$ to -2 Myr) to evolved stars (Quintuplet, $t_{peri} \sim 5$ Myr) and span the whole time range of star formation. Immediate insights for cloud evolution could be gained from a study of internal cloud kinematic, size, shape, and density.

In addition to the ISM ingredients gas and dust, the key to a better understanding of (proto-) star formation in extreme environments such as the CMZ are the stars themselves. Evolution in gas and possibly also in dust is accompanied by increasing signs of star formation along the dust ridge that we suspect to partially power the rise in temperature. Starting from an increased base level after initial heating by tidal effects, the Brick is still cold and shows little star formation (Longmore et al. 2012; Kauffmann et al. 2013; Rodríguez & Zapata 2013), while cloud c contains H$_2$CO and SiO masers (Ginsburg et al. 2015), cloud d contains a H$_2$CO maser, which suggests massive star formation (Immer et al. 2012), and Sgr B2 is heavily forming stars, which heats the surrounding medium. From the qualitative picture, gas and stars seem to go hand in hand, providing a rough picture that needs to be tested in more detail in order to reach the goal of a well-calibrated absolute timeline of star formation in the CMZ.

6. Summary and Conclusions

We described the observations and data reduction of the SWAG survey and presented the first data products. This paper covers the central $\sim$250 pc of the CMZ in the Galactic Center in the six metastable ammonia inversion lines NH$_3$ (1, 1) to (6,6) at a resolution of $\sim$22″ ($\sim$0.9 pc). The gas distribution is asymmetric with respect to the Galactic Center (Sgr A*) as most gas is detected at positive longitudes. We find ammonia gas in the known arching structures, especially in the dust ridge spanning from the Brick (G0.253+0.016) to Sgr B2. The typical NH$_3$ (3, 3) main beam brightness is found to be on the order of a few hundred mJy beam^{-1} (a few K), but reaches up to 5.28 Jy beam^{-1} (24.8 K) in Sgr B2. Ammonia gas at $[0, b > 0]$ is oriented approximately perpendicular to the Galactic plane and shows significantly higher velocities than the rotating arc structures. The typical velocity dispersions are 5–25 km s^{-1}, but they are affected by blending of ammonia hyperfine components and multiple emission components along the line of sight.

Fitting the hyperfine structure allows us to derive maps of line width, opacity, column density, and kinetic gas temperature. We find the line widths to be Δv(FWHM) = 6–18 km s^{-1} with a typical value of $\sim$10 km s^{-1}, consistent for the six ammonia species. Large areas of the CMZ are optically thin, with the more massive clouds being somewhat optically thick at $\tau < 5$. Exceptions of high opacity ($\tau \gtrsim 10$) are the Brick, several clouds surrounding Sgr B2, an extension to the 20 km s^{-1} cloud, and G-0.40-0.20. Ammonia column densities reach up to $N \sim 7 \times 10^{16}$ cm^{-2} in Sgr B2 and several 10^{16} in the massive CMZ clouds. Smaller clouds on the gas "ring" show lower column densities of $N < 10^{16}$ cm^{-2}.

The kinetic gas temperatures exhibit two components, a cold component of 25–50 K traced by T_{12}, and a warm component of 50–120 K traced by T_{24}, T_{45}, and T_{36} where T_{ij} denotes the temperature derived from ammonia states NH$_3$ (i, i) and NH$_3$ (j, j). Sgr B2 stands out as the warm component and is detected at up to $\sim$200 K. On average over the CMZ, the cold component contributes $\sim$55% to the ammonia column density, the warm component $\sim$45%. In the 20 km s^{-1} and 50 km s^{-1} clouds, the cold gas fraction is higher ($\sim$68%) than in the dust
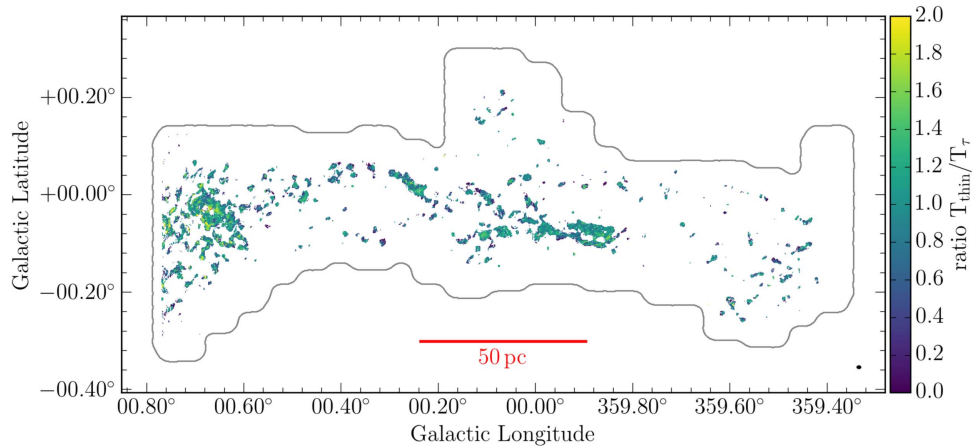
Figure 34. Ratio map $T_{\rm thin}/T_{\tau}$ of the ammonia T_{24} temperature assuming optically thin emission ($T_{\rm thin}$) and considering opacity effects (T_{τ}). The differences are minor (blue-green) in large areas of the map, but the temperature can be overestimated (yellow) in dense regions by factors of ~2.0. Temperatures in less dense clouds and at the edges of the fitted area are underestimated (dark blue).
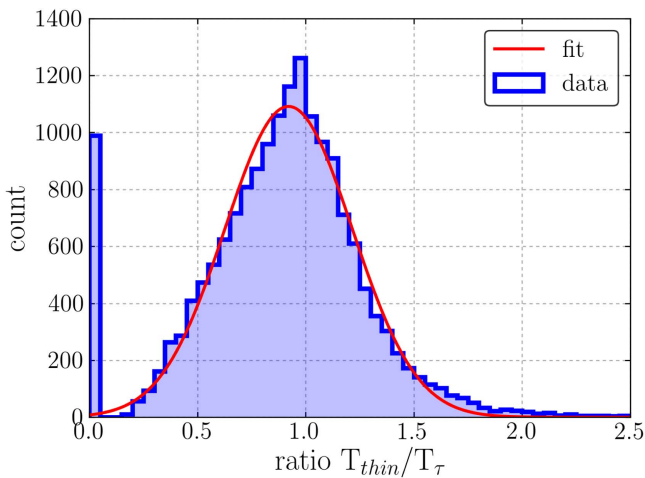

Figure 35. Histogram of the temperature ratio $T_{\rm thin}/T_{\tau}$ between the kinetic ammonia temperature T_{24} derived assuming optically thin emission and considering measured opacities (Figure 34). For ~1000 pixels at a ratio of 0.0, the hyperfine structure could be fitted and an opacity-corrected temperature derived, although the emission is faint enough to be masked while calculating the image moment 0 on which the temperature under thin assumption is based. The inverse case (ratios of $+\infty$) occurs more often, but does not show up in this plot. A Gaussian fit generally describes the distribution well, but does not fit a greater amount of temperature ratios of 1.0 and 1.5–2.0. The latter is the effect of considering the opacity for optically thick emission. As lower ammonia states are typically more occupied (falling slope in Boltzmann plot) and the opacity correction increases occupation over the thin approximation ($N_{\tau} > N_{\rm thin}$), the temperature decreases ($T_{\tau} < T_{\rm thin}$) and thus $T_{\rm thin}/T_{\tau} > 1.0$.

ridge (~60%). The warm gas component is more pronounced in Sgr B2, where both cold and warm gas contribute equally (~50% each) to the total column density. We confirm the kinetic gas temperature to be offset from the dust temperature, for which we derive offsets of ~10–15 K for the cold component and ~75–100 K for the warm component. Despite the offset, the median gas temperatures of both components are linearly correlated with the dust temperature.

One possibility to exploit this rich data set is given in Section 5 by statistically analyzing CMZ temperature, column density, and line width as a function of time based on the dynamical model of K15. We find evidence for a consistent, gradual heating of 52 K Myr^{-1} in two sequences in the dust ridge and at near-side pericenter passage in the three partially independent ammonia temperature tracers T_{24}, T_{45}, and T_{36}. Near

Sgr C, a steeper trend of ~100 K Myr^{-1} is detected, whereas at far-side pericenter passage, we identify a qualitative increase of gas temperature. A hint on time-dependent evolution is also found as a decreasing sequence of column density at near-side pericenter passage, while other time ranges show no or no consistent evolution. No evolution is found in line width, but instead, variations between clouds dominate potential weaker evolutionary trends. This time dependence can be explained in the context of Longmore et al. (2013b) and K15 as being the result of tidal triggering of cloud collapse when passing pericenter. Gravitational energy released through a turbulence cascade triggered by tidal compression is potentially the source of heating near pericenter. The observed sequences of rising temperatures can result if the heat cannot be efficiently radiated away in the dense molecular clouds. Clouds downstream the triggering point continue to collapse and begin to form stars in their cores, which introduces an increasing source of heat that likely powers the second sequence of rising gas temperatures. Stacking of the identified sequences results in a weaker correlation because of the scatter of the exact collapse triggering point, i.e., clouds do not collapse at identical orbital phase. By allowing the starting point of each sequence to vary by up to ± 0.3 Myr, we recover a heating rate of ~48 K Myr^{-1} and estimate the triggering point to scatter by -0.2 Myr to $+0.3$ Myr.

Our work demonstrates the power of ammonia temperature measurements in inferring physical conditions. Usually a tool for investigations on small scales, we greatly expanded the spatial scale as was never done before to derive temperatures, column density, and opacity in the inner CMZ, and finally, the whole CMZ in the full SWAG survey. Despite the large area, SWAG offers high resolution, which allows statistical conclusions like the observed rising temperature sequences. The other data of SWAG, spatial as well as spectral coverage, will be presented in forthcoming papers.
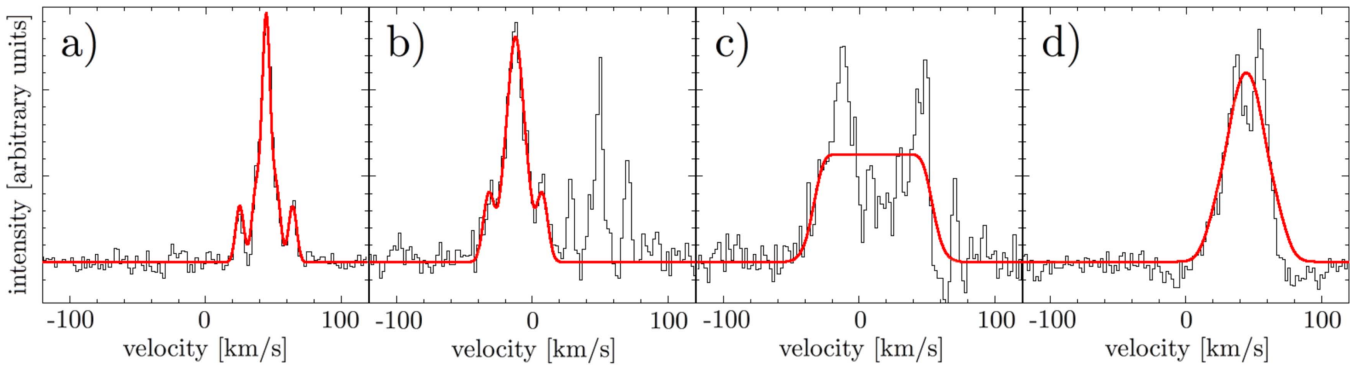
Figure 36. Examples of the ammonia hyperfine structure per pixel fits (red) to observed SWAG spectra (black). Satellite components blend with the main line because of the large line width (a), (b), and (c) or because of the blending of multiple lines along the line of sight (c) and (d). (a) Typical good fit of a single emission component along the line of sight. (b) For multiple components, the strongest component is usually fitted well. (c) Occasionally, two separated components of similar peak intensity may be fitted by an unphysically large line width. (d) When two (or more) components of similar intensity blend, they might be fitted as a single component with large line width. The latter two cases are excluded from further analyses by the large line width ((c), $\sim$80 km s^{-1}) and bad fit quality as given by the reduced χ^2 (d).

Appendix A
SWAG Data Products

A.1. Channel Maps

In Figures 22–26, we present the channel maps of NH$_3$ (1, 1), (2, 2), (4, 4), (5, 5), and (6, 6) as discussed in Section 3.1. The channel maps of NH$_3$ (3, 3) are shown in Figure 5.

A.2. Sample Spectra

In Figure 27, we present sample spectra toward the Brick for NH$_3$ (1, 1) to (6, 6).

A.3. Moment Maps

Figures 28–32 show the moment maps of NH$_3$ (1, 1), (2, 2), (4, 4), (5, 5), and (6, 6). Their generation from the respective data cubes is explained in Section 3.3.

Appendix B
Cleaning Depth in MOSMEM

Version 1.6 of mosmem as of 2015 contained[31] a bug that did not correctly scale the rms noise when emission is found, which resulted in accumulation of the background flux density level and a non-constant baseline in spectra (M. Wieringa, private

communication). The strength of this effect depends on the amount of cleaned flux density and thus on the number of iterations. Tests on line bearing and line-free channels of SWAG data showed that for up to $\sim$50 iterations, no measurable effects occur, while noticeable spectral slopes of tens of mJy beam^{-1} over the spectral range arise when $\gtrsim$100 iterations are used, and very high iteration counts of 250–500 result in multiple sudden unpredictable jumps of 30–80 mJy beam^{-1} in the spectra. These observations imply that the flux offsets are inherited from one channel to the next in the order of processing. Channels containing large amounts of emission (e.g., ammonia lines) would need about 150–200 iterations for mosmem to converge and thus still contain noticeable amounts of uncleaned sidelobe structure. The applied restriction to 50 iterations in the generation of SWAG maps therefore results in maps that are not affected by the software bug at the cost of remaining undeconvolved flux.

Appendix C
The Ammonia Thermometer

Ammonia is a good thermometer because of its inversion lines, which cover rotational temperatures from close to absolute zero to thousands of Kelvin when the rotational quantum number J increases. Its hyperfine structure allows directly calculating opacities, which are needed in order to derive correct temperatures without the need for a background source (on-off technique). The simplest approach in deriving column densities and subsequently temperatures is to assume optically thin emission, i.e., use moment-0 maps (Figure 7). As this technique cannot disentangle hyperfine satellite lines or multiple emission sources along the line of sight, it is problematic for ammonia and in the GC. Therefore, we fit the ammonia spectra to resolve hyperfine lines and complex emission. A comparison of these two methods for temperature deriving is given in Section C.4.1.

C.1. Rotational Temperature and Boltzmann Plot

The occupation of different rotational levels follows a Boltzmann distribution, and the ratio of two column densities therefore becomes a function of temperature (Goldsmith & Langer 1999). For a state of energy E with excitation temperature $T_{\rm ex}$ of the system, the probability of the system

---
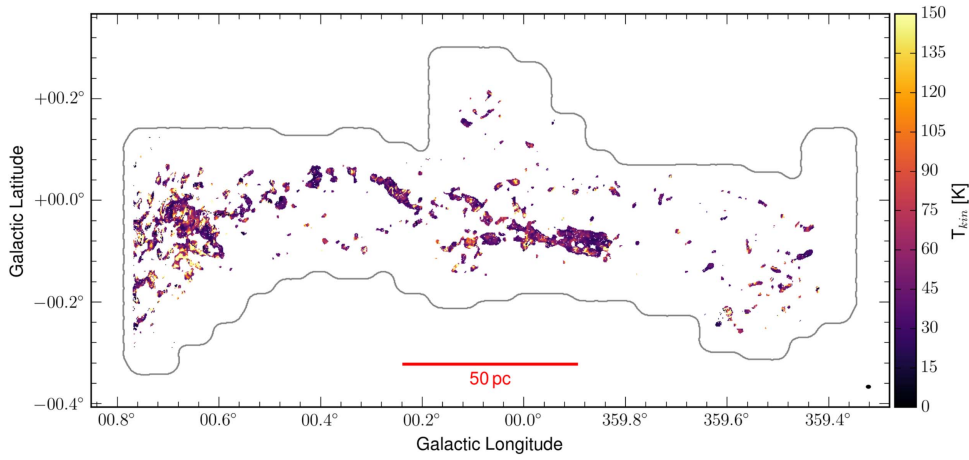
Figure 37. T_{12}
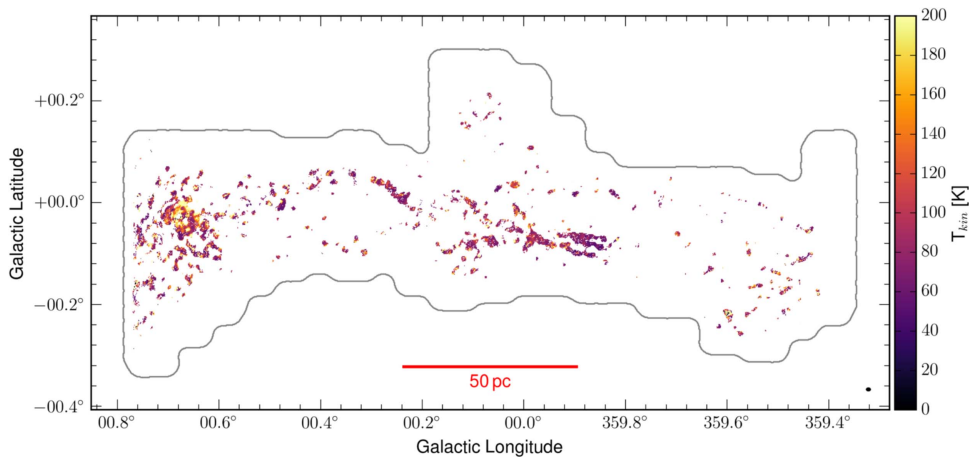
Figure 38. T_{45}

to be in that state is given by

$$p \propto \exp{\frac{E}{k_B T_{ex}}}, \qquad (2)$$

where $k_B = 1.38 \times 10^{-23}\ J/K$ is the Boltzmann constant. For two metastable inversion lines with rotational numbers $J = K$, the relative probability is called Boltzmann factor and depends only the energy difference ΔE. For rotational states, the temperature T_{ex} is accordingly called rotational temperature $T_{JJ'}$ for states J, J' after considering the correct conversion. The probability of being in a certain state can be translated into the number of particles in that state, which can be approximated by column densities because only the Boltzmann factor (relative ratio) is needed instead of absolute values. Therefore, the ratio of column density N_u in the upper rotational state u with J or J' can be expressed as

$$\frac{N_u'(J', J')}{N_u(J, J)} = \frac{g(J')}{g(J)} \frac{2J' + 1}{2J + 1} \exp\left(\frac{-\Delta E}{T_{JJ'}}\right), \qquad (3)$$

with relative weight factors of $2J + 1$ and statistical weights g that follow from quantum mechanical considerations as derived in Schilke (1989). It must be taken into account that ammonia can exist in two different configurations of the hydrogen atom nuclear spin, all spins parallel, or one spin antiparallel to the other two. The configurations differ in energy and thus give rise to two ladders of ammonia states, ortho for rotational states $J = 0, 3, 6, ...$ (all spins parallel, statistical weight $g = 2$) and para for $J = 1, 2, 4, 5,...$ (one spin antiparallel, $g = 1$). Equation (3) can be rewritten as

$$\underbrace{\ln\left(\frac{N_u'(J', J')}{g'(2J' + 1)}\right)}_{y'} - \underbrace{\ln\left(\frac{N_u(J, J)}{g(2J + 1)}\right)}_{y} = \underbrace{-\frac{\Delta E}{k_B T_{rot,JJ'}}}_{\Delta x / T_{rot,JJ'}}, \qquad (4)$$

which is an equation of simple linear form for the inverse temperature with slope m,

$$m = \frac{\Delta y}{\Delta x} = \frac{y' - y}{\Delta x}. \qquad (5)$$

The corresponding plot is called Boltzmann plot, with energy above ground state on the x-axis and y-axis values derived from measured column densities. For convenience, y is given in logarithms of base 10 instead of e as

$$y = \log_{10}\left(\frac{N(J, J)}{g(J)(2J + 1)}\right), \qquad (6)$$

35
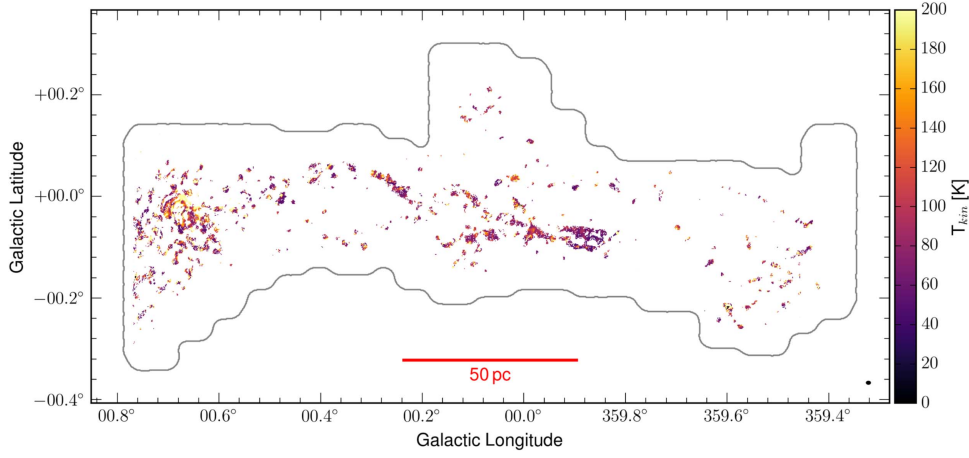
Figure 39. T_{36}

which leads to a correction factor of $\log_{10}(e)$ when calculating temperatures,

$$T_{\mathrm{rot,JJ'}} = \frac{-\log_{10}(e)}{m}. \qquad (7)$$

Overall, this means the rotational temperature of ammonia gas can be derived from the slope between two measurements of column density for the known state energies.

C.2. Excitation Temperature

For radio frequencies and the expected ISM temperatures (T [K] $\gtrsim 10$ K), the Rayleigh–Jeans approximation for blackbody emission holds because $\exp\left(-\frac{h\nu}{k_B T}\right) \approx 1 - \frac{h\nu}{k_B T}$. With intensities expressed as line temperatures and considering the limited beam size of a telescope, radiative transfer can be expressed as

$$T_L(\nu) = \eta_f T_{\mathrm{ex}}(1 - e^{-\tau}) + \eta_f T_{\mathrm{BG}}\, e^{-\tau} + (1 - \eta_f)T_{\mathrm{BG}} \qquad (8)$$

in the notation of Schilke (1989). T_L is the observed line temperature that results from source emission with excitation temperature T_{ex} and background T_{BG} that both pass through a medium with opacity τ. The beam filling factor η_f denotes the fractional area of the beam filled by the source on the sky. For completeness, it will be dragged along in further equations, but set to unity in all calculations as this is expected to be approximately given for the beam size of SWAG (~ 0.9 pc) and the extended emission detected ($>20''$).

Solving for T_{ex} results in

$$T_{\mathrm{rot,JJ'}} = T_{\mathrm{ex}} = \frac{T_L}{f(1 - e^{-\tau})} + T_{\mathrm{BG}}. \qquad (9)$$

The background temperature T_{BG} is set by the cosmic microwave background (CMB) at 2.7 K.

C.3. Column Density

In order to calculate rotational temperatures via Equation (7), the column densities of two states need to be known, which are given by

$$N(J, K) = \frac{3h}{8\pi^3} \frac{J(J + 1)}{K^2} \frac{1}{\mu^2} \frac{k_B}{h\nu_{JK}} \int T_{\mathrm{ex}}\, dv, \qquad (10)$$

with the Planck constant h, the Boltzmann constant k_B, the angular momentum J, the projected angular momentum K, the ammonia dipole moment μ, the frequency ν of the transition $J \to J'$, and the excitation temperature T_{ex} integrated over the velocity dv.

The integral is solved differently when assuming optically thin emission or considering opacities.

C.3.1. Column Density in the Optically Thin Limit

Assuming optically thin emission, column densities can simply be derived from observed intensities with the appropriate scaling factors because every detected photon directly corresponds to one emitting molecule. Following Ott et al. (2005, 2014), Mills & Morris (2013), whose work is based on Hüttemeister et al. (1993, 1995), and Mauersberger et al. (2003), the column density N in state (J, K) depends on the electric dipole moment μ in Debye and on the line brightness temperature T_{mb} as

$$N(J, K)[\mathrm{cm}^{-2}] = 1.6698 \cdot 10^{14} \cdot \frac{J(J + 1)}{K^2}$$

$$\times \frac{1}{\mu^2\,[D^2] \cdot \nu\,[\mathrm{GHz}]} \int_{\mathrm{line}} T_{\mathrm{mb}}\, dv\,[\mathrm{K\ km\ s^{-1}}] \qquad (11)$$

$$= \frac{7.77 \times 10^{13}}{\nu\,[\mathrm{GHz}]} \frac{J(J + 1)}{K^2} \int_{\mathrm{line}} T_{\mathrm{mb}}\, dv\,[\mathrm{K\ km\ s^{-1}}]. \qquad (12)$$

Equation (11) lists the general formula for any symmetric top molecule with dipole moment μ, whereas Equation (12) already includes $\mu = 1.472$ D for ammonia and shows the form given in the literature.

The datacube structure in discrete channels of width Δv_{chan} simplifies the integration in velocity over the spectral line to a summation of spectral channels, which in turn is just the definition of moment-0 flux $F_{\mathrm{mom0}} = \int T_{\mathrm{mb}}\, dv = \sum T_{\mathrm{mb}}\, \Delta v_{\mathrm{chan}}$,

$$N(J, K)[\mathrm{cm}^{-2}] = 1.6698 \cdot 10^{14} \frac{J(J + 1)}{K^2}$$

$$\cdot \frac{1}{\mu^2\,[D^2] \cdot \nu\,[\mathrm{GHz}]} \cdot \sum_{\mathrm{line}} T_i\, \Delta v_{\mathrm{chan}}\,[\mathrm{K\ km\ s^{-1}}], \qquad (13)$$
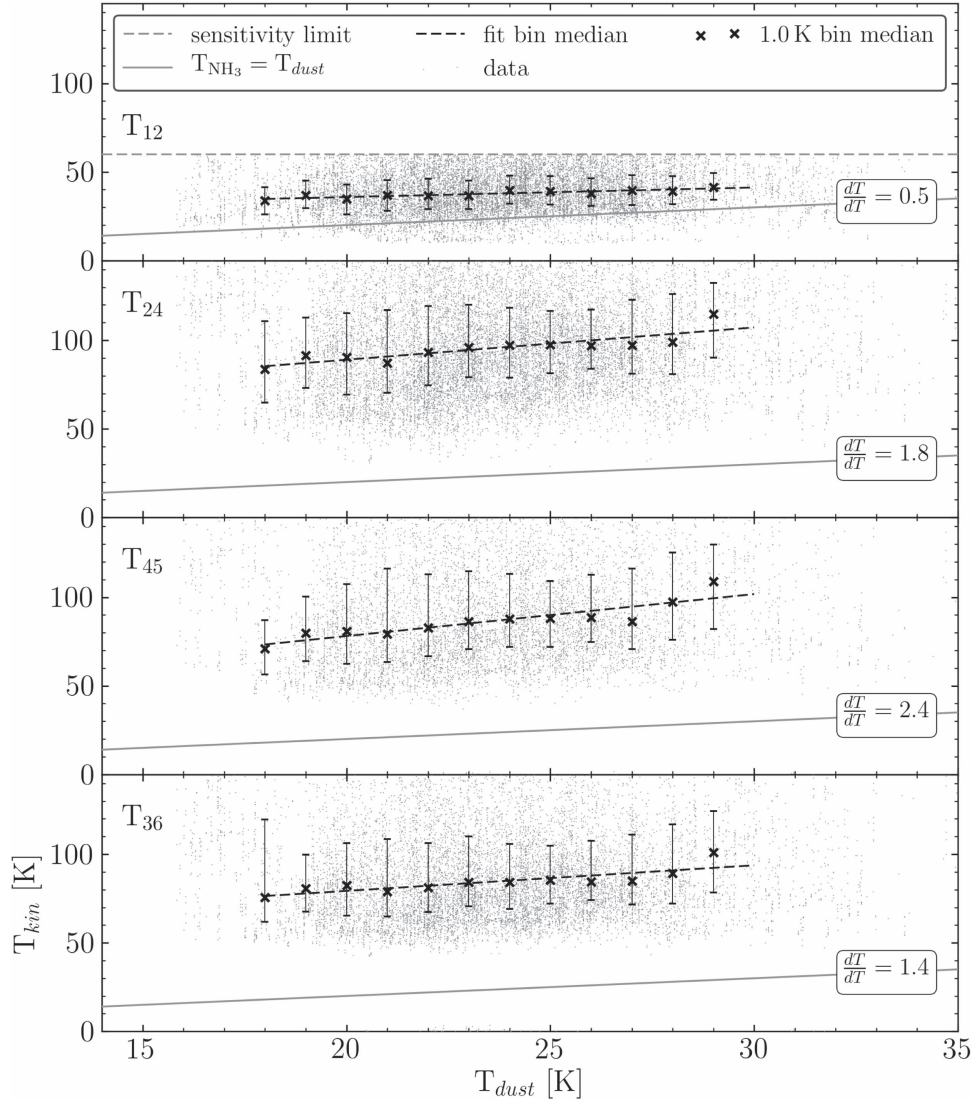
Figure 40. Correlation of the Hi-Gal dust temperature (Molinari et al. 2011) and the kinetic ammonia gas temperature as in Figure 17. The temperature estimate is labeled in the top left corner of each panel. Panels are zoomed to display the same range to allow a direct comparison.

$$= \frac{7.77 \times 10^{13}}{\nu \text{ [GHz]}} \frac{J(J+1)}{K^2} F_{\text{mom0}} \text{ [K km s}^{-1}\text{]}, \quad (14)$$

C.3.2. Column Densities Considering Opacity

By solving the radiative transfer equation, it is possible to derive an expression for the column density without assuming high or low optical depth because an exact solution for the relation of T_{ex} ($T_{JJ'}$ for rotational states) and observed brightness temperature T_{mb} is known (Schilke 1989).

The derivation starts again from the general approach in Equation (10), but then solves the integral over a spectral line of Gaussian shape (peak T_L and FWHM Δv_{int}) with excitation temperature as in Equation (9). The integral over a single hyperfine component thus is given by

$$A = \frac{\sqrt{\pi}}{2\sqrt{\ln 2}} \cdot T_L \cdot \Delta v_{\text{int}} \quad (15)$$

and the velocity integrated temperature becomes

$$\int T_{\text{ex}} \, dv = \frac{\sqrt{\pi}}{2\sqrt{\ln 2}} \Delta v_{\text{int}} \frac{T_{\text{ex}} \tau}{f_J}, \quad (16)$$

$$= \frac{\sqrt{\pi}}{2\sqrt{\ln 2}} \Delta v_{\text{int}} \frac{T_L \tau}{f f_J (1 - e^{-\tau})}, \quad (17)$$

T_L denotes the line peak intensity and must not be confused with the integrated line intensity T_{mb} we used before. Δv_{int} stands for the fitted FWHM of a single hyperfine component.

Calculating all numerical factors and logically rearranging the parts to match Equation (11)–(14) results in

$$N(J, K) = 1.77745 \cdot 10^{14} \text{ cm}^{-2} \cdot \frac{J(J+1)}{K^2}$$
$$\times \frac{\Delta v_{\text{int}} \text{ [km s}^{-1}\text{]}}{(\mu \text{ [D]})^2 \, \nu \text{ [GHz]}} \frac{\tau \, T_L \text{ [K]}}{f_J (1 - e^{-\tau})}. \quad (18)$$

The pre-factor of $1.77745 \cdot 10^{14}$ applies when the beam filling factor is set to unity, line width Δv_{int} is given in km s^{-1},
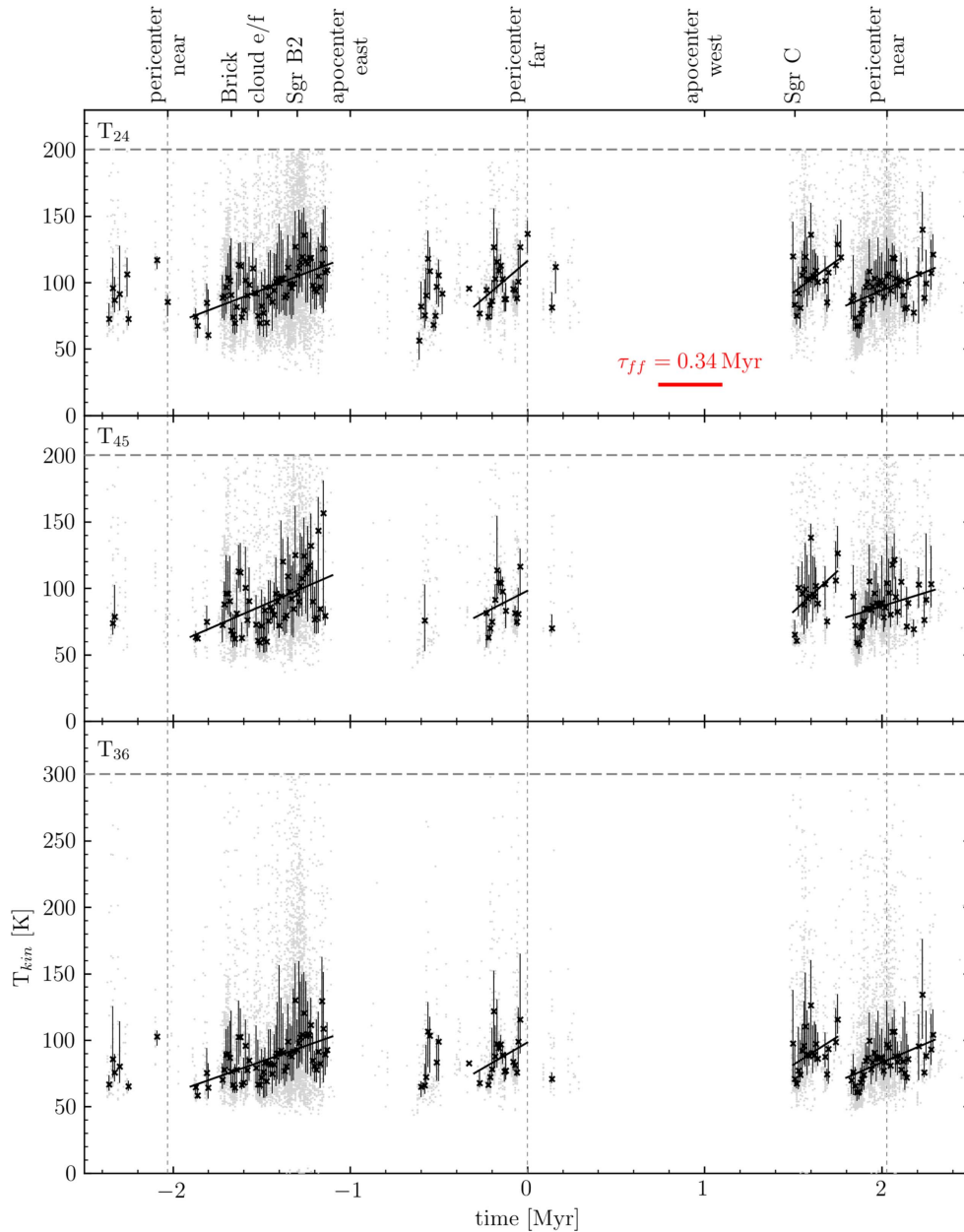
Figure 41. Kinetic ammonia temperature as a function of time since far-side pericenter passage (bottom *x*-axis; the top *x*-axis shows important dynamical points in the K15 model and massive molecular clouds). The temperature tracer is given in the top left corner of each panel. A horizontal dashed gray line denotes the sensitivity limit of the conversion from rotational into kinetic temperature. Vertical dashed lines highlight the occurrence of pericenter passages. Measurements for individual pixels (light gray points) are overlaid with black crosses denoting medians in bins of 0.01 Myr and error intervals that include 50% of the data in each bin.

dipole moment μ in Debye, frequency of the inversion line in GHz and line peak intensity in Kelvin. f_J is a factor to correct the fitted opacity τ for its line profile and is basically the ratio of flux in the central hyperfine component (see Schilke 1989, for details). Table 3 lists f_J for NH$_3$ (1, 1) to (6, 6) for five hyperfine components per line, whereof the central ("component 0") enters Equation (18).

Figure 33 shows the column density distribution of the upper state N_u of NH$_3$ (3, 3) as an example.

C.3.3. Total Ammonia Column Density

Note that Equations (18) and (12) and Figure 33 give the column density of ammonia in the lower transition state only. The total column density of the state (J, K) must also take the

molecules in the upper transition state into account. In thermal equilibrium, the column densities of both states are related by a Boltzmann factor

$$N(J, K) = N_l(J, K)\left(1 + \exp\left(-\frac{h\nu}{k_B T}\right)\right) \qquad (19)$$

$$\simeq 2 \times N_l(J, K) \qquad \text{for } T \gg \frac{h\nu}{k_B}. \qquad (20)$$

In the ground state $(J = 0)$, the inversion states are degenerate and no transition can be observed, which means that the column density N_{00} cannot be derived directly but needs to be extrapolated from low metastable states. As the slope in a typical Boltzmann plot (excitation state-scaled
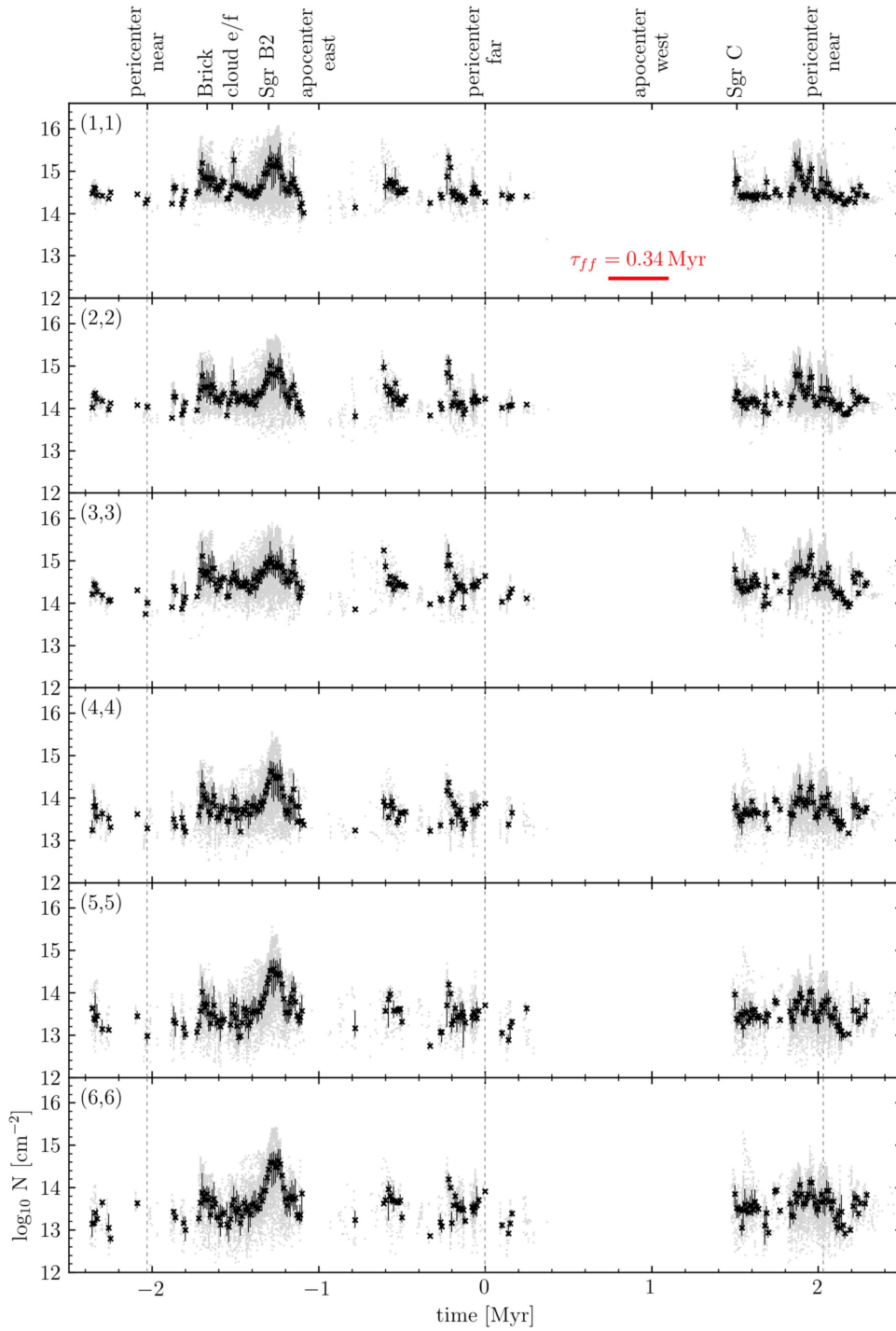
Figure 42. Ammonia column density as a function of time since far-side pericenter passage (bottom *x*-axis; the top *x*-axis shows important dynamical points in the K15 model and massive molecular clouds). The ammonia species is given in the top left corner of each panel. Vertical dashed lines highlight the occurrence of pericenter passages. Measurements for individual pixels (light gray points) are overlaid with black crosses denoting medians in bins of 0.01 Myr and error intervals that include 50% of the data in each bin.

column density versus excitation temperature) of ammonia emission of the GC starts to flatten around $J = 4$–6, the best estimate for N_{00} is derived from the slope between measurements at $J = 1$ and $J = 2$, i.e., rotational temperature T_{12}. If the ortho/para ammonia abundance ratio is not known, the simplest approach is to assume occupation by thermal equilibrium of states $J = 0, 1, 2$ at temperature T_{12}, hence to extrapolate N_{00} according to Equation (21) (Ungerechts

et al. 1986). The factor 23.2 K is given by the energy difference of NH$_3$ (0, 0) and NH$_3$ (1, 1),

$$N_{00} = \frac{1}{3} \exp\left(\frac{23.2\,\mathrm{K}}{T_{\mathrm{kin},12}}\right) N_{11}. \tag{21}$$

The "total" column density of ammonia is then derived by summing the six directly measured column densities
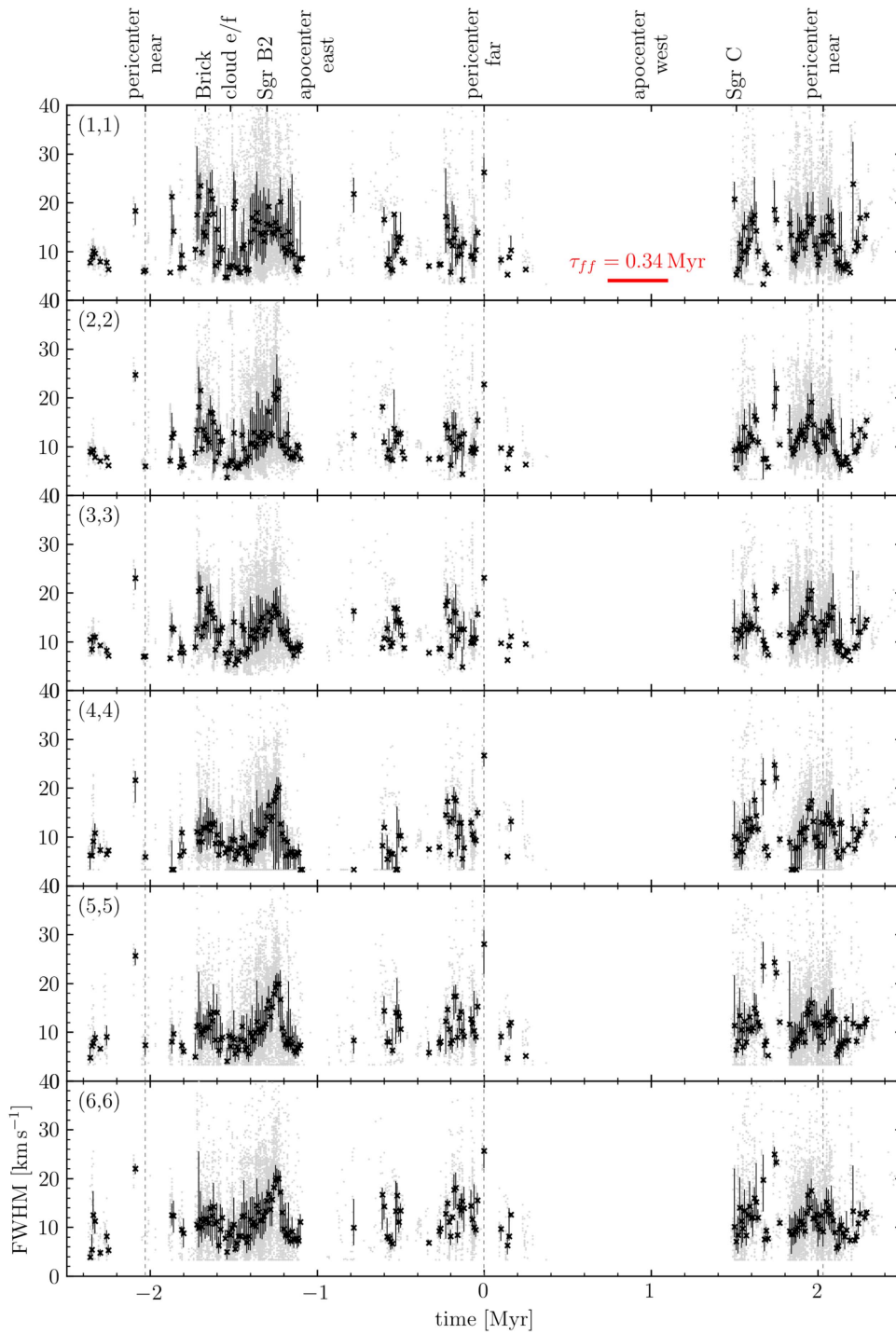
Figure 43. Ammonia line width as a function of time since far-side pericenter passage (bottom *x*-axis; the top *x*-axis shows important dynamical points in the K15 model and massive molecular clouds). The ammonia species is given in the top left corner of each panel. Vertical dashed lines highlight the occurrence of pericenter passages. Measurements for individual pixels (light gray points) are overlaid with black crosses denoting medians in bins of 0.01 Myr and error intervals that include 50% of the data in each bin.

$(N = N_l + N_u)$ for states $J = 1, ..., 6$ and the extrapolated $J = 0$ column density. In thermal equilibrium, higher states are increasingly less populated and can thus be approximated to contribute negligibly to the total column density for low temperatures. Equation (22) uses these assumptions, i.e., does not contain the contribution of ammonia in rotation states higher than $J = 6$ and consequently must be understood as a lower limit. How close this limit is to the real ammonia column density can roughly be estimated by the ratio N_{00}/N_{66}, which in SWAG typically exceeds 10 with only few very hot clouds such as Sgr B2 that contain relevant amounts of ammonia in higher excitation states, as was also found by Mills & Morris (2013). The assumption of thermal equilibrium, which is required to extrapolate the total column density, does not hold in all CMZ clouds, whereas the lower limit is supported by direct measurements and thus is more robust.

The total column density of ammonia (defined to include emission up to $J = 6$) is thus given by

$$N_{\rm tot} = \left[\frac{1}{3}\exp\left(\frac{23.2\ {\rm K}}{T_{12,\rm kin}}\right) + 1\right]N_{11}$$
$$+ N_{22} + N_{33} + N_{44} + N_{55} + N_{66}. \qquad (22)$$

C.4. Rotational to Kinetic Temperature Conversion

The rotational temperature is always lower than the kinetic temperature, with negligible difference at low values. For increasing temperature, the deviation also increases and must be taken into account. Reasons for this behavior are the increasing number of energetically available non-metastable levels for depopulation of higher metastable states and radiative decay (Walmsley & Ungerechts 1983). LVG radiative transfer models allow deriving approximations to the conversion of rotational to kinetic temperature. Ott et al. (2011) calculated LVG grids for temperatures up to 500 K for metastable ammonia species up to (6, 6) and derived exponential functions for the rotational-to-kinetic temperature conversion. These fits agree with the modeled curves within less than 5% for the temperature measures calculated in this work, which are T_{12}, T_{24}, T_{45}, and T_{36}, denoting the kinetic temperature T_{ij} derived from NH_3 (i, i) and NH_3 (j, j). Table 4 lists the conversion functions as partially published in Ott et al. (2011) and Gorski et al. (2017). Toward high kinetic temperatures, the conversion flattens out, which decreases the ability to correctly discern temperatures. Especially the temperature measurements of low ammonia states are affected, effectively setting an upper limit above which the tracer becomes unreliable as even small changes in $T_{\rm rot}$ by random errors translate into substantial changes in $T_{\rm kin}$. A cutoff is thus applied to all rotational temperatures before conversion to exclude high values that cannot be reliably translated into kinetic temperatures.

With the $T_{\rm kin}-T_{\rm rot}$ conversion in hand, all further mentions of temperature are kinetic temperatures labeled T_{ij} if not explicitly stated otherwise, e.g., by the subscript $T_{{\rm rot},ij}$.

C.4.1. Optical Depth Effects on Temperature

As described in Appendix C, temperatures can also be calculated assuming optically thin emission, as is often done (in extra-galactic contexts), with the advantage of being able to derive temperatures over a larger area. From the fitted opacities (Figure 14), it is already known that this assumption is not satisfied in a significant portion of the map. The practical differences for derived temperatures are shown in Figure 34, which plots the ratio $T_{\rm thin}/T_\tau$ of the kinetic temperature T_{24} derived under the assumption of optically thin emission and considering fitted opacities. The differences are minor in large areas of the map, but the temperature can be overestimated by $T_{\rm thin}$ in dense regions by factors of up to 1.6 in Sgr B2. Temperatures in less dense clouds and at the edges of the fitted area are typically underestimated by factors of $\lesssim 2$. This can also be seen in a histogram of the map (Figure 35) as an increase in ratios >1.0 over what is expected from statistical, normally distributed errors (Gaussian fit). In an optically thick molecular cloud, not all emission can be detected because of self-absorption and scattering, as would be the case in an optically thin cloud. The derived column densities thus increase when opacity is considered. The temperature is derived from the inverse slope of the column density as a function of

molecular energy level, which results in lower temperatures for two conditions: when the opacity is considered in calculating the column density, and when the opacity decreases for higher states, which typically is the case. Given that the opacity typically decreases for higher states, the effect on column density is stronger for lower J transitions. As the temperature is derived from the inverse slope of the column density as a function of molecular energy level, considering the opacity results in lower temperatures.

Appendix D
Details on Hyperfine Structure Fitting in CLASS

Figure 36 shows the typical fit quality and two examples of failed fits which are excluded from the further analysis. Table 5 lists the statistics of a pixel-by-pixel fitting.

Appendix E
Further Temperature Maps

Maps of the kinetic temperature tracers T12, T45, and T36 are shown in Figures 37–39, respectively.

Appendix F
Further Temperature Comparisons

Figure 40 shows the correlation between the four tracers of ammonia gas temperature and dust temperature.

Appendix G
Further Sequence Plots

Figures 41–43 show the orbital evolution of ammonia gas temperature, column density and line width for the four temperature tracers and six ammonia lines.

ORCID iDs

Nico Krieger ⓘ https://orcid.org/0000-0003-1104-2014
Jürgen Ott ⓘ https://orcid.org/0000-0001-8224-1956
Henrik Beuther ⓘ https://orcid.org/0000-0002-1700-090X
Fabian Walter ⓘ https://orcid.org/0000-0003-4793-7880
David S. Meier ⓘ https://orcid.org/0000-0001-9436-9471
Elisabeth A. C. Mills ⓘ https://orcid.org/0000-0001-8782-1992
Yanett Contreras ⓘ https://orcid.org/0000-0002-6388-3635
Adam Ginsburg ⓘ https://orcid.org/0000-0001-6431-9633
Christian Henkel ⓘ https://orcid.org/0000-0002-7495-4005
James Jackson ⓘ https://orcid.org/0000-0002-3466-6164
Steven Longmore ⓘ https://orcid.org/0000-0001-6353-0170
Mark R. Morris ⓘ https://orcid.org/0000-0002-6753-2066
Erik Rosolowsky ⓘ https://orcid.org/0000-0002-5204-2259
Hiroko Shinnaga ⓘ https://orcid.org/0000-0001-9407-6775
Qizhou Zhang ⓘ https://orcid.org/0000-0003-2384-6589

References

Ao, Y., Henkel, C., Menten, K. M., et al. 2013, A&A, 550, A135
Bally, J., Aguirre, J., Battersby, C., et al. 2010, ApJ, 721, 137
Barnes, A. T., Longmore, S. N., Battersby, C., et al. 2017, MNRAS, 469, 2263
Betz, A. L., McLaren, R. A., & Spears, D. L. 1979, ApJL, 229, L97
Bigiel, F., Leroy, A., Walter, F., et al. 2010, AJ, 140, 1194
Boehle, A., Ghez, A. M., Schödel, R., et al. 2016, ApJ, 830, 17
Churazov, E., Khabibullin, I., Ponti, G., & Sunyaev, R. 2017, MNRAS, 468, 165
Clark, P. C., Glover, S. C. O., Ragan, S. E., Shetty, R., & Klessen, R. S. 2013, ApJL, 768, L34

Clavel, M., Terrier, R., Goldwurm, A., et al. 2013, A&A, 558, A32
Federrath, C., Rathborne, J. M., Longmore, S. N., et al. 2016, ApJ, 832, 143
Ferrière, K., Gillard, W., & Jean, P. 2007, A&A, 467, 611
Ginsburg, A., Henkel, C., Ao, Y., et al. 2016, A&A, 586, A50
Ginsburg, A., Walsh, A., Henkel, C., et al. 2015, A&A, 584, L7
Goldsmith, P. F., & Langer, W. D. 1999, ApJ, 517, 209
Gorski, M., Ott, J., Rand, R., et al. 2017, ApJ, 842, 124
Güsten, R., Walmsley, C. M., & Pauls, T. 1981, A&A, 103, 197
Henkel, C., Braatz, J. A., Menten, K. M., & Ott, J. 2008, A&A, 485, 451
Henshaw, J. D., Longmore, S. N., & Kruijssen, J. M. D. 2016a, MNRAS, 463, L122
Henshaw, J. D., Longmore, S. N., Kruijssen, J. M. D., et al. 2016b, MNRAS, 457, 2675
Ho, P. T. P., Barrett, A. H., & Martin, R. N. 1978, ApJL, 221, L117
Ho, P. T. P., & Townes, C. H. 1983, ARA&A, 21, 239
Hüttemeister, S., Wilson, T. L., Bania, T. M., & Martin-Pintado, J. 1993, A&A, 280, 255
Hüttemeister, S., Wilson, T. L., Mauersberger, R., et al. 1995, A&A, 294, 667
Immer, K., Kauffmann, J., Pillai, T., Ginsburg, A., & Menten, K. M. 2016, A&A, 595, A94
Immer, K., Menten, K. M., Schuller, F., & Lis, D. C. 2012, A&A, 548, A120
Johnston, K. G., Beuther, H., Linz, H., et al. 2014, A&A, 568, A56
Juvela, M., Padoan, P., & Nordlund, Å. 2001, ApJ, 563, 853
Kauffmann, J., Pillai, T., & Zhang, Q. 2013, ApJL, 765, L35
Kauffmann, J., Pillai, T., Zhang, Q., et al. 2017a, A&A, 603, A89
Kauffmann, J., Pillai, T., Zhang, Q., et al. 2017b, A&A, 603, A90
Kendrew, S., Ginsburg, A., Johnston, K., et al. 2013, ApJL, 775, L50
Kennicutt, R. C., Jr. 1998, ApJ, 498, 541
Kruijssen, J. M. D., Dale, J. E., & Longmore, S. N. 2015, MNRAS, 447, 1059
Kruijssen, J. M. D., & Longmore, S. N. 2013, MNRAS, 435, 2598
Kruijssen, J. M. D., Longmore, S. N., Elmegreen, B. G., et al. 2014, MNRAS, 440, 3370
Kruijssen, J. M. D. 2017, in IAU Symp. 322, The Multi-Messenger Astrophysics of the Galactic Centre, ed. R. M. Crocker, S. N. Longmore, & G. V. Bicknell (Cambridge: Cambridge Univ. Press), 64
Krumholz, M. R., Dekel, A., & McKee, C. F. 2012, ApJ, 745, 69
Krumholz, M. R., & Kruijssen, J. M. D. 2015, MNRAS, 453, 739
Krumholz, M. R., Kruijssen, J. M. D., & Crocker, R. M. 2017, MNRAS, 466, 1213
Krumholz, M. R., & McKee, C. F. 2005, ApJ, 630, 250
Lada, C. J., Forbrich, J., Lombardi, M., & Alves, J. F. 2012, ApJ, 745, 190
Lada, C. J., Lombardi, M., & Alves, J. F. 2010, ApJ, 724, 687
Larson, R. B. 1981, MNRAS, 194, 809
Launhardt, R., Zylka, R., & Mezger, P. G. 2002, A&A, 384, 112
Lebrón, M., Mangum, J. G., Mauersberger, R., et al. 2011, A&A, 534, A56
Leroy, A. K., Bolatto, A. D., Ostriker, E. C., et al. 2015, ApJ, 801, 25
Leroy, A. K., Walter, F., Brinks, E., et al. 2008, AJ, 136, 2782
Lis, D. C., & Carlstrom, J. E. 1994, ApJ, 424, 189
Lis, D. C., Li, Y., Dowell, C. D., & Menten, K. M. 1999, in ESA Special Publication 427, The Universe as Seen by ISO, ed. P. Cox & M. F. Kessler (Paris: ESA), 627
Lis, D. C., Menten, K. M., Serabyn, E., & Zylka, R. 1994, ApJL, 423, L39
Longmore, S. N., Bally, J., Testi, L., et al. 2013a, MNRAS, 429, 987
Longmore, S. N., Kruijssen, J. M. D., Bally, J., et al. 2013b, MNRAS, 433, L15
Longmore, S. N., Rathborne, J., Bastian, N., et al. 2012, ApJ, 746, 117
Lu, X., Zhang, Q., Kauffmann, J., et al. 2017, in IAU Symp. 322, The Multi-Messenger Astrophysics of the Galactic Centre, ed. R. M. Crocker, S. N. Longmore, & G. V. Bicknell (Cambridge: Cambridge Univ. Press), 99
Mangum, J. G., Darling, J., Henkel, C., et al. 2013, ApJ, 779, 33
Mauersberger, R., Henkel, C., Weiß, A., Peck, A. B., & Hagiwara, Y. 2003, A&A, 403, 561
Mauersberger, R., Henkel, C., Wilson, T. L., & Walmsley, C. M. 1986, A&A, 162, 199
McGary, R. S., Coil, A. L., & Ho, P. T. P. 2001, ApJ, 559, 326
McMullin, J. P., Waters, B., Schiebel, D., Young, W., & Golap, K. 2007, in ASP Conf. Ser. 376, Astronomical Data Analysis Software and Systems XVI, ed. R. A. Shaw, F. Hill, & D. J. Bell (San Francisco, CA: ASP), 127
Mills, E. A. C., & Morris, M. R. 2013, ApJ, 772, 105
Molinari, S., Bally, J., Noriega-Crespo, A., et al. 2011, ApJL, 735, L33
Morris, M., & Serabyn, E. 1996, ARA&A, 34, 645
Morris, M., Zuckerman, B., Palmer, P., & Turner, B. E. 1973, ApJ, 186, 501
Oka, T., Hasegawa, T., Sato, F., Tsuboi, M., & Miyazaki, A. 1998, ApJS, 118, 455
Oka, T., Mizuno, R., Miura, K., & Takekawa, S. 2016, ApJL, 816, L7
Ott, J., Henkel, C., Braatz, J. A., & Weiß, A. 2011, ApJ, 742, 95
Ott, J., Weiss, A., Henkel, C., & Walter, F. 2005, ApJ, 629, 767
Ott, J., Weiß, A., Staveley-Smith, L., Henkel, C., & Meier, D. S. 2014, ApJ, 785, 55
Ott, J., Weiß, A., Staveley-Smith, L., Henkel, C., & Meier, D. S. 2014, ApJ, 785, 55
Pillai, T., Kauffmann, J., Tan, J. C., et al. 2015, ApJ, 799, 74
Rathborne, J. M., Longmore, S. N., Jackson, J. M., et al. 2014a, ApJ, 786, 140
Rathborne, J. M., Longmore, S. N., Jackson, J. M., et al. 2014b, ApJL, 795, L25
Rathborne, J. M., Whitaker, J. S., Jackson, J. M., et al. 2016, PASA, 33, e030
Reid, M. J., Menten, K. M., Brunthaler, A., et al. 2014, ApJ, 783, 130
Ridley, M. G. L., Sormani, M. C., Treß, R. G., Magorrian, J., & Klessen, R. S. 2017, MNRAS, 469, 2251
Robitaille, T., & Bressert, E. 2012, APLpy: Astronomical Plotting Library in Python, Astrophysics Source Code Library, ascl:1208.017
Rodríguez, L. F., & Zapata, L. A. 2013, ApJL, 767, L13
Rodríguez-Fernández, N. J. 2011, MSAIS, 18, 195
Rodríguez-Fernández, N. J., & Combes, F. 2008, A&A, 489, 115
Sault, R. J., Staveley-Smith, L., & Brouw, W. N. 1996, A&AS, 120, 375
Sault, R. J., Teuben, P. J., & Wright, M. C. H. 1995, in ASP Conf. Ser. 77, Astronomical Data Analysis Software and Systems IV, ed. R. A. Shaw, H. E. Payne, & J. J. E. Hayes (San Francisco, CA: ASP), 433
Sawada, T., Hasegawa, T., Handa, T., & Cohen, R. J. 2004, MNRAS, 349, 1167
Schilke, P. 1989, dissertation, Universität Bonn
Schuller, F., Menten, K. M., Contreras, Y., et al. 2009, A&A, 504, 415
Shetty, R., Beaumont, C. N., Burton, M. G., Kelly, B. C., & Klessen, R. S. 2012, MNRAS, 425, 720
Shirley, Y. L. 2015, PASP, 127, 299
Sofue, Y. 1995, PASJ, 47, 527
Stolte, A., Hußmann, B., Morris, M. R., et al. 2014, ApJ, 789, 115
Takekawa, S., Oka, T., & Tanaka, K. 2015, in ASP Conf. Ser. 499, Revolution in Astronomy with ALMA: The Third Year, ed. D. Iono et al. (San Francisco, CA: ASP), 171
Townes, C. H., & Schawlow, A. L. 1975, Microwave Spectroscopy (New York: Dover)
Ungerechts, H., Walmsley, C., & Winnewisser, G. 1986, A&A, 157, 207
Walker, D. L., Longmore, S. N., Bastian, N., et al. 2015, MNRAS, 449, 715
Walmsley, C., & Ungerechts, H. 1983, A&A, 122, 164
Wilson, W. E., Ferris, R. H., Axtens, P., et al. 2011, MNRAS, 416, 832
Yusef-Zadeh, F., Wardle, M., & Roy, S. 2007, ApJL, 665, L123
Zschaechner, L. K., Ott, J., Walter, F., et al. 2016, ApJ, 833, 41